DESIGN AND DEVELOPMENT OF A TRAVELING WAVE FERRO-MICROFLUIDIC DEVICE AND MULTI-PHYSICS MODEL FOR POTENTIAL CELL SEPARATION AND SORTING IN WATER BASED FERROFLUIDS

by

Maegan Edwards

A thesis submitted to the faculty of
The University of North Carolina at Charlotte
in partial fulfillment of the requirements
for the degree of Master of Science in
Applied Energy and Electromechanical Engineering

Charlotte

2023

Approved by:

_____
Dr. Rodward L. Hewlin, Jr.

_____
Dr. Wesley Williams

_____
Dr. Michael Smith

ABSTRACT

MAEGAN EDWARDS. Design and Development of a Traveling Wave Ferro-Microfluidic Device and Multi-Physics Model for Potential Cell Separation and Sorting in Water Based Ferrofluids (Under the direction of DR. RODWARD L. HEWLIN, JR.)

This thesis presents the design and development of a simple traveling wave ferro-microfluidic device and system rig purposed for the potential manipulation and magnetophoretic separation of cells in water-based ferrofluids. This thesis details in full: (1) a computational multi-physics model developed for predicting the dynamics of magnetic and nonmagnetic microparticles in the ferro-microfluidic device, (2) a method for tailoring cobalt ferrite nanoparticles for specific diameter size ranges *(10-20nm)*, (3) the development of a ferro-microfluidic device for potentially separating cells and magnetic nanoparticles, (4) the development of a water-based ferrofluid with magnetic nanoparticles and non-magnetic microparticles and (5) the design and development of a system rig for producing the electric field within the ferro-microfluidic channel device for magnetizing and manipulating nonmagnetic particles in ferro-microfluidic channel.

The results reported in this thesis demonstrate proof of concept for magnetophoretic manipulation and separation of magnetic and non-magnetic particles in a simple ferro-microfluidic device. The design reported in this model is an improvement over existing magnetic excitation microfluidic system designs in that heat is efficiently removed from the circuit board to allow a range of input currents and frequencies to manipulate non-magnetic particles. Although this work did not analyze the separation of cells from magnetic particles, the results demonstrate that non-magnetic *(surrogates for cellular materials)* and magnetic entities can be separated and, in some cases, continuously pushed through the channel based on amperage, size, frequency and electrode spacing. The results

reported in this work establish that the developed ferro-microfluidic device may potentially be used as an effective platform for microparticle and cellular manipulation and sorting.

This research consisted of a multi-physics computational model development and analyses as well as MEMS fabrication techniques, to develop an integrated microfluidic device that employs ferrofluids *(an aqueous suspension of magnetic nanoparticles for manipulation and separation of target particles)*. Conceptually, the magnetic nanoparticles in the ferrofluid direct the nonmagnetic moieties to collection sites once subjected to traveling magnetic fields. We present a detailed treatment of the physical mechanism underlying the manipulation of nonmagnetic particles using ferrofluids, including a thorough theoretical analysis of the dynamic behavior of particles within ferro-microfluidic devices.

ACKNOWLEDGEMENTS

I would like to acknowledge the engineering team of Sigenics Inc. for their help in developing the programmable electronic chip platforms, Mr. Jay Dalton of the Shared Materials Instrumentation Facility at Duke University for his help in developing the single channel mask for the microfluidic channel mold development, Dr. Deguzman of the University of North Carolina at Charlotte Physics and Optical Sciences Department for his help in the UNC-C cleanroom with fabricating the PDMS microfluidic channels and fabricating the cobalt ferrite particles, and Christopher Schultz, an undergraduate student of the UNC-C Electrical Engineering Technology program for his help in instrumenting the magnetic rig. I would also like to thank the graduate thesis committee Dr. Wesley Williams and Dr. Michael Smith for their help with this research.

This work was funded by the University of North Carolina at Charlotte Faculty Research Grant *(UNC-C FRG)*, the North Carolina Space Grant *(NCSG)* through the National Aeronautics and Space Administration *(NASA)*, the North Carolina Sea Grant *(NC Sea Grant)*, and the Research Triangle Nanotechnology Network *(RTNN)* Kickstarter award program supported through the National Science Foundation (NSF) grant number (Grant ECCS-1542015).

TABLE OF CONTENTS

TABLE OF FIGURES

LIST OF ABBREVIATIONS

A	Force matrix
B_{in}	Magnetic flux density
C_D	Drag coefficient
C_e	Cunningham correction factor
d_p	Particle diameter
E	Electric field
f_i	Resistance factor
f_0	Frequency
$\vec{F}_{ave}$	Average magnetic force
F_{bi}	Brownian force
F_D	Drag force
$\vec{F}_{ins}$	Instantaneous magnetic force
F_x	Body force
h	Distance from the channel ceiling
$\vec{H}$	Magnetic field
J	Current density
J_e	External current density
$\vec{M}_{eff}$	Effective magnetization
n_{Hb}	Molecular volume of hemoglobin
$N_{np,in}$	Number of particles entering the computational domain
$N_{np,out}$	Number of particles exiting the computational domain

P	Pressure
r	Particle radius
S	Oxygen saturation of oxyhemoglobin
s_f	Slip factor
$S_{n,ij}$	Spectral intensity
t	time
u	Ferrofluid velocity
u_p	Particle velocity
$v_{force,x}$	Particle force velocity
V_p	Particle volume
$v_{torque,x}$	Particle torque velocity
v_x	Particle linear velocity
$\hat{y}$	Y-position vector
μ	Ferrofluid dynamic viscosity
ρ	Ferrofluid density
ρ_p	Particle density
η_c	Capture efficiency
μ_0	Permeability of free space
μ_p	Particle permeability
μ_r	Relative permeability
φ	Phase angle

τ_{ave}	Average particle torque
$\vec{\tau}_{ins}$	Instantaneous torque
χ	Magnetic susceptibility
$\chi'_{deoxyHb}$	Molar magnetic susceptibility of deoxyhemoglobin
χ_{eff}	Effective susceptibility
χ_f	Ferrofluid susceptibility
χ_{globin}	Magnetic susceptibility of globin
χ_{Hb}	Magnetic susceptibility of hemoglobin
χ_{H2O}	Magnetic susceptibility of water
χ_{RBC}	Magnetic susceptibility of red blood cells (RBC)

CHAPTER 1: INTRODUCTION

1. Introduction and Background

1.1 Motivation

This thesis details the design and development of a simple traveling wave ferro-microfluidic device and system rig purposed for the potential manipulation and magnetophoretic separation of cells in a water-based ferrofluid. Ferrofluids have attracted significant attention due to their fascinating behavior since their discovery by NASA scientists [1]. Ferrofluids have been employed in several applications from aeronautics to medicine. Advances in rendering magnetic nanoparticles biocompatible have enabled their widespread use in medical applications such as in magnetic resonance imaging *(MRI)* as contrast enhancement agents, in drug delivery as drug carriers, and in hyperthermia for the selective destruction of tumor cells [2, 3]. Recent research focuses on ferrofluids use in cellular manipulation and separation [4].

Although cellular manipulation is a key step in many clinical settings, achieving this goal in high-efficiency and low-cost tools has been a challenging endeavor. Many conventional approaches require labor intensive and time-consuming protocols, have low throughput, and may result in cell damage [9]. There is an ever-increasing demand in clinical settings for smaller, practical, and personalized diagnostic tools that can be used in routine tests. The next section presents the state of the art in lab on chip devices.

1.2 Review of the State of the Art in Lab on a Chip Devices

Lab-on-a-chip devices for cellular manipulation and sorting are now being used in a variety of research applications involving cancer diagnosis, pathogen detection, and rapid genomic testing [5, 6]. Dielectrophoresis (DEP), immunolabeling, magnetic bead

separation, and laminar flow-based separation are some of the common techniques utilized [7-11]. In addition to current methods for cellular manipulation at the nano-scale, separation methods based on magnetic beads require labeling, as well as multiple and prolonged incubation and wash cycles.

Dielectrophoresis (DEP) has been widely reported as an exceptional technique for cell discrimination and isolation for biological sample processing, sorting of biological cells [12, 13], droplets [14, 15] and particles [15-18]. In a recent work done by Yamashita et al., this group established a method of high purification of platelets using DEP to eliminate blood cells from platelet concentrates [19]. Zhao et al. demonstrated the isolation of CTCs from blood cells by the combination of DEP and magnetophoresis in a microfluidic chip [20]. Li et al. [21] utilized DEP to separate live and heat-treated Listeria innocua cells. Gascoyne et al. [22] applied DEP to isolate malaria-infected cells from blood. Moon et al. [23] successfully separated human breast cancer cells *(MCF-7)* from a spiked blood cell sample by combining multi-orifice flow fractionation *(MOFF)* and DEP.

Song et al. [24] utilized a continuous-flow microfluidic device based on the accumulation of multiple DEP forces to sort stem cells and their differentiation progeny at different flow rates. Wang et al. proposed a novel microfluidic chip for the continuous separation of microalgae cells based on AC DEP [25]. Vahey et al. demonstrated the separation of polystyrene beads based upon surface conductance as well as sorting non-viable from viable cells of the budding yeast Saccharomyces cerevisiae through DEP [26]. Cao et al. [27] demonstrated highly effective enrichment of proteins by using nanoscale insulator-based DEP *(iDEP)* integrated with Ag/SiO_2 Nanorod Arrays. Kung et al. [28] utilized a tunnel DEP *(TDEP)* mechanism for continuously tunable, sheath less, 3D, and

single-stream microparticle and cell focusing in high-speed flows. Edwards and Hewlin recently developed a numerical simulation of DEP in a microfluidic device [11]. Conversely, schemes based on electric fields, DEP, suffer from high voltage requirements, have a performance that is highly dependent on the ionic strength of the solution [29, 30], and negatively affect cell metabolism and vitality by polarizing their membranes [31].

Using functionalized magnetic beads to separate target molecules and cells can overcome these challenges using magnetic fields instead of electric fields. The downside of this technique is the lengthy incubation times and wash cycles and the difficulty of removing the label post priori [32]. The deterministic hydrodynamics approach, as reported in the work of Davis et al. [33], can achieve high resolution separation without the use of any electromagnetic fields. However, high throughput with this device requires high-resolution lithography on a large area, keeping the cost per device high.

Table 1: A comparison of cell sorting and separation techniques and their abilities.

	Separation Mode	Purity(%)	Throughput	Label	Cost ($) Setup/Consumables	Typical Assay Run-time
FACS	Flow/electrostatic actuation	>88	~10^4 cells/s	Yes, fluo	>250,000/1000*	~1 hour
Immunomagneticic batch	Batch/magnetic actuation of label	>70	~10^6cells/s	Yes, magnetic	390/320***	~1 hour
Immunomagnetic flow	Flow/magnetic actuation of label	>99	10^3 cells/s	Yes, magnetic	~1000/300	~1 hour
Hydrodynamic	Flow/hydrodynamic forces	99	~3 cells/s	No	~1000/1 (estimated)	~1 hour *(for 1 µl blood)*
Dielectrophoresis	Batch or flow/electrodynamic actuation	95	~$3x10^3$ cell/s	No	~1000/1 (estimated)	10 minutes
Ferro-microfluidic	Batch or flow, ferrohydrodynamic actuation	88	~3x104 particles/s/mm^2	No	~100/1	~1 minute

There have been various works reported on using magnetic fields to separate cells in continuous microfluidic flow. Sutermaster and Darling investigated the ability of separating defined mixtures of alkaline phosphatase liver/bone/kidney *(ALPL)*-expressing

and non-expressing cell types using magnetic fields [34]. The results from this work showed that initial magnetic-activated cell sorting *(MACS)* runs performed using the manufacturer's recommended antibody and microbead concentrations produced inaccurate ALPL+ vs. ALPL− cell splits compared to fluorescence-activated cell sorting *(FACS)* when ALPL+ cells were present in larger proportions *(>~25%).* Shamloo et al. designed and developed two centrifugal microfluidic devices for the isolation of rare cancer cells [35]. These devices were tested at different disk rotational speeds, and it was reported that the passive design could isolate MCF-7 cells with a recovery rate of 76%.

Yang et al. investigated separating circulating tumor cells using a ferrohydrodynamic approach [36]. Liu et al. reported a separation method termed quantitative ferrohydrodynamic cell separation *(qFCS).* In this work, the authors were able to achieve multimodal rare cell sorting and simultaneous antigen profiling at a ~30,000 cells/min throughput with a 96.49% recovery rate and a 98.72% purity of recovered cells [37]. Although there has been some success in using this technique for separating living cells, the reported downsides of this technique are the lengthy incubation times and wash cycles and the difficulty of removing the label post priori [32, 38, 39]. The deterministic hydrodynamics approach, as reported in the work of Davis et al. [33], can achieve high-resolution separation without the use of any electromagnetic fields. However, high throughput with this device requires high-resolution lithography on a large area, keeping the cost per device high. There is also a small number of works that have investigated separating cells and magnetic materials in microfluidic devices using a traveling wave magnetic field [40-42]. More research is needed to investigate the ability to separate cells in continuous microfluidic flow using a traveling wave magnetic field [43].

To address performance limitations and the current knowledge gaps, our group aims to design and develop a microfluidic platform based on ferro-hydrodynamics for the manipulation and separation of cells and microorganisms within dynamic ferrofluids under an applied transient field. This work is similar to the work of Kose et al. [40]. This technique involves using a water-based ferrofluid as a uniform magnetic environment that surrounds the cells within a microfluidic channel. Cells and other nonmagnetic particles within the ferrofluid act as "magnetic voids" [44], in a manner comparable to electronic holes in a semiconductor. An externally applied magnetic field gradient attracts magnetic nanoparticles and causes nonmagnetic nanoparticles or cells to be effectively pushed away [45-48]. This principle has been applied in the author's earlier works to capture non-magnetic microparticles between magnetic film islands and in other microfluidic devices [49, 50].

The design reported in this work consists of integrated copper electrodes that carry alternating currents in quadrature to generate programmable magnetic field gradients locally for magnetic manipulation and separation of magnetic nanoparticles and non-magnetic microparticles within the ferrofluid. This paper details the design, methodology, and results. The key contributions of this work are:

1. A computational multi-physics model for predicting the magnetic and non-magnetic particle dynamics in the proposed ferro-microfluidic device.
2. A method for tailoring preferred size range *(10–20 nm)* magnetic cobalt ferrite magnetic nanoparticles.
3. The development of a ferro-microfluidic device for potentially separating cells and magnetic microparticles without detrimental thermal effects.

4. The development of a water-based ferrofluid with magnetic and non-magnetic particles as surrogates for biological cells.
5. The design and development of a rig for producing the electric field within the ferro-micro fluidic device for magnetizing the magnetic nanoparticles and manipulating nanoparticles in static and dynamic flow while efficiently removing heat from the electrode base.
6. A method for measuring the surrounding fluid and particle velocity, vorticity, and characterizing particle dynamics in the developed ferrofluid.

The next section discusses the ultimate goal and specific objectives of this work.

1.3 Ultimate Goal and Specific Objectives

The ultimate goal of this thesis is to design and develop a ferro-magnetic microfluidic device for label-free magnetic manipulation and separation of microparticles and cells within biocompatible ferrofluids. The specific objectives of this work are listed below:

1. Develop a multi-physics computational model for analyzing the magnetic field, particle dynamics, and particle capture efficiency for design optimization of the proposed ferro-magnetic microfluidic device.
2. Develop a magnetic rig for producing the magnetic field in the ferro-microfluidic device and observing particle dynamics under a microscope objective.
3. Tailor a ferrofluid with magnetizable particles that can be manipulated under an applied magnetic field and are bio-friendly with attaching cells.
4. Conduct experimental studies to characterize particle dynamics under varying applied magnetic field strengths and frequencies.

The next chapter discusses the methodology of this work.

CHAPTER 2: METHODOLOGY

This chapter provides an overview of the materials and methodology of this work. The order of the topics in this chapter is as follows: (1) an overview of the theory and numerical simulation methodologies, (2) the ferro-microfluidic device and system rig design and development and assembly methodology, (2) the heat dissipation system design methodology, and (3) the ferrofluid tailoring and preparation methodology. The next section introduces the numerical simulations for this work.

2.1 Numerical Modelling

2.1.1 Numerical Modelling Theory

In this work, particle transport and capture efficiency are predicted in the proposed system design using a developed multi-physics computational model that considers the dominant magnetic and hydrodynamic forces as well as coupled particle-fluid interactions. The model is based on a coupled Eulerian-Lagrangian computational fluid dynamics *(CFD)* based numerical scheme combined with analytical magnetic analysis for the magnetic force. The Lagrangian analysis is used to track the motion of individual particles while a Eulerian-based CFD analysis is used to solve the Navier Stokes momentum equations. The transfer of momentum from the particles to the fluid is achieved by introducing a particle force sink into the Navier Stokes equations. The ability to evaluate two-way particle-fluid coupling is an important feature of our model that distinguishes it from most other models used in this field that are limited to one-way particle-fluid coupling, which neglects the effects of particle motion on fluid flow [51-54].

An additional key aspect of the presented model is that a hybrid closed-form/numerical approach is implemented that combines numerical transport analysis with closed-form field

analysis. The use of closed-form magnetic analysis provides an exact prediction of the magnetic field and force in the microchannel and is computationally more efficient and accurate than numerical field analysis, which is more commonly used for this analysis. It should be noted that while the transport equations are solved in a confined computational domain *(i.e., the microchannel);* the magnetic analysis requires a larger *(open)* domain because the field extends to infinity. Additionally, accurate magnetic force values depend on the gradient of the field, which depends on the resolution of the grid. Normally, many computational nodes are required to achieve an accurate magnetic analysis, which increases computation time and inhibits large-scale parametric analysis. The closed-form magnetic analysis used here overcomes these limitations and enables rapid parametric studies of particle manipulation for systems with extended and complex magnetic structure. The next section presents an overview of the derived magnetic computational model.

2.1.2 Particle Magnetization Model Theory

Contrary to the previous model involving analyzing particle dynamics in a static magnetic field due to an array of conductive elements and a using mathematical superposition method to model the magnetic field [55], this section presents a simplistic magnetization model analytical approach. This approach provides a basis for estimating the particle velocities and critical frequencies in the travelling wave ferro-microfluidic device. In this effort, we begin with assuming a perfectly spherical, incompressible microparticle submersed in a magnetically linear ferrofluid with a slip factor "s_f" that is independent of the magnetic field magnitude and frequency. We further assume that the spherical particle radius "r" is small relative to the wavelength of the travelling wave

magnetic field "$\vec{H}$" as determined by electrode dimensions and spacing. This is done such that the following relationship is met:

$$r\left|\nabla\vec{H}\right| \ll \left|\vec{H}\right| \quad \textbf{(1)}$$

Under this assumption and condition, the ferrofluid magnetization in surrounding the microparticle, along with the particle's internal magnetization (M_{eff}) is uniform. We also further approximate any field value as constant within the microparticle's interior. The total instantaneous force is calculated as:

$$\vec{F}_{ins} = \int_{V_p} \nabla\left(\vec{M}_{eff} \cdot \vec{B}_{in}\right) dV \quad \textbf{(2)}$$

where B_{in} is the magnetic flux density in the microparticle's interior, and the integration is over the internal volume of the particle. Under these assumptions, the surface terms in (2) due to discontinuities in M and B create pressure terms that integrate out to 0, and a simple vector expansion of the integrand reveals that this term is the same as the Kelvin force density. As a result, the instantaneous force expression can be simplified to

$$\vec{F}_{ins} = V_P \nabla\left(\vec{M}_{eff} \cdot \vec{B}_{in}\right) \quad \textbf{(3)}$$

To obtain an analytical expression for the magnetic force, we express M_{eff} and B_{in} in terms of the external time-dependent magnetic field (H_{ext}) in the absence of the microparticle, since this field value can be easily obtained from simple simulations. The net magnetization of the particle with a magnetic particle and fluid permeability μ_p and μ_f within the ferrofluid depends on H_{ext} as follows:

$$\vec{M}_{eff} = 3\left(\frac{\mu_p - \mu_f}{\mu_p + 2\mu_f}\right)\vec{H}_{ext} \quad \textbf{(4)}$$

which can be rearranged in terms of material susceptibility:

$$\vec{M}_{eff} = \frac{3\chi}{3+2\chi_f}\vec{H}_{ext} \quad \textbf{(5)}$$

Determining the magnetic flux density and field within the particle requires consideration of the demagnetization field inside it. The overall magnetic field inside the microparticle is described as:

$$\vec{H}_{in} = \vec{H}_{ext} - \vec{H}_{dmag} \quad \textbf{(6)}$$

With the field demagnetization for the microparticle described as:

$$\vec{H}_{dmag} = \frac{\vec{M}_{eff}}{3} \quad \textbf{(7)}$$

In the linear regimes where the microparticle magnetization can be written in terms of the effective susceptibility and the internal magnetization, the effective magnetization can be written as:

$$\vec{M}_{eff} = \left(\frac{3\chi_{eff}}{3+\chi_{eff}}\right)\vec{H}_{ext} \quad \textbf{(8)}$$

The effective susceptibility can be written as:

$$\chi_{eff} = \frac{-\chi_f}{1+\chi_f} \quad \textbf{(9)}$$

where χ_f is the ferrofluid susceptibility.

The effective magnetic susceptibility depends on the ferrofluid, given that the microparticle responds to magnetic forces only because it displaces the ferrofluid and creates a *"magnetic hole"*. In that regard, the magnetic medium in which the hole resides determines the strength of the interactions between that magnetic hole and applied fields.

The negative sign indicates that the effective magnetization of the microparticle is in the opposite 3 direction of the local ferrofluid magnetization under static conditions. While $\chi_{eff} \approx -\chi_f$ for $\chi_f << 1$. The effective susceptibility of the magnetic hole approaches -1 in a strongly magnetizable medium. In effect, using too strong a ferrofluid for microparticle manipulation could be counterproductive. With much mathematical manipulation, the average magnetic force on the particle can be expressed as

$$F_{ave} = \frac{1}{2} V_p \mu_0 \left(\frac{\mathrm{Re}\left[\chi_{eff} \right]}{\left| \chi_{eff} \right|^2} + 1 \right) \left(\frac{9\left| \chi_f \right|^2}{9 + 6\,\mathrm{Re}\left[\chi_f \right] + 4\left| \chi_f \right|^2} + 1 \right) \vec{\nabla} \left| \vec{H}_{ext} \right|^2 \qquad \textbf{(10)}$$

Similarly, the instantaneous torque on a magnetic microparticle is given by

$$\vec{\tau}_{ins} = s_f V_p \left(\vec{M}_{eff} \times \vec{B}_{in} \right) \mathrm{r} \qquad \textbf{(11)}$$

we have allowed for the possibility that the rotation of the microparticle may be subject to a s_f between 0 and 1. This slip factor represents the ratio of the torque that a non-magnetic microparticle experiences in our ferro-microfluidic device to the value of the torque that would be felt by an isolated particle of the same size and effective magnetization. The remaining details of the derivation for magnetic torque mirror those for magnetic force [56]. The next section discuss the device geometry and modelling in COMSOL.

$$\tau_{ave} = \frac{\hat{y}\, s_f V_p \mu_0}{2} \left(\frac{\mathrm{Im}\left[\chi_{eff} \right]}{\left| \chi_{eff} \right|^2} \right) \left(\frac{9\left| \chi_f \right|^2}{9 + 6\,\mathrm{Re}\left[\chi_f \right] + 4\left| \chi_f \right|^2} + 1 \right) \vec{\nabla} \left| \vec{H}_{ext} \right|^2 \qquad \textbf{(12)}$$

2.1.3 Device Geometry and Mesh Modelling Methodology

COMSOL v. 2019 commercial finite element Multiphysics analysis software was used to model a 2-D representation of the ferro-microfluidic system, the ferrofluid flow, calculate the external magnetic field "H_{ext}" through from the electrodes to the surrounding

medium, and calculate the time averaged particle velocity, torque, and magnetic force. A snapshot of a 3-D CAD drawing of the ferro-microfluidic device including the electronic chip base and the PDMS microchannel device developed in Solidworks™ v22 is shown below in *Figure 1*. As shown in *Figure 1*, the electronic chip base contains 12 identical conductive copper electrodes that are arranged in quadrature via copper wire bonds to create a periodic magnetic landscape via phase differenced current inputs *(0°,90°,180°, and 270°).* Each electrode has a width of 240µm and height of 30µm. Although not shown, a thin 1µm layer of PDMS separated the channel from the electrodes to prevent shorting. The PDMS microchannel device includes a simple single microchannel with a total height of 100µm and a length of 5000µm.

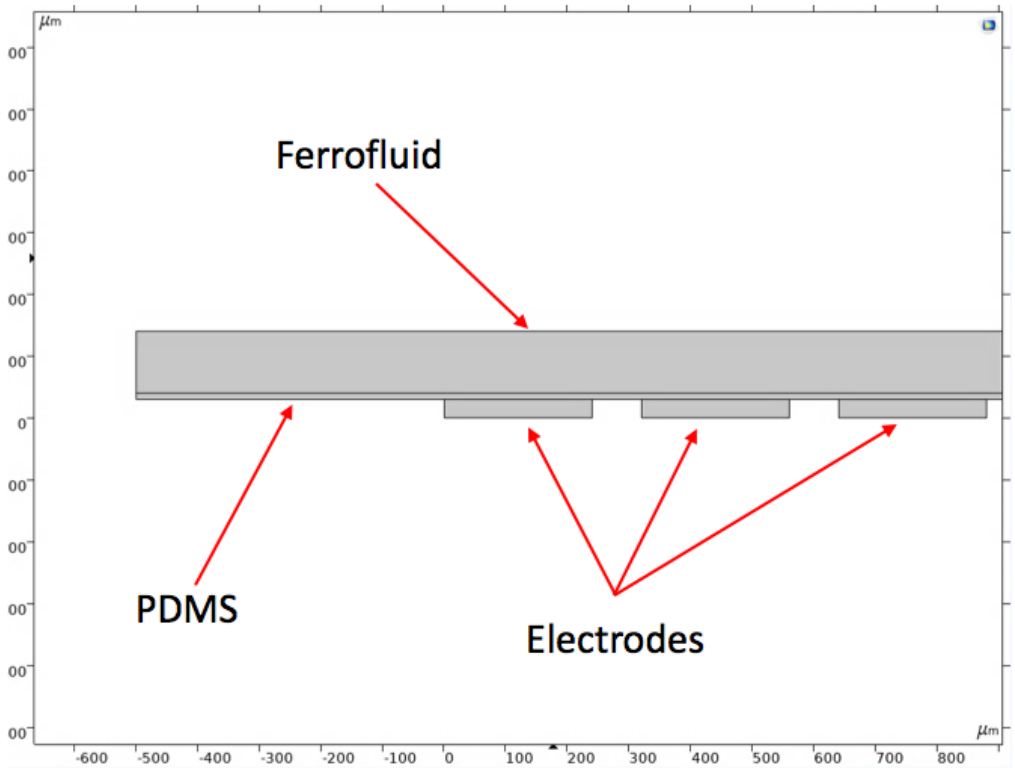

Figure 1: Enlarged view snapshot of the 2-D ferro-microfluidic system modelled in COMSOL.

For the COMSOL simulations, a 2-D representation of the device presented in ***Figure 1*** was developed and analyzed. For 2-D model development, the flow is assumed to be symmetric about the x-coordinate axis as shown in ***Figure 1***. As a result, the z-direction was neglected for the 2-D model development. The 2-D model was created in COMSOL. ***Figure 2*** provides a snapshot of the 2-D model generated in COMSOL with the boundary condition assignment for pre-processing.

For the 2-D modelling, the surrounding ambient air is not modelled in this system. Only the ferrofluid, electrodes and the thin PDMS layer separating the ferrofluid and the electrodes are modelled. The flow of the ferro-fluid is modelled as a steady laminar flow. In this flow regime, inertial effects are neglected, and the Stokes flow equations dominate the hydrodynamics. The computational mesh is shown below in ***Figure 2***.

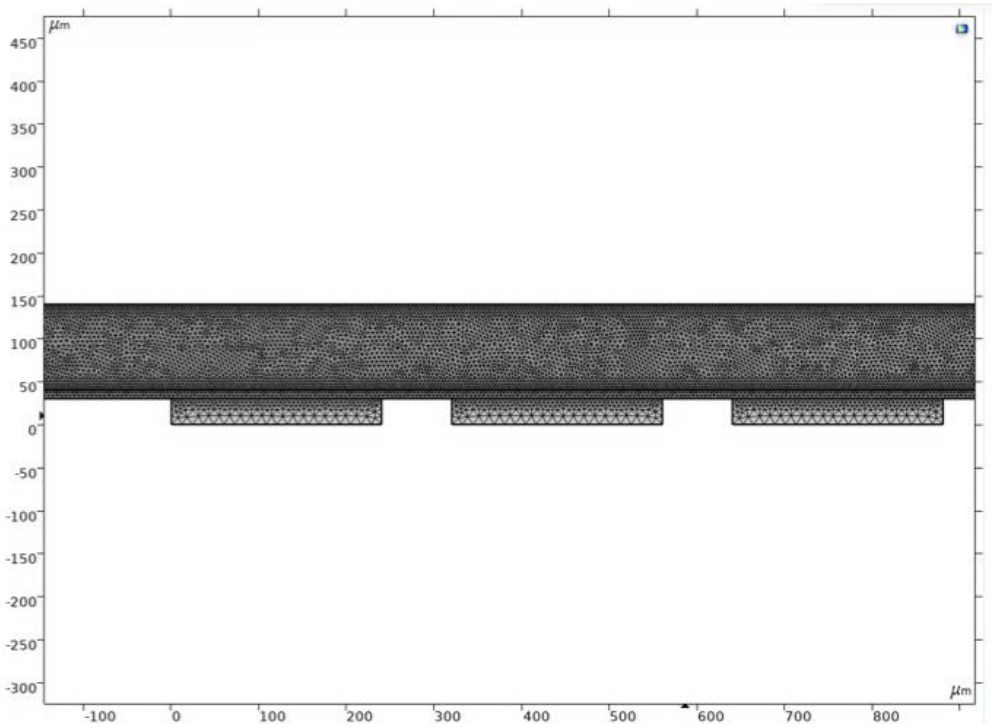

Figure 2: Snapshot of the 2-D ferro-microfluidic system model mesh (coarse).

The computational mesh consists of 568,524 tetrahedral elements at which grid independence was achieved. For grid independence, the model was meshed using a range of COMSOL intervals *(e.g., very coarse, coarse, fine, very fine, etc.)*, until the average velocity for laminar flow reached less than 5% difference in error in comparative values between mesh runs. This chosen mesh also allowed enough resolution to resolve the magnetic field strength and intensity values around the electrodes as well as provided enough collateral for memory when running large frequency studies (f_0>1kHz).

2.2 Fluid and Particle Flow Modelling Methodology

For fluid flow simulations, the laminar steady flow solver was employed that utilizes the continuity and Navier-Stokes equation in a finite element form shown below in (13) to calculate the velocity flow field. The laminar steady flow solver assumes that the flow is constant and time-independent [57, 58]:

$$\nabla \cdot u = 0 \quad \textbf{(13)}$$

$$\rho\left(\frac{\partial u}{\partial t} + u\left(u \cdot \nabla\right)\right) = -\nabla p + \nabla \cdot \left(\mu \nabla u\right) \quad \textbf{(14)}$$

The boundary conditions imposed for the microfluidic computational model include a constant velocity condition of 1μm/s for the inlet, a no-slip boundary condition imposed for the microchannel base and ceiling wall, and a pressure outlet condition at the outlet. The working fluid was modelled using the fluid properties of water along with cobalt ferrite and RBCs and E. Coli magnetic properties selected for the magnetic and non-magnetic particles as mentioned previously. The next section discusses the transient magnetic field methodology and relations.

2.3 Transient Magnetic Field Relations

COMSOL's AC/DC module was used to simulate the external magnetic field due to the electrodes. The electrodes are modelled as individual magnetic coils with one wire turn and a sinusoidal input current.

$$\nabla \times E = -\frac{\partial B}{\partial t} \quad \textbf{(15)}$$

Here the electric field E is computed from the current density, using the constitutive relationship:

$$E = E_m(J - J_e) + v \times B \quad \textbf{(16)}$$

Where J_e is an external generated current density, v is the relative velocity of the domain in the physics interface. The total current density J, is obtained from Ampere's Law:

$$\nabla \times H = J \quad \textbf{(17)}$$

To calculate the transient magnetic field, COMSOL uses the Faraday's law:

$$\nabla \times \left(E_m(J - J_e) + v \times B \right) + \frac{\partial B}{\partial t} = 0 \quad \textbf{(18)}$$

More theory from the AC/DC module can be found in the COMSOL reference manual [59]. The next section discusses the microparticle trajectory model.

2.4 Particle Trajectory Model

A discrete phase model *(DPM)* was implemented in the present work to calculate the trajectory of microparticles. This model is the same model used in our previous work of magnetic drug targeting. The trajectory of the particles is predicted by integrating the force balance on the particle cluster, which is written in a Lagrangian reference frame. The force balance equates the particle cluster inertia with the forces acting on the particles and can be expressed as:

$$\frac{du_p}{dt} = F_D(u - u_p) + \frac{g_x\left(\rho_p - \rho\right)}{\rho_p} + F_{bi} + F_x \tag{19}$$

where u is the fluid velocity, u_p is the particle parcel velocity, ρ is the fluid density, ρ_p is the particle density, F_{bi} is the Brownian force acceleration term, F_x is the body force acceleration term, d_p is the particle diameter, and $F_D(u-u_p)$ is the drag force per unit mass and is written as:

$$F_D = \frac{18\mu}{\rho_p d_p^{\,2}} \frac{C_D \,\mathrm{Re}}{24} \tag{20}$$

The relative Reynolds number, *"Re"* is defined as:

$$\mathrm{Re} = \frac{\rho d_p \left|u_p - u\right|}{\mu} \tag{21}$$

the drag coefficient, "C_D" is defined as:

$$C_D = a_1 + \frac{a_2^{\,2}}{\mathrm{Re}} + \frac{a_3^{\,3}}{\mathrm{Re}^2} \tag{22}$$

where a_1, a_2, and a_3 are constants that apply for smooth particles using the spherical drag law and apply over a range of Reynolds numbers as reported by Morsi and Alexander [60]. For the present work, when substituting the appropriate constants, the drag coefficient takes the following form for micron sized particles:

$$C_D = \frac{24}{\mathrm{Re}}\left(1 + b_1 \mathrm{Re}^{b_2}\right) + \frac{b_3 \,\mathrm{Re}}{b_4 + \mathrm{Re}} \tag{23}$$

where

$$b_1 = \exp(2.3288 - 6.4581\phi + 2.4486\phi^2)$$
$$b_2 = 0.0964 + 0.5565\phi$$
$$b_3 = \exp(4.905 - 13.8944\phi + 18.4222\phi^2 - 10.2599\phi^3)$$
$$b_4 = \exp(1.4681 + 12.2584\phi - 20.7322\phi^2 + 15.8855\phi^3)$$

which is adapted from Haider and Levenspeil [61]. The shape factor, "ϕ" is defined as:

$$\phi = \frac{s}{S} \tag{24}$$

Where *s* is the surface area of a sphere having the same volume as the particle, and *S* is the actual area of the particle. The shape factor, which is a unitless ratio, cannot exceed a numerical value of 1. For superparamagnetic particles, a form of Stokes drag law is used [62]. In this case, the drag force on a particle per unit mass is defined as:

$$F_D = \frac{18\mu}{d_p{}^2 \rho_p C_e} \tag{25}$$

where the Cunningham correction factor C_e is described as:

$$C_e = 1 + \frac{2\lambda}{d_p}\left(1.257 + 0.4e^{-(1.1 d_p/2\lambda)}\right) \tag{26}$$

and λ is the molecular mean free path. For superparamagnetic particles, the effects of Brownian motion are included. The components of the Brownian force are modeled as a Gaussian white noise process with spectral density given by $S_{n,ij}$.

$$S_{n,ij} = S_0 \delta_{ij} \tag{27}$$

where δ_{ij} is the Kronecker delta function and:

$$S_0 = \frac{216 \nu k_B T}{\pi^2 \rho d_p{}^5 \left(\frac{\rho_p}{\rho}\right) C_e} \tag{28}$$

T is the absolute temperature of the fluid *(taken as body temperature)*, ν is the kinematic viscosity, and k_B is the Boltzmann constant. The Brownian force per unit mass component is described as:

$$F_{bi} = \zeta_i \sqrt{\frac{\pi S_0}{\Delta t}} \tag{29}$$

where ζ_i is the zero-mean unit-variance-independent Gaussian random number. The next section discusses the particle velocity calculation methodology.

2.5 Particle Velocity Calculation Methodology

The magnetic and non-magnetic particle velocities were calculated in COMSOL's post-processor. Given that the flow is laminar, the viscous drag and magnetic forces determine microparticle dynamics. Given this fact, all hydrodynamic coefficients involved can be combined into the resistance matrix shown below to determine particle velocities during post-processing:

$$\begin{bmatrix} F_{ave} \\ \tau_{ave} \end{bmatrix} = A \begin{bmatrix} v_x \\ \varpi_y \end{bmatrix} \tag{30}$$

where,

$$A = \begin{pmatrix} 6\pi\eta R f_1(h,R) & 6\pi\eta R^2 f_2(h,R) \\ 8\pi\eta R^2 f_3(h,R) & 8\pi\eta R^2 f_3(h,R) \end{pmatrix} \tag{31}$$

In this arrangement, v_x is the linear velocity of the microparticle along the channel length, ω is its angular velocity, η is the ferrofluid viscosity, r is microparticle radius, and f_i is a resistance factor that depends on particle radius and its distance *(h)* from the channel ceiling. Assuming that h << R, these resistance factors can be obtained from the standard lubrication theory as:

$$\begin{aligned} f_1 &= -\frac{8}{15}\ln\left(\frac{h}{R}\right) + 0.9588, \quad f_2 = -\frac{2}{15}\ln\left(\frac{h}{R}\right) + 0.2526 \\ f_3 &= -\frac{1}{10}\ln\left(\frac{h}{R}\right) - 0.1895, \quad f_4 = -\frac{2}{5}\ln\left(\frac{h}{R}\right) + 0.3817 \end{aligned} \tag{32}$$

We estimate *h* through the Derjaguin, Landau, Verwey and Overbeek theory (DLVO theory) [63] using the surface charge density on the microparticle and the channel surfaces, and the ionic conditions within the ferrofluid. The vertical force ($F_{ave,y}$) that pushes the microparticles up to the channel ceiling is on the order of nN's and we expect them to be close to touching the channel wall. The matrix can then be solved for v and omega through a matrix inversion operation:

$$A^{-1} = \frac{\begin{pmatrix} 6\pi\eta R f_1(h,R) & 6\pi\eta R^2 f_2(h,R) \\ 8\pi\eta R^2 f_3(h,R) & 8\pi\eta R^2 f_3(h,R) \end{pmatrix}}{48\pi^2\eta^2 r^4 G} \quad \textbf{(33)}$$

Here, $G=f_1f_4-f_2f_3$ has been defined for notational convenience. Hence, particle linear velocities due to magnetic force and torque alone can be determined:

$$v_{force,x} = \frac{f_4}{6\pi\eta r G} F_{ave} \quad \textbf{(34)}$$

The velocity due to the torque can be determined from:

$$v_{force,x} = -\frac{s f_2}{8\pi\eta r^2 G} \tau_{ave,y} \quad \textbf{(35)}$$

The net particle velocity can then be calculated from the combination of the force and torque velocity shown below:

$$v_x = v_{force,x} + v_{torque,x} \quad \textbf{(36)}$$

The next section presents the microparticle capture efficiency methodology.

2.6 Particle Capture Efficiency

Capture efficiency is a major parameter of interest in this work. Capture efficiency describes the effectiveness of targeting particles under the influence of a magnetic field. The capture efficiency for the magnetized section of ferro-microfluidic device is defined

as the ratio of the number of injected particle parcels to the number of particle parcels leaving the magnetized region:

$$\eta_c = \frac{N_{np,in}}{N_{np,out}} \times 100\% \quad \textbf{(37)}$$

The capture efficiency is determined via comparing the number of injected particle parcels $N_{np,in}$ to the number of escaped particle parcels $N_{np,out}$ as described in (37). The next section discusses magnetic susceptibility and relative permeability methodology.

2.7 Magnetic Susceptibility and Relative Permeability Methodology

The relative permeability of both magnetic and non-magnetic entities was input into COMSOL's pre-processor for modelling the particle dynamics in the proposed device design reported in this work. The magnetic permeabilities are modelled in terms of the magnetic susceptibility in the relation below:

$$\mu_r = 1 + \chi \quad \textbf{(38)}$$

where μ_r is the relative permeability and χ is the susceptibility of the medium analyzed *(cobalt ferrite, E. Coli, and red blood cells).*

The magnetic susceptibility of cobalt ferrite magnetic particles is modelled as χ=1.4 after cobalt ferrite [64-66]. The magnetic susceptibility of E. Coli cells is modelled as $\chi=1.0\text{x}10^{-6}$ [67]. For the magnetic susceptibility of red blood cells *(RBCs)*, the RBC magnetic susceptibility was calculated relative to that of the ferrofluid from an approach we adopted from the work of Zborowski and Spees et al. [68, 69]. The work of Spees et al. [69] is based on an early work by Cerdonio et al. [70, 71] in which the RBC volume magnetic susceptibility is the weighted sum of the susceptibilities:

$$\chi_{RBC} = \chi_{H2O}\chi_{H2O} + (1-S)\chi_{Hb}\chi_{deoxyHb} + \chi_{globin}\chi_{globin} \quad \textbf{(39)}$$

where χ_{H2O} and $\chi_{H2O,}$ $(1\text{-}S)\chi_{Hb}$ and $\chi_{deoxyHb,}$ χ_{globin}, and χ_{globin} are the volume fractions and volumetric magnetic susceptibilities of water, deoxyhemoglobin and the protein *(globin)* part of the hemoglobin molecule, respectively; and *S* is the oxygen saturation of oxyhemoglobin. Here, $\chi_{H2O}=1\text{-}n_{HbnHb}$, where n_{Hb}=5.5mM is the total intracellular hemoglobin concentration, n_{Hb} = 48,277cm^3 /mol is the molar volume of hemoglobin, $\chi_{deoxyHb} = \chi'_{deoxyHb}$, , where $\chi'_{deoxyHb}$=50,893x10^{-6} cm^3/mol is the molar susceptibility of deoxyhemoglobin, and χ_{globin} $\chi_{globin}=n_{Hb}M_{Hb}\chi''_{globin}$ where M_{Hb}=64,450 is the molecular weight of hemoglobin, and χ_{globin}=0.580x10^{-6} cm^3/g is the specific susceptibility of globin in the hemoglobin molecule. The susceptibility values are given in the cgs unit system to facilitate comparison with the literature data; the conversion to values in the SI unit system requires multiplication by 4π. The metHb contribution to the erythrocyte magnetic susceptibility has a similar form as the one above:

$$\Delta\chi = \chi_{RBC} - \chi_{H2O} \quad \textbf{(40)}$$

Where χ_{H2O}=-0.719x10^{-6} is the magnetic susceptibility of water. χ of RBCs in water was determined to be -0.0147×10^{-6}. The relative permeability values modelled in COMSOL are μ_r =2.4 for cobalt ferrite, μ_r =1 for RBCs in water and E. Coli. In this work, a simplified assumption was applied to the RBCs in that they are modelled as spherical as opposed to elliptical. It was also assumed that this would have a minimal effect on magnetic manipulation or particle transport. Spherical assumptions have been made in prior works for RBCs [72-76]. Similarly, macro level flows have considered on the viscosity of blood as opposed to modelling individual cells [77-79]. The next section discusses the experimental setup.

2.8 Experimental Setup

The ferro-microfluidic particle manipulation device used in our experiments consists of two parts: the microfluidic channel and the underlying programmable copper electrode circuit board chip. The electrodes *(30 µm high, 300 µm wide and 2 cm in length)* were fabricated by an external consultant *(Sigenics Inc)*. The electrodes were fabricated via wet etching the copper layer of a thermal-clad printed circuit board *(on an insulated metal substrate)* through a photoresist mask. The electrodes were bonded via internal board wire junctions to complete the quadrature electrode circuit *(currents phased at 0°, 90°, 180°, and 170°)*. A photo of the developed chip is shown below in *Figure 3*.

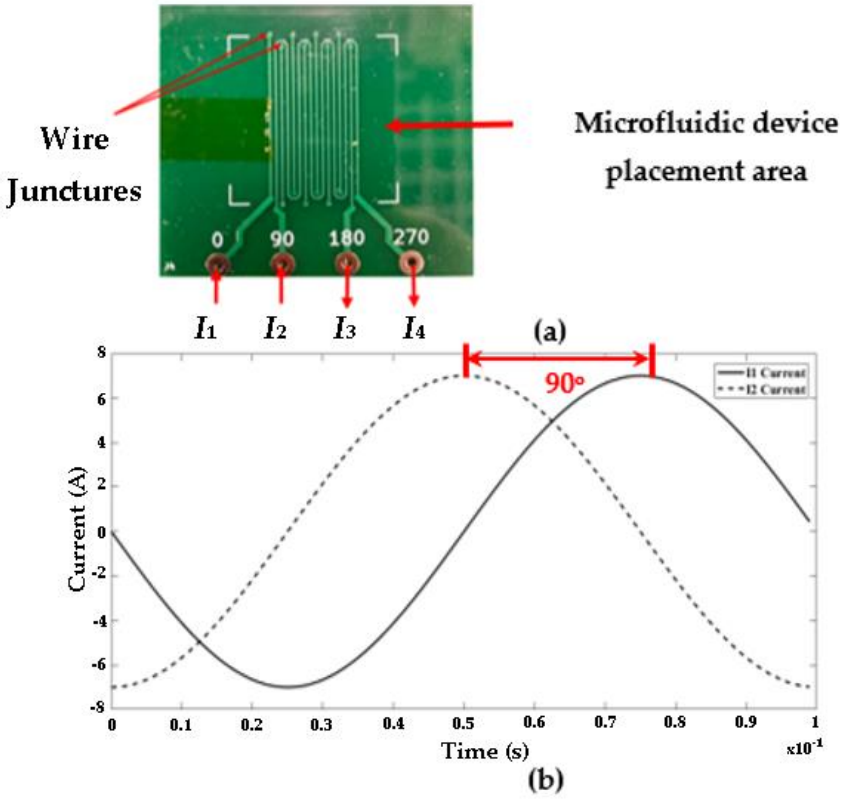

Figure 3: Overview of the programmable chip platform and current waveform: (a) Photo of the first fabricated programmable electronic chip base. The arrows going in represent the current amplitudes supplied to the chip at a 90° phase and the arrows coming from the chip represent the output currents at a 90° phase difference. (b) The current sinusoidal input current waveforms for I_1 and I_2.

In this work, a travelling magnetic field is generated in the channel by applying alternating currents in quadrature to a single layer of electrodes. A plot of the input current profiles for both inputs at 7A and 10 kHz is shown in *Figure 3b*. The microfluidic channel *(20 µm to 100 µm high, 1 mm to 3mm wide and 2 cm to 3cm long)* was prepared from polydimethylsiloxane *(PDMS)* stamps through soft lithography and was bonded to a glass slide that acts as an insulating layer between the channel and the electrodes. The channel height was chosen to be well below the optimum for localized ferrohydrodynamic flow to minimize its potential effects on microparticle migration. For PDMS removal, the PDMS is allowed to cure, and the microfluidic device is easily peeled off from the salinized SU-8 master. The fluidic connection holes are punched with a syringe needle. The SU-8 master can be reused as many times as needed to create additional PDMS devices.

The PDMS channel device was treated via plasma treatment *(in a plasma cleaner chamber from Harrick Scientific, Pleasantville, NY)* at 90 mmHg O_2 partial pressure with 18 W power for one minute. This enables the PDMS to be rendered hydrophilic and allows the PDMS and glass components to create a strong bond. The PDMS was then bonded to the glass slide. This attachment is sustained via oxygen bonds between silanol groups, formed on the PDMS surface via plasma treatment.

Once the microfluidic device is fully assembled, it is placed over a cooling water block *(the cooling block is discussed in section 2.8)* with a thin layer of a silver-thermal conductive paste and glue *(8349TFM MG Chemicals Thermal adhesive)* to dissipate heat. The electrode pads are connected to a stereo-amplifier *(Crown Com-Tech 410, 2-Channel Power Amplifier)* with connection cables to both channels. A resistor bed was created from

2Ω resistors wired in series to avoid large current pulses during startup of the stereo-amplifier. A schematic of the electronics setup is shown below in *Figure 4*.

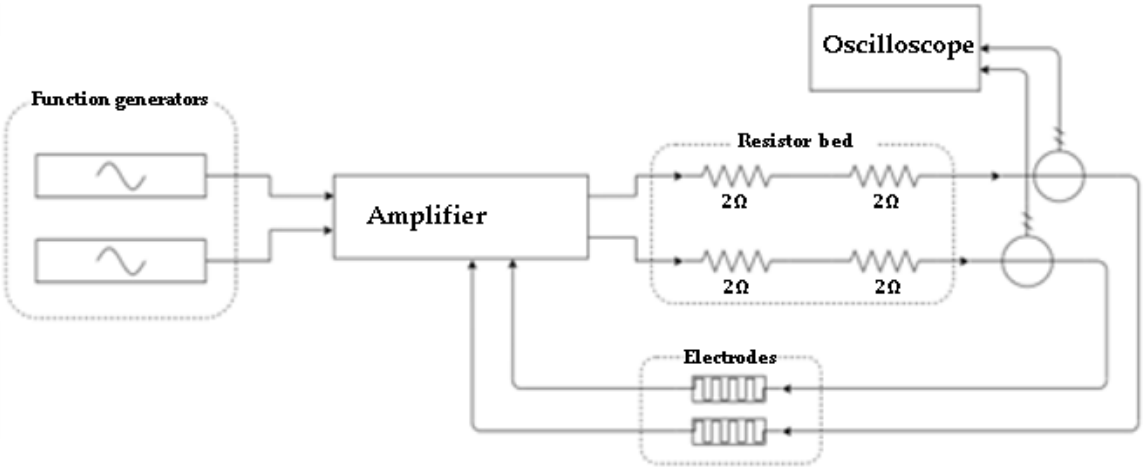

Figure 4: Schematic diagram of the experimental rig electronic components.

A 3-D resistor housing was 3-D printed to cover the resistors and two CPU fans were installed on top of the housing to cool the resistors during experimental runs. Two function generators from Agilent *(33220A Function/Arbitrary Waveform Generator, Santa Clara, CA)*, are phase-locked to each other to generate the sinusoidal signal and the resulting current is amplified with the stereo-amplifier. The current is measured by two current probes from Tektronix *(TCPA 300, TCP 305, Richardson, TX)* connected to the cables. An oscilloscope *(Tektronix, TDS 2014, Digital Oscilloscope)* is connected to the current probes and monitors the current. A Ziess Axioplan 2 microscope outfitted with a camera is used to record images of the ferrofluid and fluorescent microparticle mixture dynamics under an applied field. The current amplitude and frequency as well as the phase difference between the two channels are controlled by a MATLAB program. A photo of the experimental setup is shown in *Figure 5*. The next section discusses the heat dissipation system design methodology.

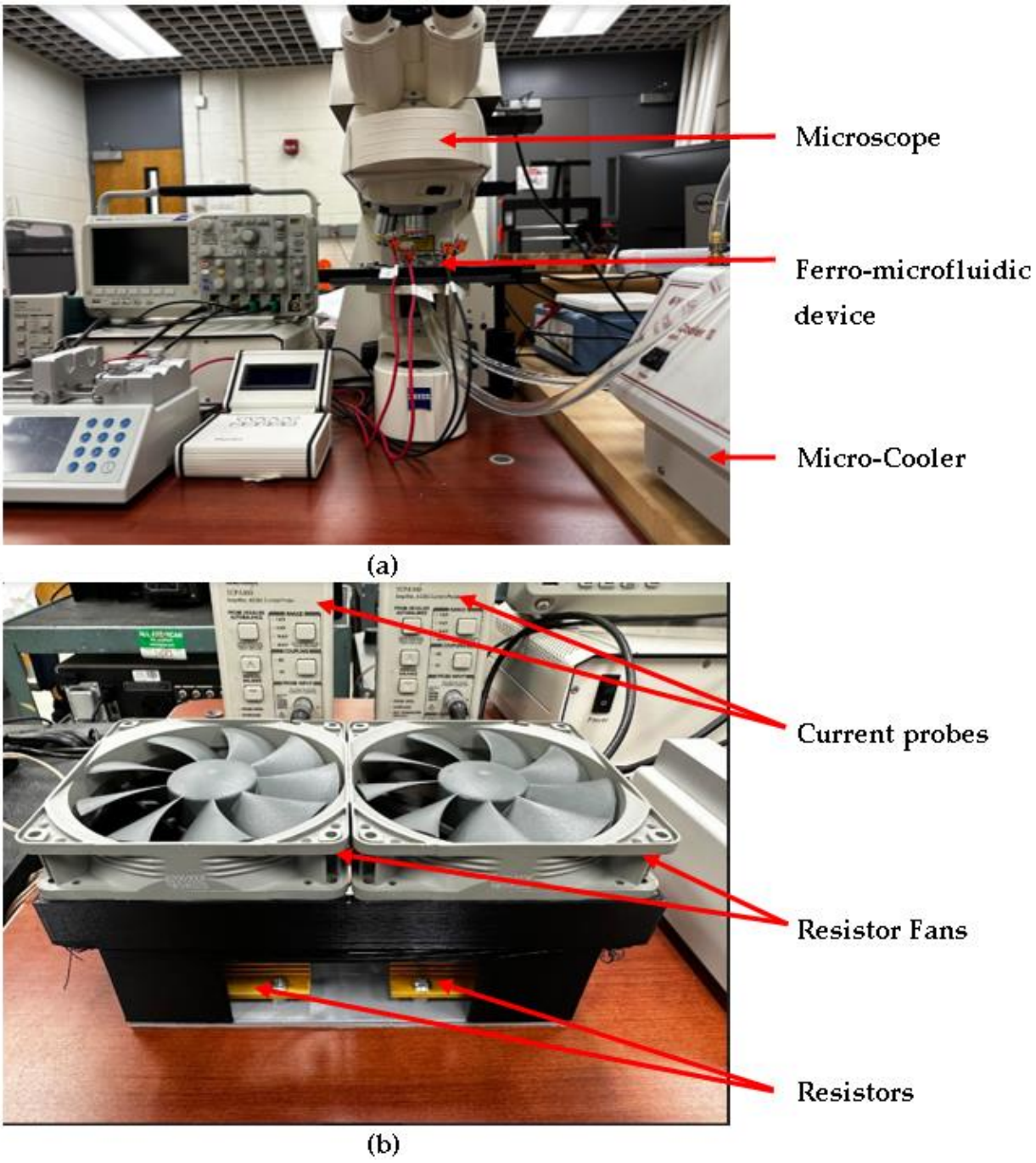

Figure 5: Photograph of the experimental rig setup: (a) Microscope and cooling system setup with the oscilloscope and (b) the 3-D printed resistor housing and cooling setup.

2.9 Heat Dissipation System Design, Development and Evaluation

The programmable electronic chip base is designed to operate with current levels of 1-7 A and covering a large frequency spectrum range *(10 Hz-1kHz).* At these current levels, heating of the device and critical thermal change to the electrodes is a vital concern. We've conducted a simple initial computational thermal heat load analysis using Solidworks™ Thermal Simulation package v.22 to provide a baseline perspective of the temperature range for the low and high heat loads. In this analysis, we conducted a low and high thermal power load assessment based on the minimum and maximum current settings of 1A and 7A.

For pre-processing, we deployed the CAD model into the thermal simulation package of Solidworks™ and applied PCB PR4 thermal material properties to the circuit board and copper thermal material properties to the electrodes. An ambient initial temperature setting of 300K was applied to the top and side faces of the model. A convection coefficient *(also called the film coefficient)* of 25 $(W/m^2)/K$ was applied. The value of the convection coefficient corresponds to natural convection taking place without a fan. Two heat load settings were applied to the electrodes for a low setting of 2 W and a high setting of 8 W. We assumed that the electrodes would experience a 0.5 Ω resistance. Using the formula for electrical power, these settings are representative of 2 and 4 amps. For meshing, a mesh control of 3 µm was applied to the electrodes and the final mesh was set to the finest meshing scheme. The resulting mesh contained 1,171,391 tetrahedral elements. This was the maximum number of elements that could be used to avoid memory and ram issues. *Figure 6* below shows the model and meshed result.

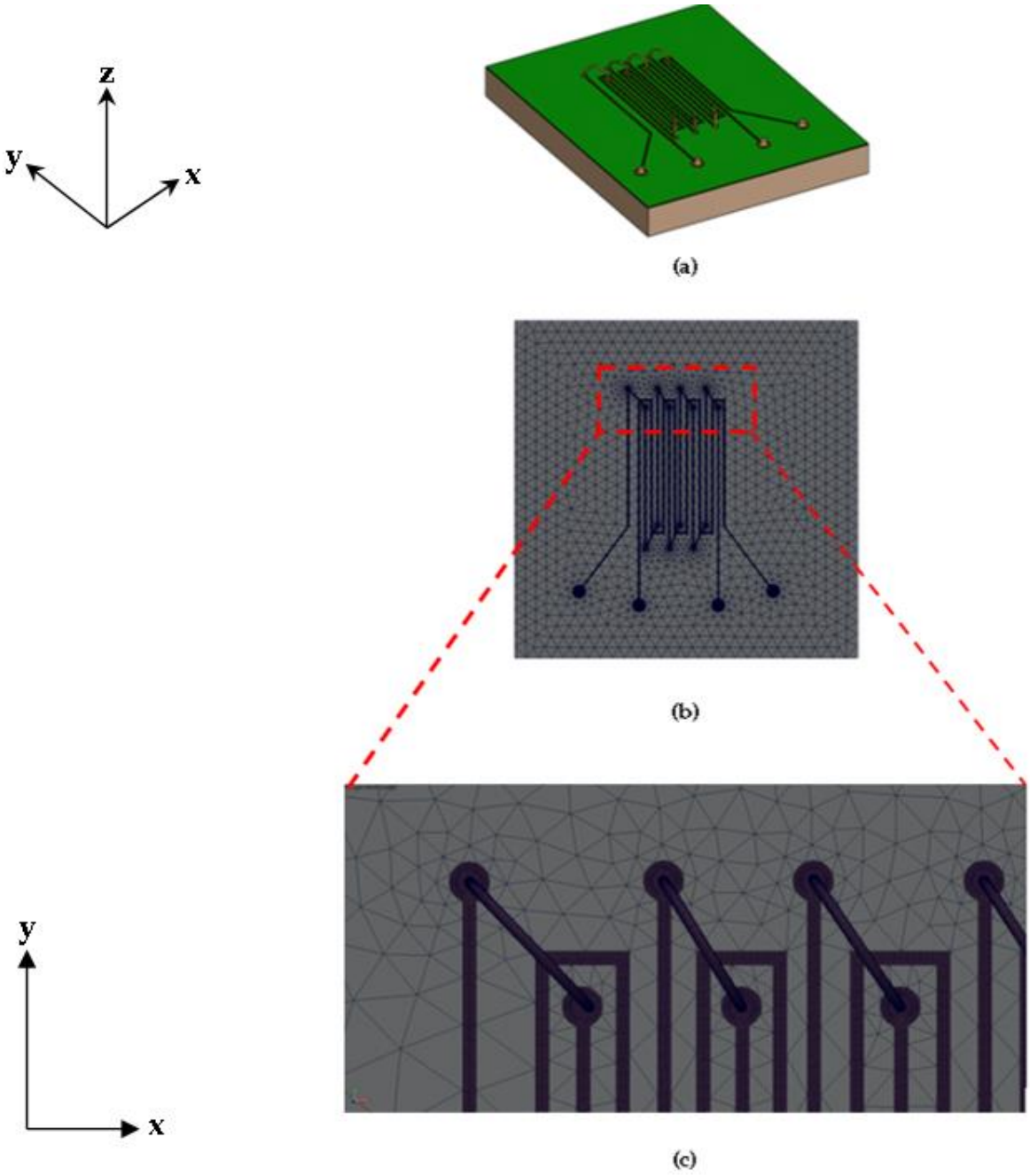

Figure 6: Computational model of the electronic chip and copper base for the heat dissipation analysis: (a) CAD model, (b) meshed model, and (c) close view of electrode meshing.

The results section discusses the results of the simulation. We've also evaluated two designs developed to enhance heat dissipation and prevent burning of the electrodes. In this regard, the wires that were used to connect each electrode pad are connected via

soldered connections and are covered with a high thermal conductance epoxy. For our initial design, we constructed a force convection setup consisting of a 3-D printed stand outfitted with a copper heat sink and central processing unit *(CPU)* fan. A series of tests were run to determine the temperature response of the electrodes to the applied current. A National Instruments cDAQ 9133 data acquisition system and thermocouple was used to obtain temperature profile data for current settings. The thermocouple was tightly connected directly atop the electrodes to measure the temperature change. The results section provides the results from this test and this setup did prove to be ineffective. We later incorporated a cooling water system into the experimental setup rig.

The cooling system consisted of a Bewinner 800L/H mini water-cooling pump and clear flexible lines to circulate water, an Aveks CPU 50mm water block to cool the chip, and a Boekel Benchtop Micro-cooler II to cool the circulating water. For later thermal experiments, a Neslab Endocal RTE-5B Heated/Refrigerated Circulating Bath was used to cool the cooling block with water as the working fluid. *Figure 7* below shows a photograph of the rig set up with the water-cooled pump and CPU water block. A CPU fan was also added in the final setup shown in *Figure 8*. A FLIR DM166 imaging multimeter was used to monitor the infrared temperature profiles and a thermocouple was used similar to the initial design to evaluate the temperature profiles.

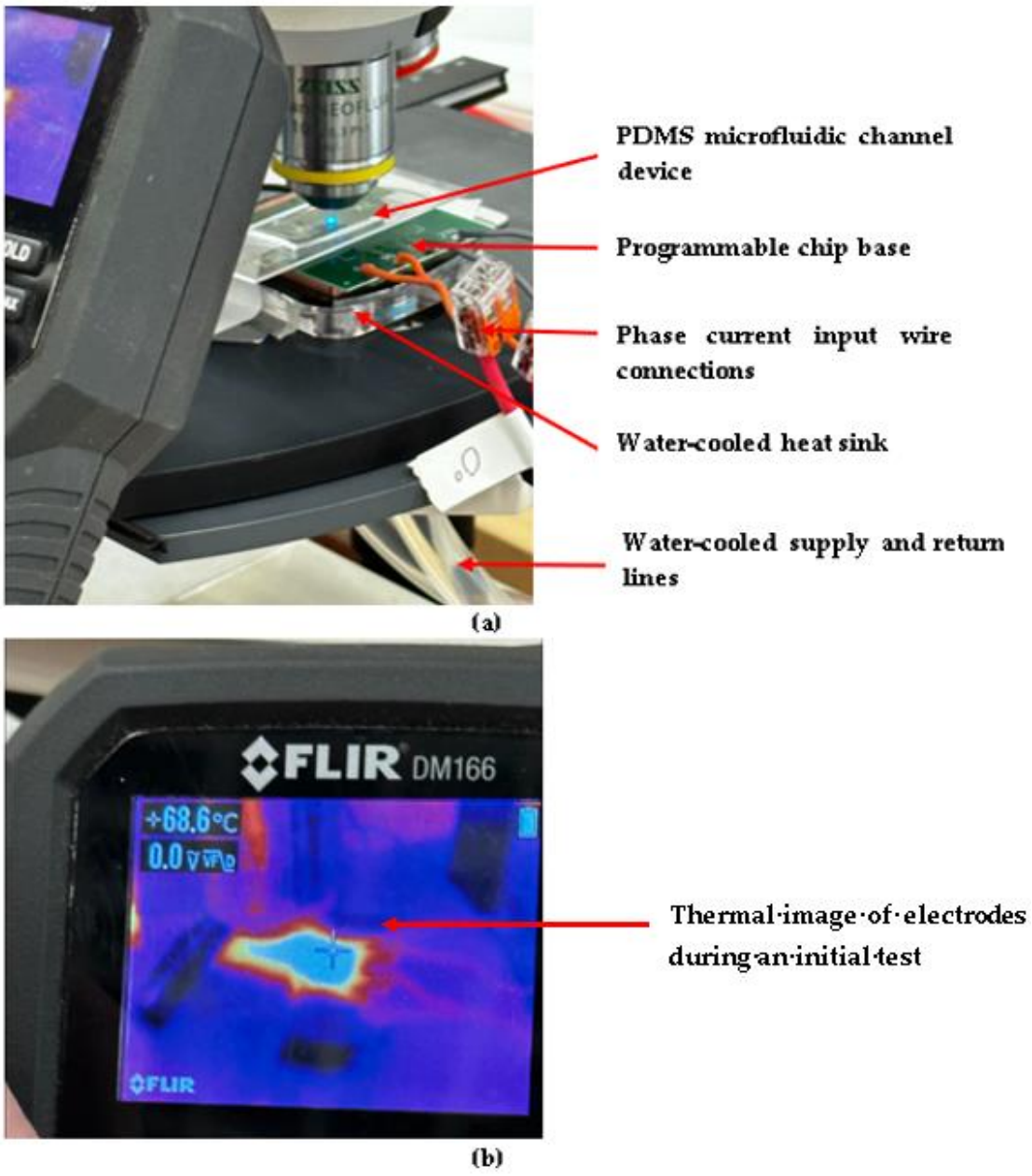

Figure 7: System rig and water-cooled heat dissipation setup: (a) full system with the ferro-microfluidic device and water block and (b) the thermal image of the electrodes with an input current.

For the water-cooled heat dissipation design system setup experiments, the mini cooler was set to a temperature setpoint of -20°C in which water circulated throughout flexible lines and the water block during the experiments. The actual cooling temperature was taken to be 0°C. The temperature was recorded periodically for 5 minutes while currents of 0.5 to

6 A are applied to the electrodes using an excitation frequency of 1 kHz. The results section discusses the results of the experiments.

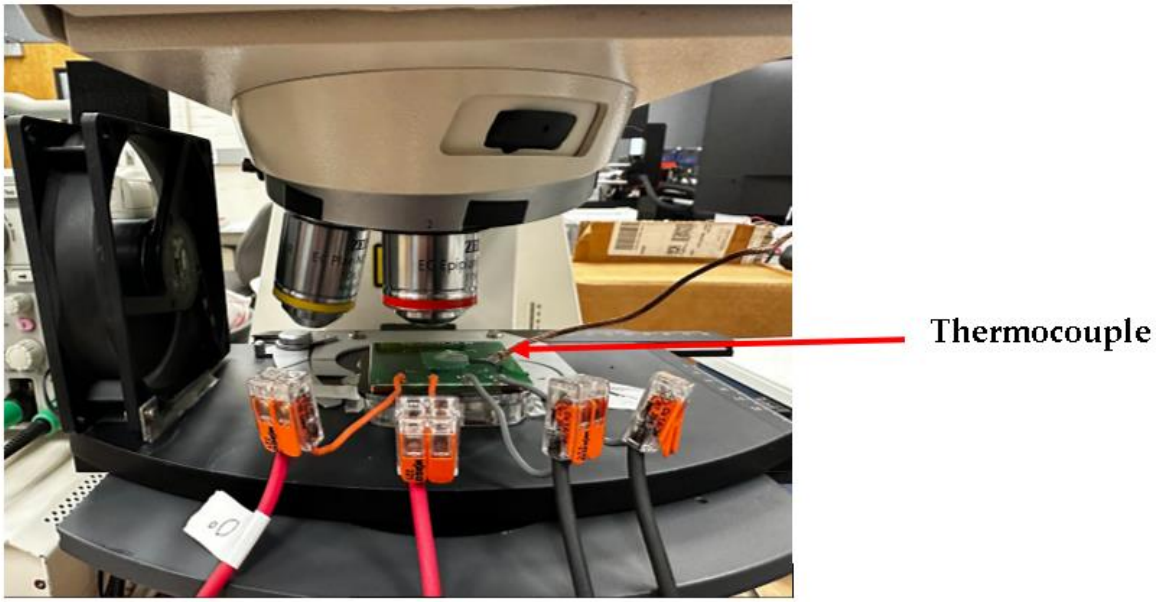

Figure 8: Thermal experiment setup.

The next section discusses the ferrofluid tailoring methodology and the channel device preparation methodology.

2.10 Ferrofluid tailoring and ferro-microfluidic Device Preparation

Tailoring the ferrofluid for this work consisted of two parts: (1) developing the magnetic cobalt ferrite microparticles and (2) suspending the cobalt ferrite microparticles and fluorescent microparticles in deionized water for the resultant aqueous ferrofluid. Section 2.10.1 describes the cobalt ferrite microparticle fabrication process. We ran two batch processes to determine a recipe for small (10-20 nm diameter) size particles.

2.10.1 Cobalt Ferrite Microparticle Tailoring Process

Ferric chloride, cobalt chloride (98 +% purity), and sodium hydroxide were used to develop the magnetic cobalt ferrite particles. 11 grams of Oleic acid of HPCL grade was used as surfactant. Double distilled, de-ionized water was used as a solvent. All the materials were reagent grade and used without further purification. The fabrication process began with mixing 25mL (0.4M) solution of iron chloride and a 25mL (0.25M) of cobalt chloride solutions in double distilled, de-ionized water. The deionized distilled water was used as a solvent to avoid the production of impurities in the final product. 3M (25ml) solution of sodium hydroxide was prepared and slowly added to the salt solution dropwise. The pH of the solution was constantly monitored as the NaOH solution was added. The reactants were constantly stirred using a magnetic stirrer until a pH level of 11-12 was reached.

The liquid precipitate was then brought to a reaction temperature of 80^{o}C and stirred for one hour. The product was then cooled to room temperature. To obtain free particles from sodium and chlorine compounds, the precipitate was then washed twice with distilled water and then with ethanol to remove the excess surfactant from the solution. To isolate the supernatant liquid, the beaker contents were then centrifuged for fifteen minutes at a given rpm (later discussed in the results) using a centrifuge. The supernatant liquid was then decanted, and then centrifuged until only thick black precipitate remained. The precipitate was then dried overnight at 450^{o}C in an oven to remove excess liquid. The acquired substance was then grinded into a fine powder. At this stage the product ($CoFe_2O_4$) contains some associated water (up to 10 wt%), which was then removed by heating at 600^{o}C for ten hours. The final product obtained was then confirmed by X-ray

diffraction to be magnetic nanoparticles of cobalt ferrite ($CoFe_2O_4$) with inverse spinel structure. Section 3 displays the X-ray diffraction and SEM images of the fabricated cobalt ferrite microparticles.

The tailoring of the ferrofluid involved suspending the cobalt ferrite microparticles in deionized water. The resulting ferrofluid had a viscosity of 1.47 cP at 20ºC. Fluorescent microparticles ranging in diameters of 1-10 μm depending on the experiments ran were added. Before introducing the ferrofluid/microsphere mixture into the microfluidic device, the channel was washed with a 1% triton-X to water solution for 10 minutes to minimize microparticle attachment to the PDMS microchannel walls. During experimental runs, the fluorescent particles were tracked and characterized with particle image velocimetry (PIV) open-source code PIVLAB as used in our previous works [77-80]. The next section presents the results of this work.

CHAPTER 3: RESULTS

The dynamics of the magnetic and non-magnetic particles travelling through the travelling wave ferro-magnetic microfluidic device are analyzed and discussed in this chapter. Two separate studies were conducted with the working fluid consisting of magnetic particles and the other with non-magnetic particles.

3.1 Simulation Results

We begin by analyzing the flow field of the ferrofluid in the microfluidic device. As mentioned previously in Chapter 2, the flow field is modelled as steady and laminar. *Figure 9* provides an illustration of the characteristic flow profile within the microchannel. *Figure 9*a shows a full view of the flow field and *Figure 9*b shows an enlarged view of the flow field from the inlet of the microchannel to electrode 3. As shown in *Figure 10b*, the flow field is organized and steady. *Figure 10* shows a plot of the velocity profile at the inlet. The velocity profile is shown to be fully developed and parabolic.

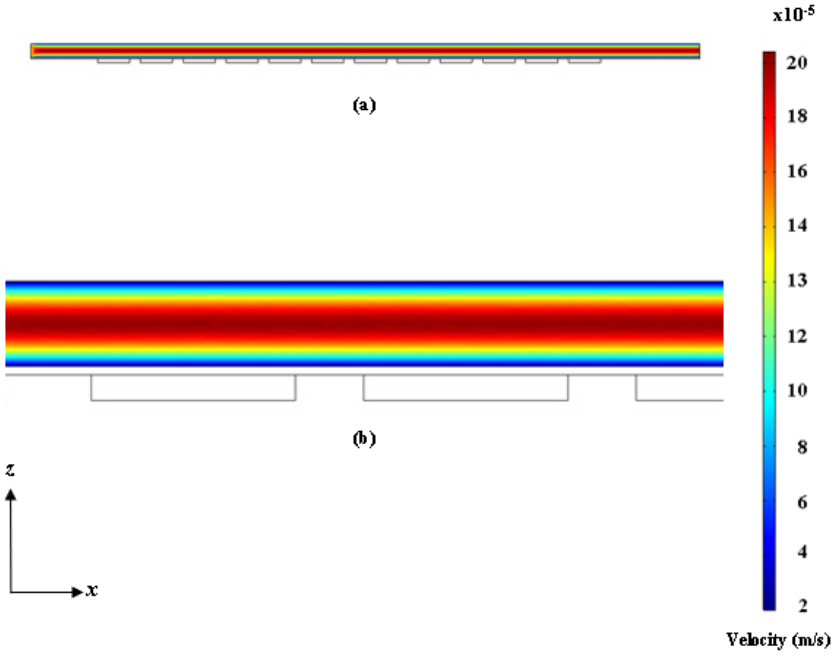

Figure 9: Velocity contour at 0.01s: (a) full view and (b) enlarged view.

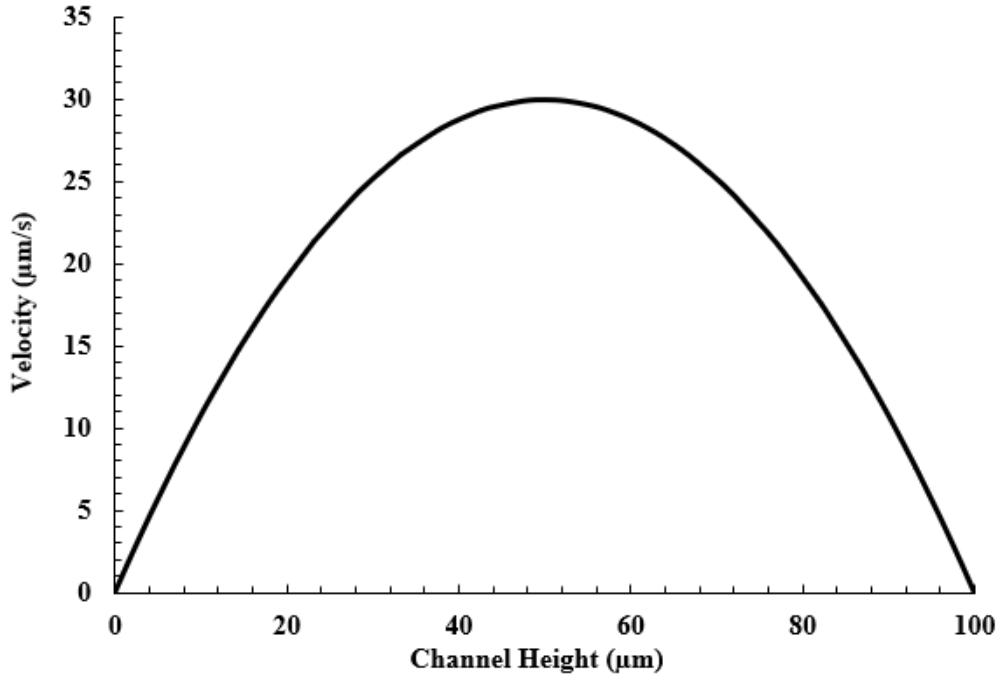

Figure 10: Velocity profile at the inlet of the microchannel.

In this work, the magnetic field is controlled by the currents travelling in each electrode. The inputs to the first and second electrodes are time-varying sinusoidal currents *(I_1=-$I_0 sin(2\pi f_0 t+\varphi_1)$ and I_2=-$I_0 sin(2\pi f_0 t+\varphi_2)$)* where I_0 is the current amplitude (7A), f_0 is the frequency *(10kHz)*, φ is the phase angle, and t is time. The current inputs are used to create the periodic magnetic landscape within the microfluidic channel. *Figure 11* shows a plot of the input current profiles to the first and second electrode.

As shown in *Figure 11*, the current waveform has a phase difference of 90 degrees, which creates a ratcheting effect for potential sorting and separation of magnetic and non-magnetic entities. The time frame of the waveform shown in *Figure 11* is 0.1ms which is relatively small compared to the reported throughput time in existing literature [81]. This time-frame is small in scale and is chosen to capture the periodicity of the waveform profile. The waveform is difficult to illustrate at larger time intervals due to the relative

(f_0> 1kHz) high frequency of 10kHz *(high oscillations)*. *Figure 12* provides contours of the magnetic field strength in the microfluidic device at different time intervals to show the rotating magnetic field. Next, we examine the particle dynamics for this work.

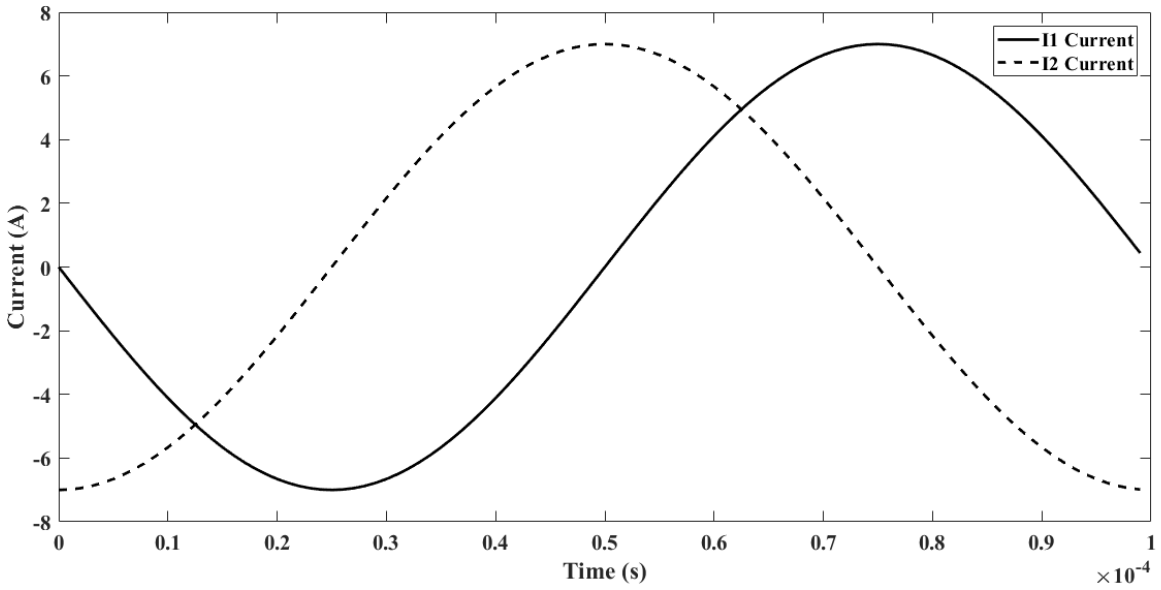

Figure 11: Input alternating currents for electrodes 1 and 2 at 10kHz and t=0.1ms.

In this work, the trajectory of the magnetic and non-magnetic particles is modelled and analyzed in the ferro-microfluidic device microchannel. We assume that the particles enter to the left of the first element and the model computes its trajectory as a function of its initial height above the conductive elements. In this work we conducted three case studies, (i) a magnetic particle trajectory analysis with the magnetic field turned off to characterize the particle dynamics without the presence of the field and (ii), a study involving the field turned on for a case with magnetic particles and (iii) a case of calculating the velocities, force, and torque on magnetic and non-magnetic particles *(RBCs and E. Coli bacteria)* with the field turned on. For the third case, the particle studies did not involve injecting particles into the microchannel, but involved using the velocity, force, and torque

equations discussed in sections 2.1 and 2.5 to theoretically calculate the velocity, force and torque given the particle properties and the magnetic field intensity.

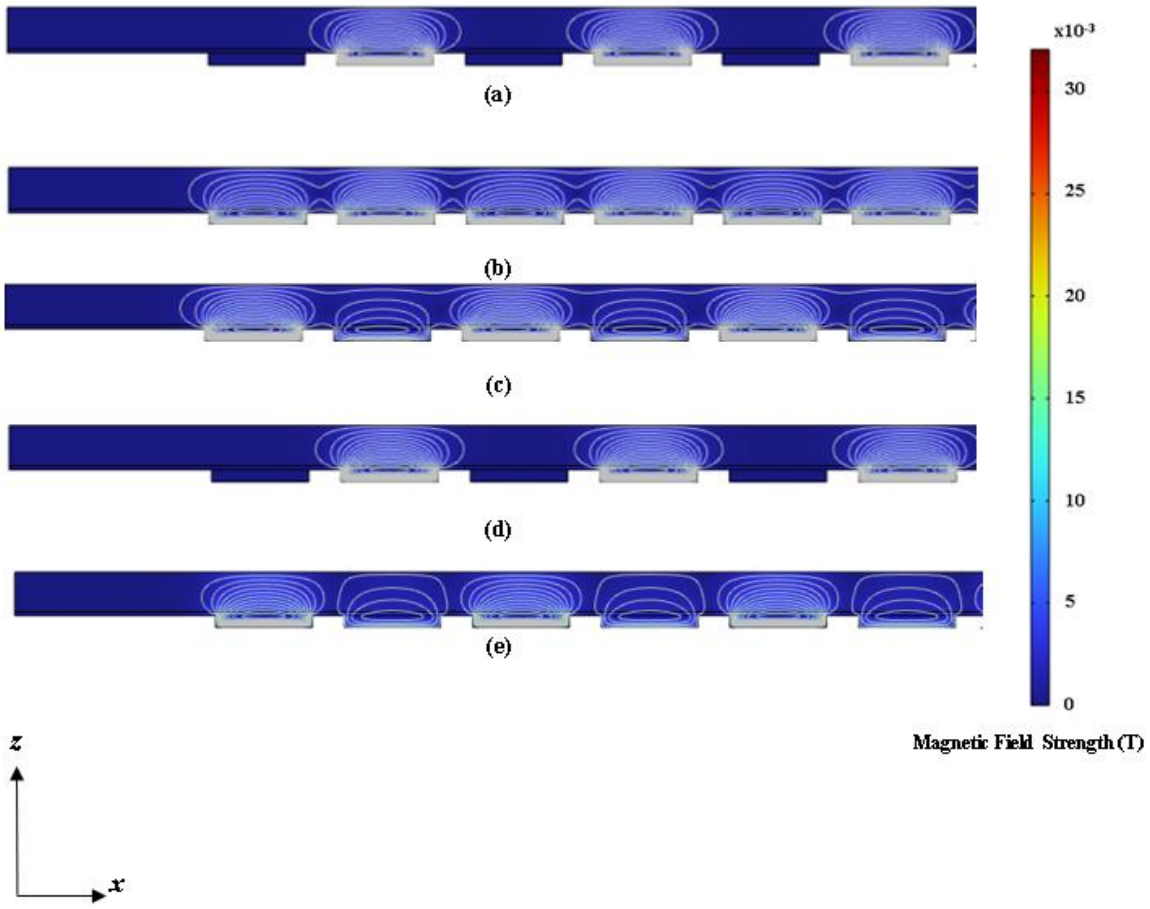

Figure 12: Magnetic field strength contours at: (a) 0s, (b) 1e-5s, (c) 2e-5s, (d) 3e-5s, and (e) 4e-5s.

For the case with the field turned off, it was observed that that the particles moved through the channel as a cluster and travelled with the flow stream. This was observed for both magnetic and non-magnetic particle studies. We did not show these results as these results are commonly expected. For the case with the magnetic field turned on, we plotted the contours of particle trajectory at discrete time intervals. *Figure 13* shows the particle trajectory profiles for a 6.1µm diameter magnetic particles injected into the fluid flow of

the microchannel with the magnetic field turned on. The particle trajectory profiles in blue are superimposed over the microchannel to illustrate the particle movement in the computational domain.

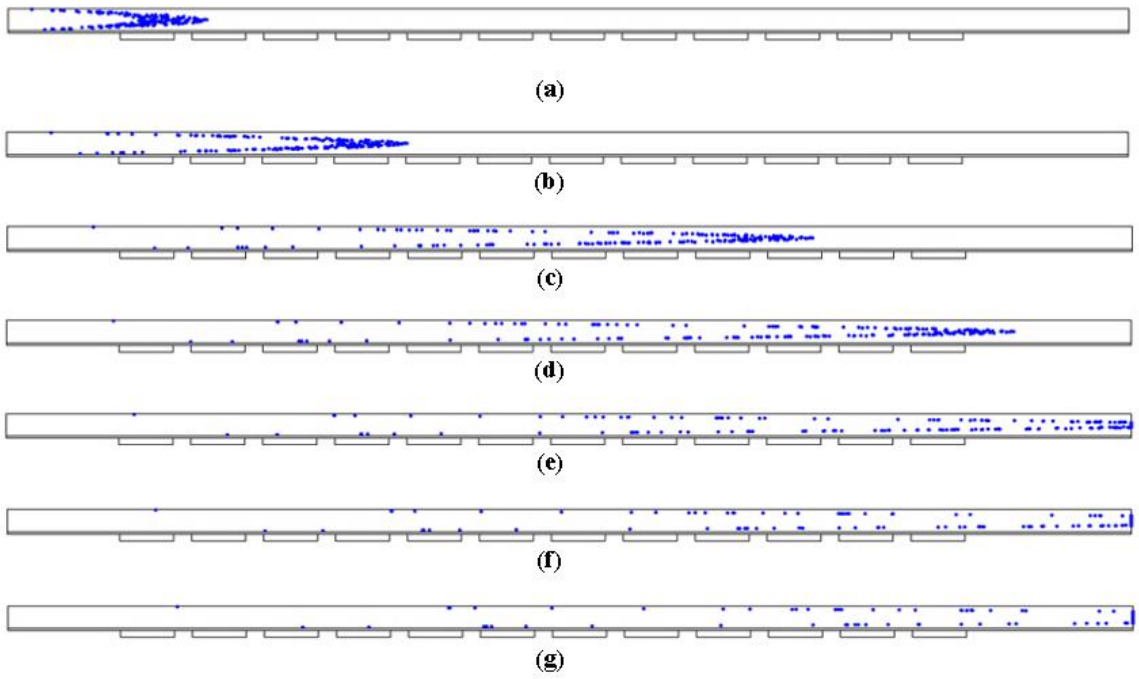

Figure 13: Magnetic microparticle tracking contours with 6.1µm diameter particles at a frequency 10kHz and at time: (a) 30s, (b) 60s, (c) 90s, (d) 120s, (e) 150s, (f) 180s, and (g) 210s.

Similar to the case without a magnetic field, the magnetic particles are injected into the micro-channel from the inlet. As shown in *Figure 13a,* the particles enter as a cluster in which the particles appear to be attracted closer to the second element which has a high magnetic field gradient. As time progressed the particles tended to break up and are pushed towards the ceiling and base of the microchannel as shown in *Figure 13 (b, c, d, e, f, and g).* This can be attributed to the y-direction dominating force due to the non-uniform magnetic field. This dominating force seems to be present from elements 1 to 12 that pushes the magnetic particles toward the ceiling and base of the microchannel. This trend

continues downstream of the channel. It appears that the magnetic field is creating an alternating force *(periodic landscape)* profile which is expected due to the phase difference between the electrodes. It also appears that the magnetic field is having a significant effect on the particles as they move through the channel. The capture efficiency calculated within the 210 s flow time range is 80%.

For this work, we also attempted to run a simulation on injecting both magnetic and non-magnetic particles into the flow simultaneously to characterize the particle dynamics in the presence of the magnetic field. The outcome was the simulation was too computationally expensive and would freeze and become unresponsive. Similarly, it was also computationally expensive to run large frequency studies for singly particle studies. The simulation would run out of memory. As a result, we modelled the magnetic and non-magnetic particle studies separately at a single frequency of 10kHz. Since the foundation of this work is built on manipulating and separating non-magnetic particles using the magnetic void effect, we calculated the velocity, force and torque on a single magnetic particle, RBC, and E.Coli particle separately.

To investigate the influence of diameter on particle motion, we calculated the particle velocities for a range of diameters. *Figure 14* shows a plot of the magnetic particle velocity at a frequency of 10 kHz and for a range of particle diameters ranging from 1.1µm to 6.1µm. *Figure 15* confirms the size dependence of the particle motion at a given frequency and any location along the length of the microchannel. We also observe that larger particles have higher velocities at any point. At a frequency of 10 kHz, particle velocities cross zero at the electrode spacings, indicating that particles eventually stop when they reach the inter-electrode spacing.

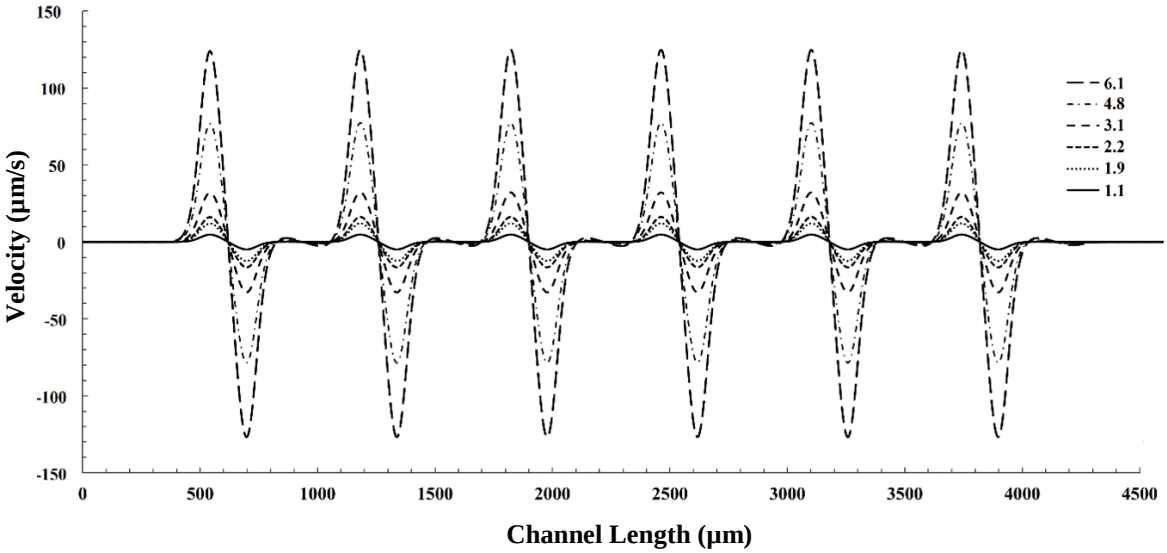

Figure 14: Magnetic particle velocities for varying particle diameter at a frequency of 10 kHz.

From the previous magnetic force derivation, we found that the magnetic force is proportional to the particle volume (r^3). After considering the fluid drag force described in Section 2, the resulting velocity due to the magnetic force is proportional to the radius.

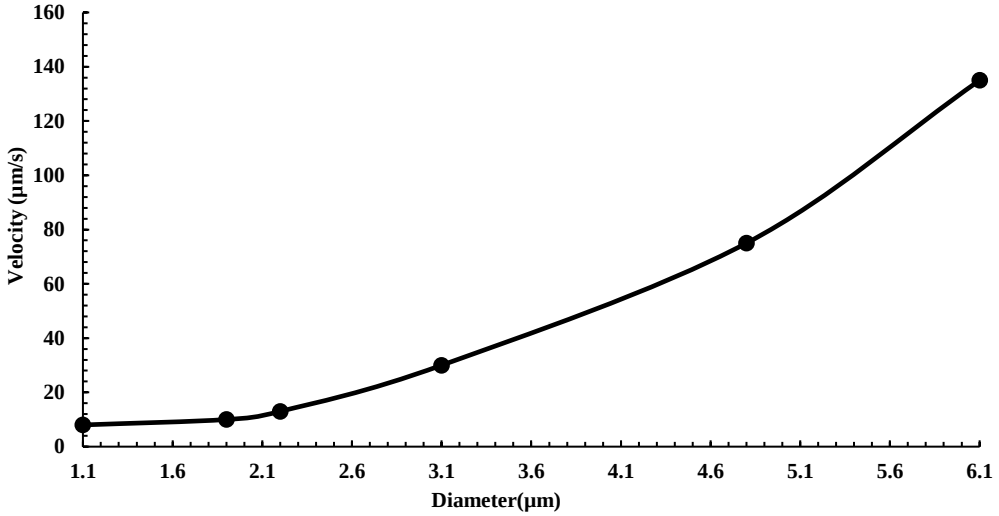

Figure 15: Maximum magnetic particle velocity for varying particle diameter at 10kHz.

Similarly, in the high frequency regime, we assume that the magnetic torque dictates the particle motion, and the magnetic force is turned off. *Figure 15* shows the

relationship of the radius to with the magnetic particle velocity at a frequency of 10kHz confirming the theory.

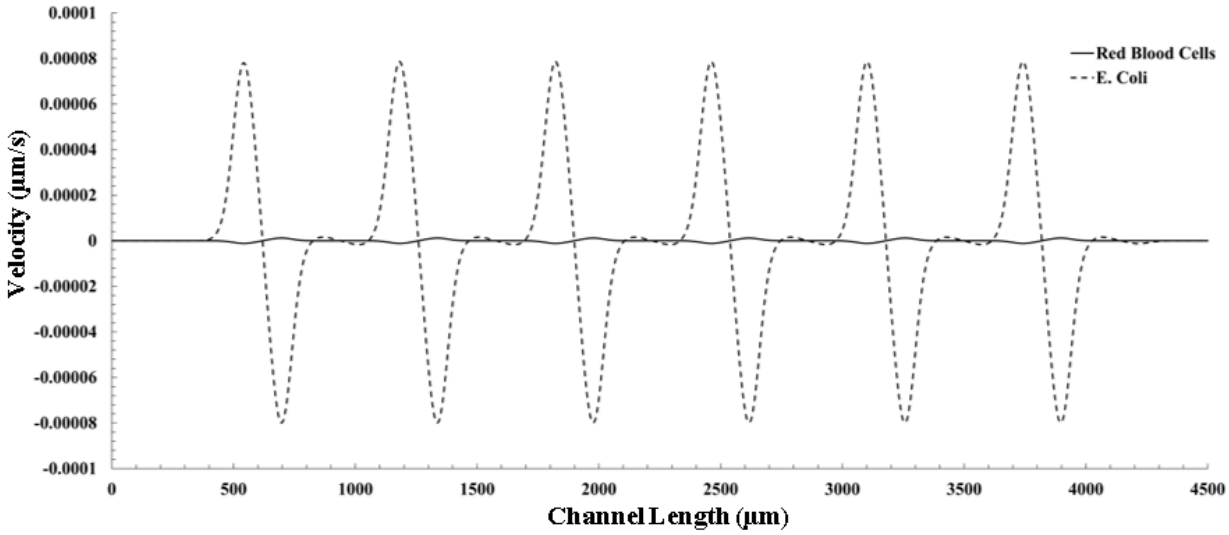

Figure 16: Particle velocities for RBCs and E. Coli.

Similar to the magnetic particle studies, we conducted a particle velocity analysis on the non-magnetic particles *(RBCs and E.Coli)* for a frequency of 10 kHz. *Figure 16* shows a plot of the particle velocity as function of microchannel length. The particle velocities for both RBCs and E. Coli are significantly lower as compared to the magnetic particles. The maximum particle velocity observed is six orders of magnitude slower as compared to the magnetic particles. This provides rationalization that RBCs and E.Coli would lag, whereas the magnetic field would push the magnetic particles out of the channel from samples. Similar to magnetic particle studies, the RBCs and E. Coli are observed to be trapped in the electrode spacings.

The magnetic field appears to be at its maximum directly above the electrodes and the particle velocity is highest. Between the two electrodes, the magnetic field decreases, resulting in slower particle motion. Particles that speed up above the electrodes slow down as they approach the spacing between electrodes. An additional phenomenon observed is

that RBCs have a different phase shift trend than the E. Coli. This is believed to be attributed to the magnetic polarity of the cells due to the negative susceptibility.

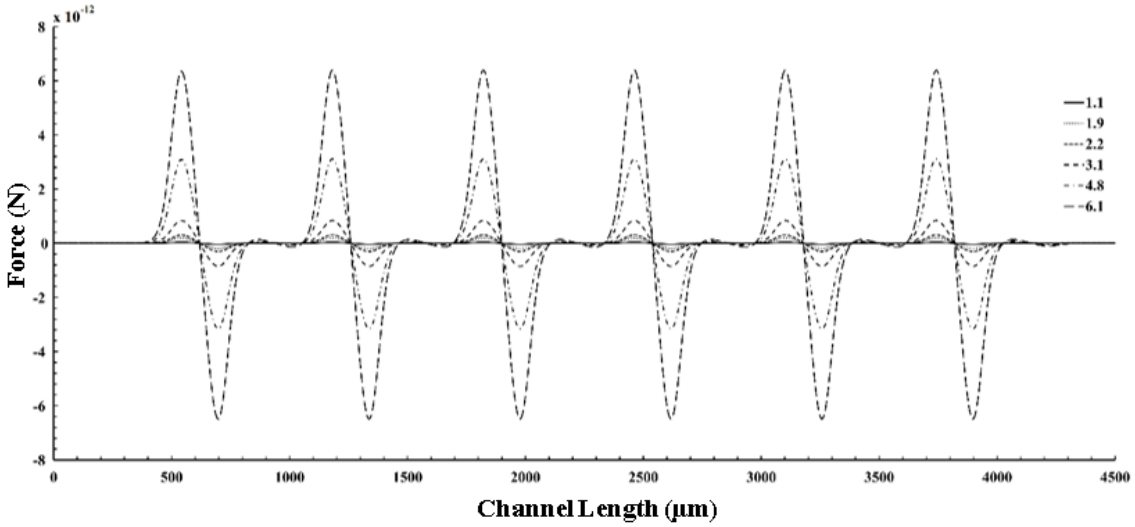

Figure 17: Magnetic force magnitude for varying particle diameter at a frequency of 10 kHz.

In further analysis, we look at the direct correlation between magnetic force and resulting particle torque for both magnetic particles. The resulting magnetic force on magnetic particles for varying particle diameter is shown in *Figure 17*. At a frequency of 10kHz, the force dominates, pushing the non-magnetic microparticles up to the channel ceiling and into the space between the electrodes. We assume that in the very low frequency regime, the magnetic torque is turned off and magnetic force dominates the particle motion. *Figure 18* provides a plot of the magnetic particle torque as a function of microchannel length. Similar to the velocity and force plots, the highest torque observed is above the electrodes while the torque magnitude diminishes between the electrodes. It is also observed that the highest torque and force is experienced for larger particle diameters. Overall, the torque and magnetic force plot show trends that suggest that magnetic particles would have sufficient torque and force to separate magnetic particles

from non-magnetic entities such as RBCs and E.Coli. Further work should be done to assess magnetic susceptibility of different materials and cells to analyze separation efficiency.

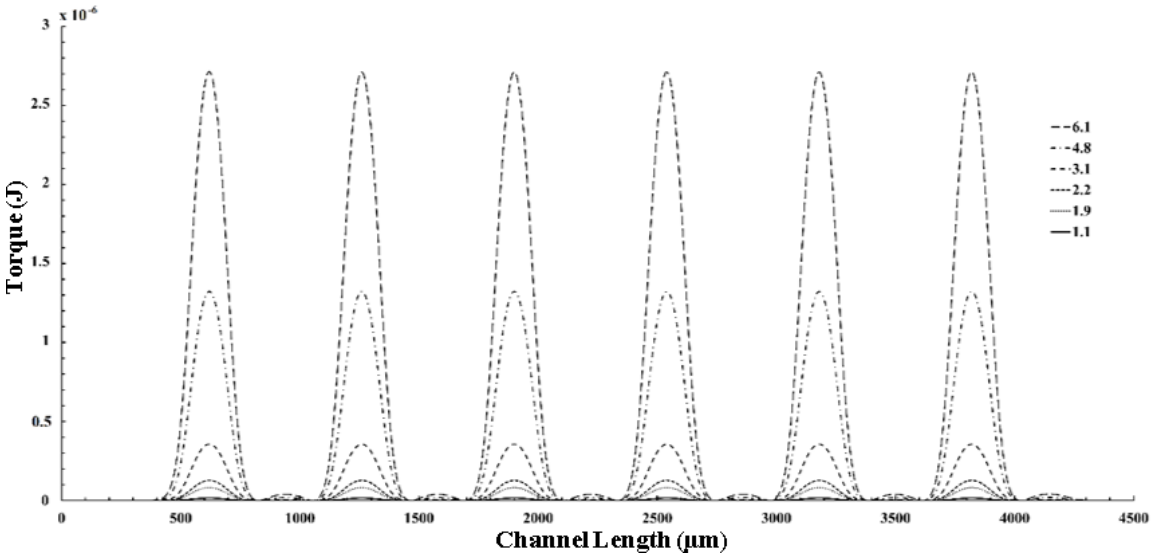

Figure 18: Magnetic torque magnitude for varying particle diameter (1.1µm to 6.1 µm) at a frequency of 10 kHz.

3.2 Experimental Results

This section of the paper provides a discussion on the results obtained from the heat dissipation computational analysis, results from the cobalt ferrite nanoparticle and ferrofluid tailoring procedure, and the initial particle dynamics analysis for the ferro-microfluidic device characterization. We begin with the results from the heat dissipation computational analysis.

3.2.1 Heat Dissipation System Design Results

In this work, we conducted a simple initial computational thermal heat load analysis using Solidworks™ Thermal Simulation package v.22 to provide a baseline perspective of the temperature range for the low and high heat loads. For heat conduction computational

analyses, Solidworks Thermal Simulation package solves the Fourier Heat Conduction equation below in Equation 1 in a finite element form:

$$\rho c_p \frac{\partial T}{\partial t} = k\left(\frac{\partial^2 T}{\partial x^2} + \frac{\partial^2 T}{\partial y^2} + \frac{\partial^2 T}{\partial z^2}\right) \quad \textbf{(1)}$$

where ρ is the material density, c_p is the material specific heat, k is the thermal conductivity and x, y, and z are the three-dimensional spatial directions of heat transfer.

For this analysis, we conducted a low and high thermal power load assessment based on the minimum and maximum current settings of 1 A and 7 A. Both the low and high load simulations were transient and were ran for a total time of 3 s with 0.01 s timesteps. The simulation took a total time of 1 hour to run the simulations with the default thermal finite element (FEM) and transient solver. *Figure 19* below shows a temperature and thermal iso-contour for the low load simulation for a total time of 3 s.

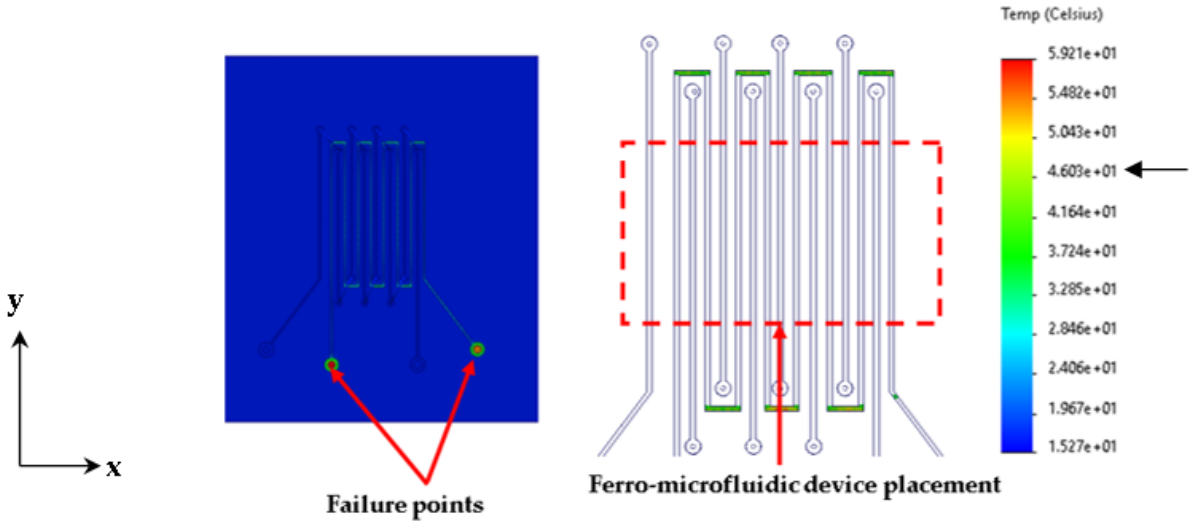

Figure 19: Thermal simulations at 2 W for 3 s: (a) thermal contour and (b) thermal iso-contours. The dashed lines in the iso-contour represent the area where the ferro-microfluidic device will sit. The black arrow on the color scale represents the temperature threshold for cell damage.

As shown in *Figure 19*, the temperature distribution in the electrodes is uneven from the input pads throughout the two electrode profiles *(bonded electrodes)* to the output pads. An interesting phenomenon observed is that the highest load point occurs at the wiring input and output pads. Several simulations were conducted with varying mesh size, and we noticed the same trends in heating regardless of the mesh sizing and type. This phenomenon may be due to the fact that a heat conductive object with a wider surface area has more surface area to act as a conduit for conducting and transferring heat [82, 83]. In this case, the rate of heat transfer is directly proportional to the surface area through which the heat is being conducted. Additionally, when comparing the pads to the actual electrodes, the pads will indeed conduct more heat than the electrodes during current inputs.

For the low heat load analysis, the highest temperature observed at 3 s was 59.21 ^{o}C. The temperature is well above the temperature of cell damage. This temperature remains constant for the duration of the current input, indicating that the simulation becomes steady state at 3s. The thermal iso-contour shown in *Figure 19b* also shows that the highest temperature in the electrodes is observed in the areas where the electrodes make sharp turns. This phenomenon is due to conductivity resistance. Sharp corners influence heat transfer similar to sharp bends in fluid pipes create energy losses and flow disturbances. We took this into consideration for the development of the chip base. For the high heat load case *(7 A)*, we noticed that the temperature climbs instantly at 0.1s and goes to steady state at 0.2 s. *Figure 20* below shows a temperature probe profile plot at a nodal point in the first electrode. From *Figure 20* it is observed that without a heat sink and proper cooling, the electrodes will degrade fast under high heat loads.

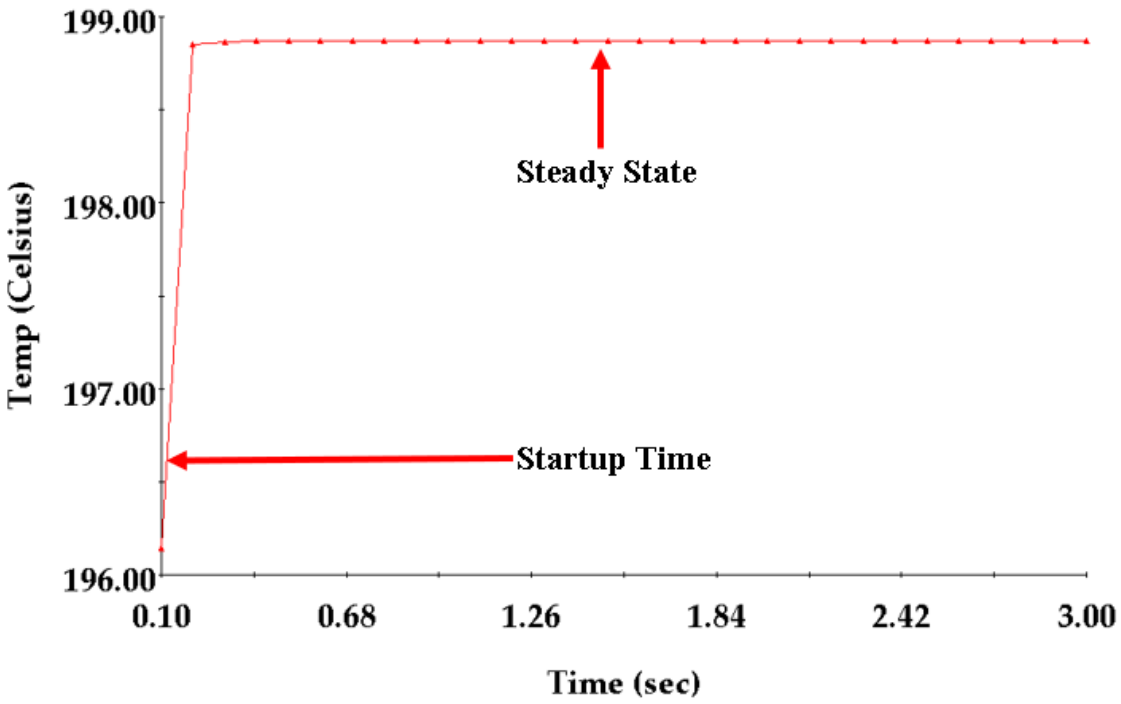

Figure 20: Temperature vs. time probe profile plot at the first electrode for 7 A without a heat sink and proper cooling.

After running the computational simulations, we conducted three forms of experimental thermal analysis studies. As mentioned previously, the electronic chip is designed and expected to operate with current levels of 1-7 A and covering a large frequency spectrum *(10 Hz-100 kHz)*. We first conducted a thermal heating analysis where we experimentally measured the temperature of the electronic chip base as a function of time, increasing amperage, and at a maximum frequency of 1 kHz. This analysis consisted of powering the electrodes and recording the temperature of the electrodes without a heat sink. *Figure 21* shows a plot of the temperature profile at each current setting at 1 kHz.

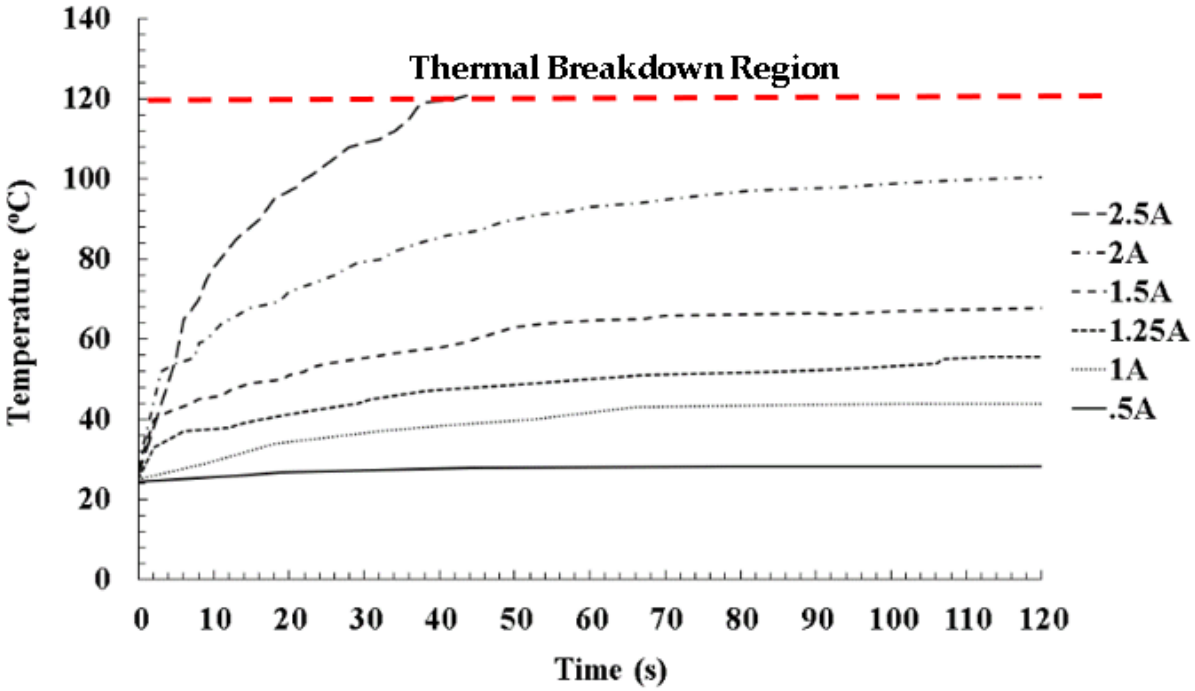

Figure 21: Temperature vs. time profile of the electrodes at various current settings. The dashed line represents the thermal breakdown region for the copper electrodes.

As shown in *Figure 21*, at low current settings *(0.5-1.5 A)*, the chip can survive the current loads without a heat sink involved. The need for a heat sink becomes evident at 2.5A where the chip experiences thermal breakdown *(120°C)* at 2.5A around 40s. For our initial design, we constructed a force convection setup consisting of a 3-D printed stand outfitted with a copper heat sink and central processing unit *(CPU)* fan. During experimental testing, it was concluded that the forced convection setup was not sufficient to continuously remove heat. In this setup, we were able to reach 3-4 A for a total time of 10s before we exceeded 130°C and the chip was damaged. *Figure 22* below shows the result of a damaged chip after 10s of heating with the forces convection setup.

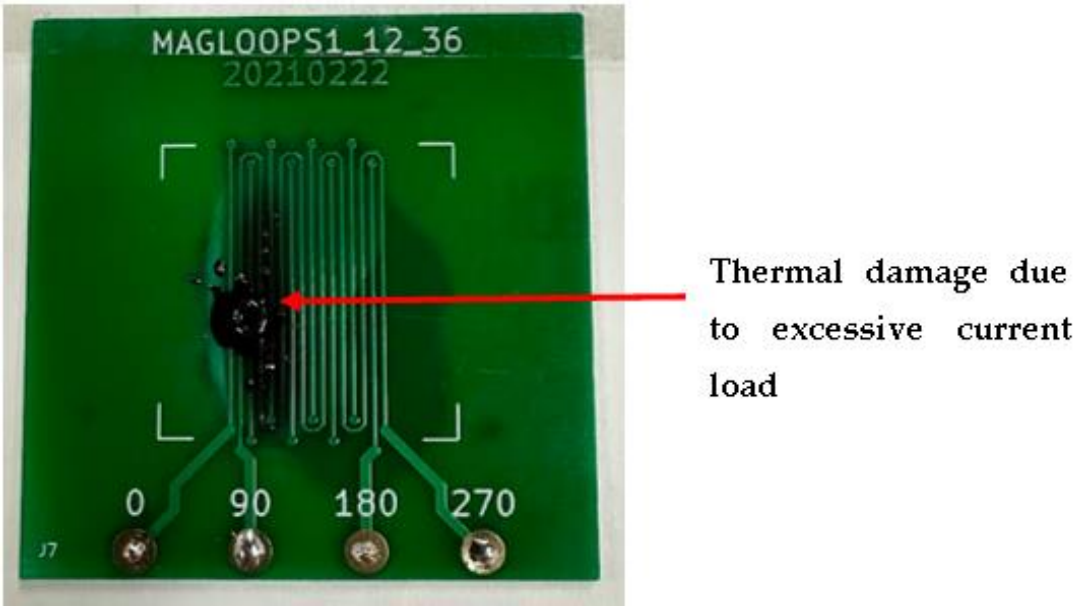

Figure 22: Photograph of the damaged chip during the forced convection setup.

At these current levels, heating of the programmable chip and microfluidic device and eventual thermal change to the electrodes is inevitable. As a result, we incorporated a cooling block and cooling water system to the experimental set up to maintain the electrodes as close to room temperature as possible during experimental runs. To test the effectiveness of the cooling water system, we performed a series of tests to determine the temperature response of the electrodes to the applied current, while the cooling water is active. A thermocouple is tightly connected directly atop a glass slide and place on the electrodes to measure the temperature change for incremental currents.

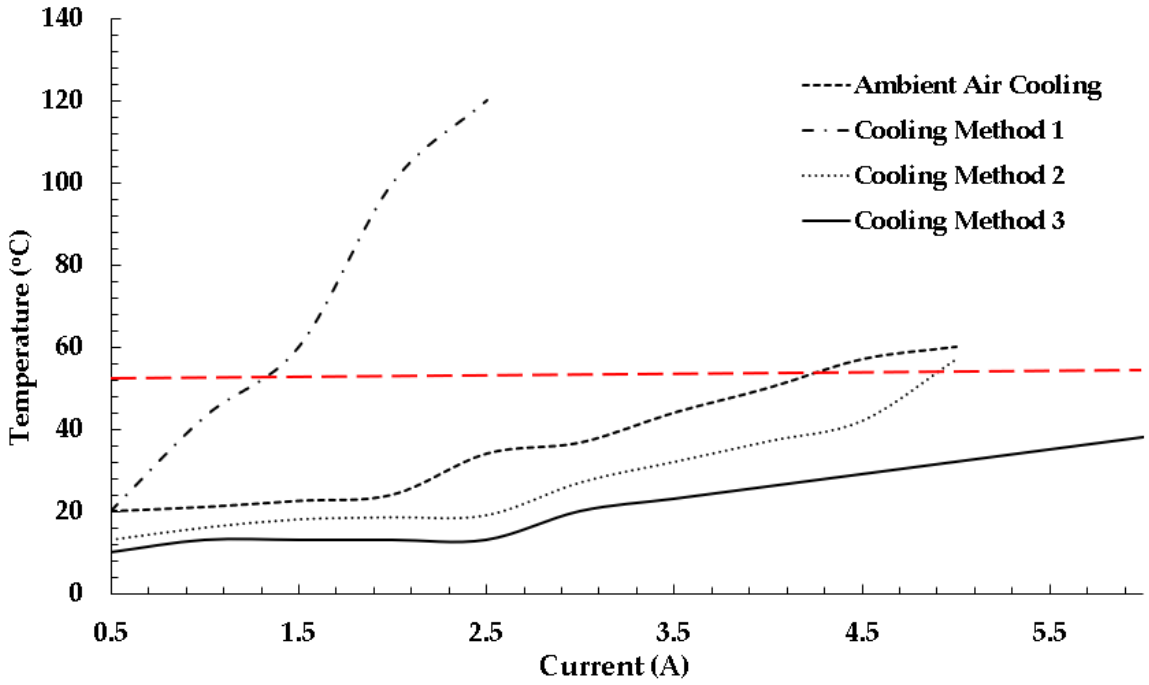

Figure 23: Averaged steady state temperature for each current setting. Ambient air cooling is without a cooling device, Cooling method 1 is using a micro-cooler setup with water at 0°C, cooling method 2 is using a Neslab bath circulator setup with the temperature set to 0°C.

We ran three types of cooling tests. For cooling water, with a temperature setpoint of -20°C circulates during the course of the experiment. The temperature is recorded periodically for 3 minutes while currents of 2, 3, 4, 5, and 6 A are applied to the electrodes using an excitation frequency of 1 kHz. We observed that the temperature reaches a steady state value after around 30 seconds. More importantly, for currents less than 5 A, the cooling water keeps the electrode chip temperature at room temperature to prevent the electrodes from burning or for the heat to affect the ferrofluid and sample being tested. The next section discusses the ferrofluid tailoring results.

3.3 Cobalt Ferrite Particle Synthesizing and Ferrofluid Tailoring Results

In this work, we tailored a cobalt ferrite-based aqueous ferrofluid using a method described in detail in section 3.3. Cobalt-ferrite possesses a high magnetic anisotropy energy density (between 1.8×10^5 and 3.0×10^5 J/m^3 for bulk material and up to 3.15×10^6 J/m^3 for nanoparticles [84]). We conducted two experimental runs for tailoring cobalt ferrite particles. *Figure 24* show the TEM images of the first batch of $CoFe_2O_4$ nanoparticles calcined at 600^{o}C for more than 10 hours (with an average crystallite size of about 48.53 nm as determined by XRD).

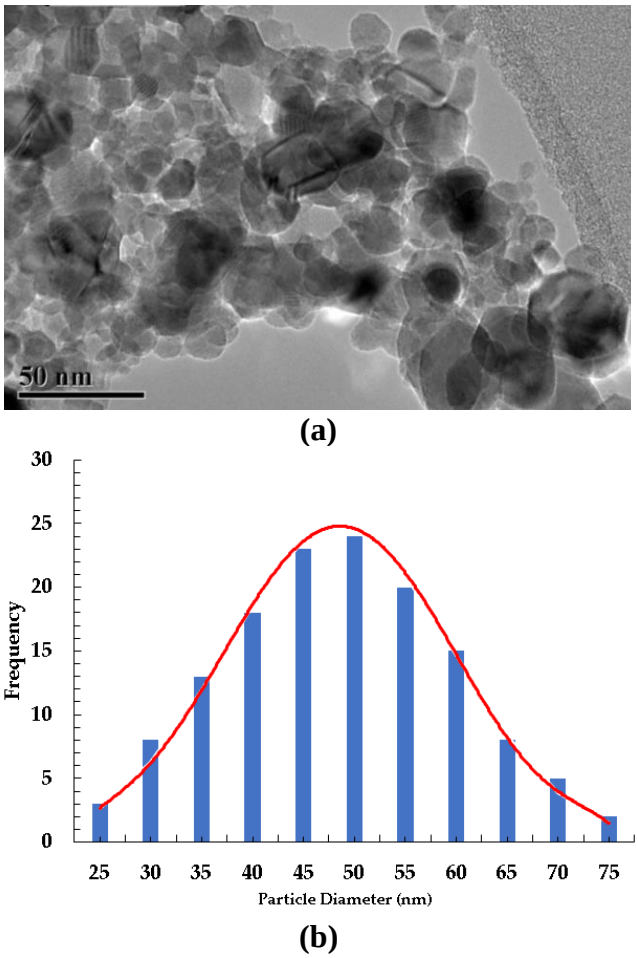

Figure 24: Individual particle sizes as extracted from TEM images for the first batch: (a) TEM image of the particles and (b) the log-normal distribution with a 48.53 nm average particle diameter.

We also performed x-ray diffraction studies on the synthesized cobalt ferrite microparticles. A plot of the x-ray diffraction results is shown in *Figure 25*. The x-diffraction pattern of the calcined powder synthesized shows that the final product is $CoFe_2O_4$ with the expected inverse spinel structure. No other phase/impurity was detected during the analysis. The size of the particles was determined by the Scherrer formula using the first two strongest peaks. The average sizes of the particles calcined at 600^oC were found to be approximately 50±2nm.

The size distribution of these nanoparticles observed from the TEM images is shown in *Figure 24b*. The distribution appears to be symmetric *(Gaussian)* about 48.53 nm, with a particle diameter range of 25-70 nm for this specimen which is preferred. The maximum number lies between 45 and 55 nm, peaking at 48.53nm, in good agreement with XRD crystallite size. Most of the particles appear spherical in shape however some elongated particles were also observed as shown in the TEM image. Some moderately agglomerated particles as well as separated particles are present in the images.

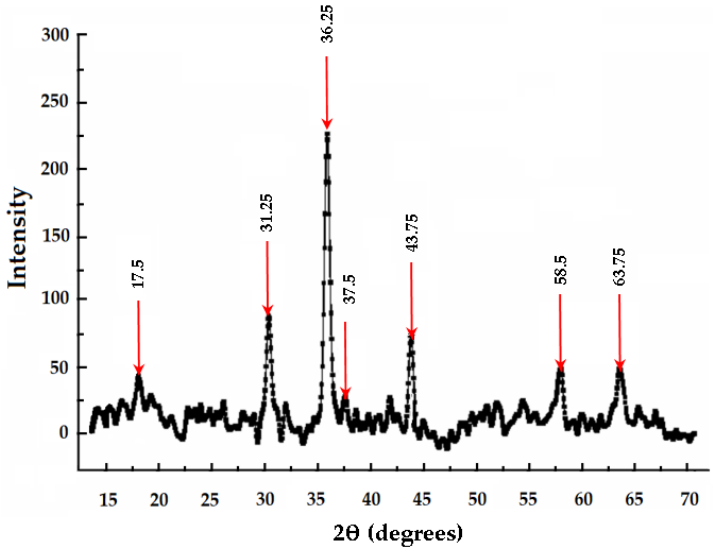

Figure 25: X-ray diffraction results for the 1st sample of cobalt ferrite particle tailoring.

We later observed for the second batch, that increasing the rate NaOH and increasing the rpm above 3000 rpm led to smaller particle diameter sizes. In the second batch we were able to achieve an average particle diameter of 17.9nm. ***Figure 26*** shows the histogram generated for the second batch.

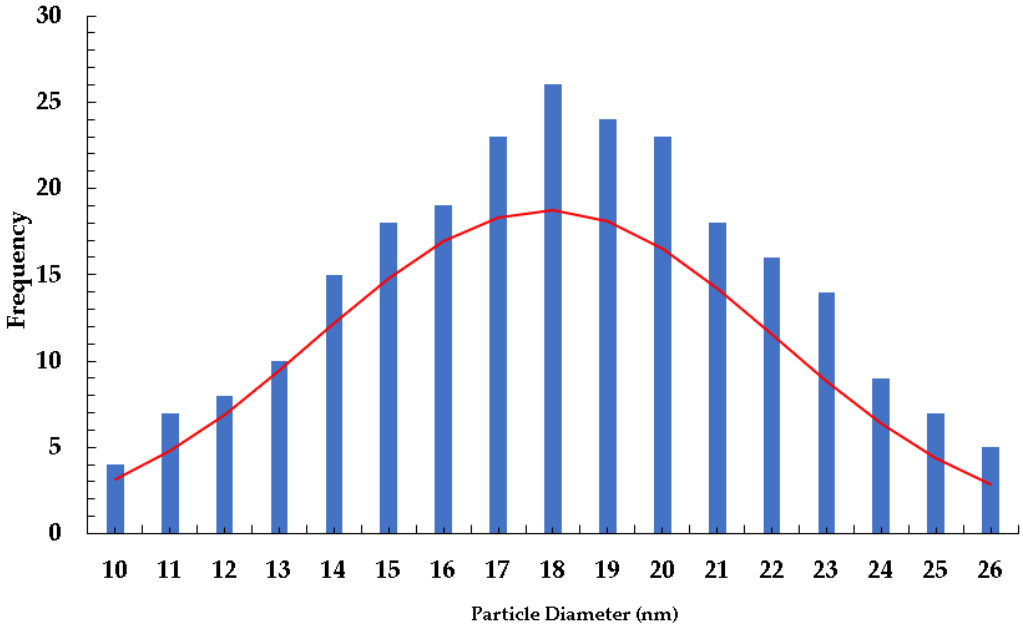

Figure 26: Histogram of particle sizes for the third batch with an average diameter of 17.9 nm.

In this data set, the average diameter and standard deviation is 17.9 nm and 4.17. This is ideal as compared the first batch as ferrofluids incorporating cobalt ferrite particles relax primarily by particle rotation *(Brownian motion)* for nanoparticles 5-20 nm in diameter. Prior to tailoring the cobalt ferrite and non-magnetic fluorescent microparticle ferrofluid, we suspended the tailored cobalt ferrite particles in deionized water, sonicated the mixture for 10 minutes and injected a small sample of the mixture in a single microchannel device as shown in *Figure 27*. As shown in *Figure 27*, the cobalt ferrite particles are randomly suspended in the microchannel with some particle aggregations observed *(numbered regions)*. The blurry particles represent particles that are closer to the bottom of the channel. To minimize particle aggregations in the ferrofluid mixture, we sonicated succeeding ferrofluid mixtures for 20 minutes and noticed no further aggregations.

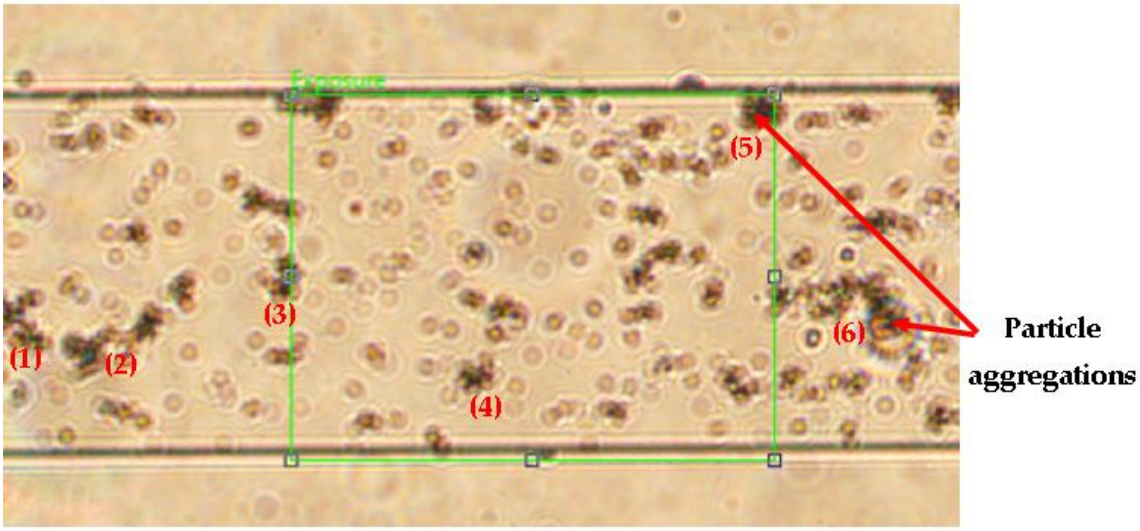

Figure 27: Microscope image of cobalt ferrite particles suspended in water in a PDMS single microchannel device. The numbered regions show the locations for the largest particle aggregations.

For the non-magnetic microparticle manipulation experiments, we prepared a water-based ferrofluid comprised of cobalt ferrite microparticles, which were synthesized using

the method described in section 2.3. The viscosity of this ferrofluid was determined to be 1.75 cP at 20ºC. Our initial experiments involved characterizing the behavior of 1 µm diameter non-magnetic particles. ***Figure 28*** below shows a scanning electron microscopy *(SEM)* image of the 1 µm diameter particles. The next section presents the particle dynamic results.

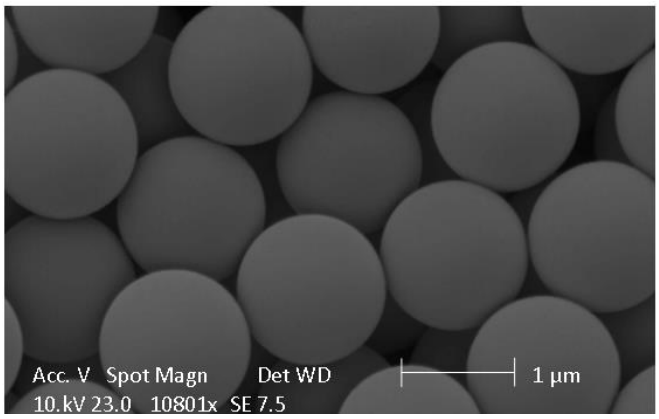

Figure 28: SEM images of 1 µm fluorescent microspheres. Microspheres are prepared to have a uniform size distribution and minimum surface charges.

3.4 Particle Dynamic Characterization Studies

This section of the paper discusses the non-magnetic microparticle dynamic study results using image cross-correlation techniques. Prior works have incorporated simple algorithms for tracking particles using recursive particle tracking techniques. This work is unique in that we can use cross-correlation analysis to determine particle trajectories, particle/fluid velocities, streamlining of flow, and vorticity *(fluid/particle)* spin. To begin the analysis, an ensemble correlation of sparsely seeded steady flow images are obtained from the videos taken during experimental runs and analyzed via cross-correlation.

The resulting correlation matrices are averaged before a peak searching algorithm is used, resulting in sufficient signal-to-noise ratio and high vector resolution for the low particles density images *(low concentration compared to PIV analyses)*. We performed the

ensemble correlation in PIVlab open-source software which features all the advanced correlation techniques of the regular correlation. This ensemble correlation involved a multiple pass, window deformation, suppression of autocorrelation, and background subtraction method for pre-processing particle/fluid flow images. To characterize the ferro-microfluidic device using fluorescent polystyrene microspheres, we conducted a series of experiments using Thermofisher Scientific; fluorescent monodisperse with diameters ranging from 1 to 10 μm. *Figure 29* below shows the result processing a frame image using this method for 4 μm diameter particles. For this example, the 4 μm diameter particles are used athey are easy to visualize and track in sparsely seeded images. This study was done with an amperage of 4 A and a frequency of 10 Hz.

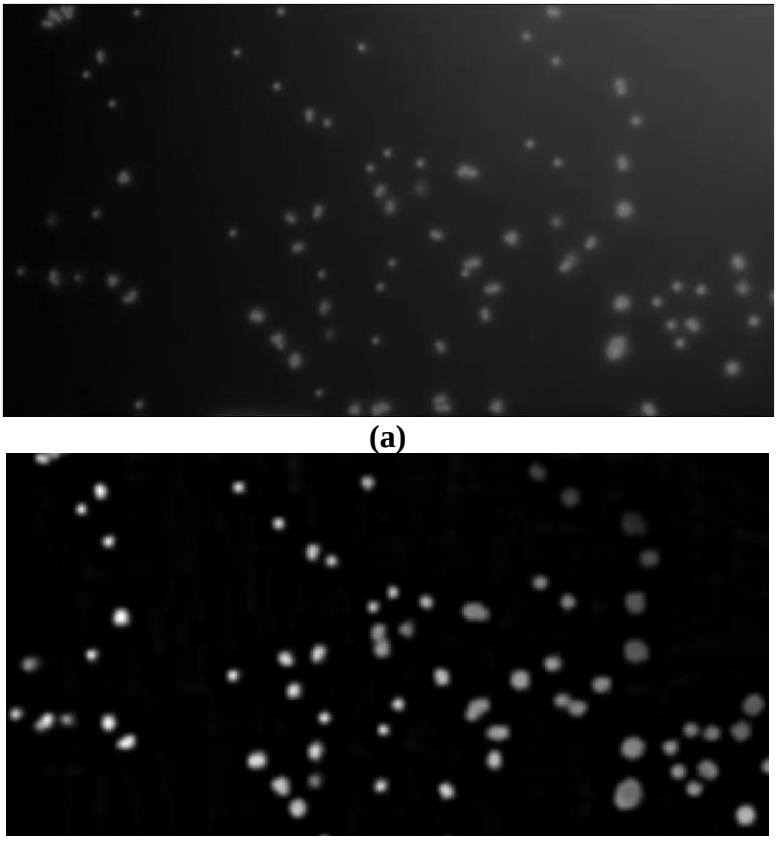

(a)

(b)

Figure 29: Particle image processing result in PIVlab for 4μm diameter particles.

For this study, the image post-processing consisted of calibrating the image with a reference line placed between the microchannel walls. The reference line was calibrated to the same length of the microchannel from wall to wall. This allowed the software to have a reference distance line for estimating velocity. After pre-processing the image, the images were resolved to velocity flow image contours. *Figure 30* below shows an example of the processing methodology and the results using 4 μm diameter particles at 4 A and 10 Hz for the small spacing electrodes. As shown in *Figure 30b*, the velocity contour demonstrate that the low flow regime exists at the electrodes and increases at the electrode spacing gap. This is because the electrodes create the force necessary for the particles to be pushed to the top of the channel, gain momentum, and translate across the channel at a given frequency and amperage.

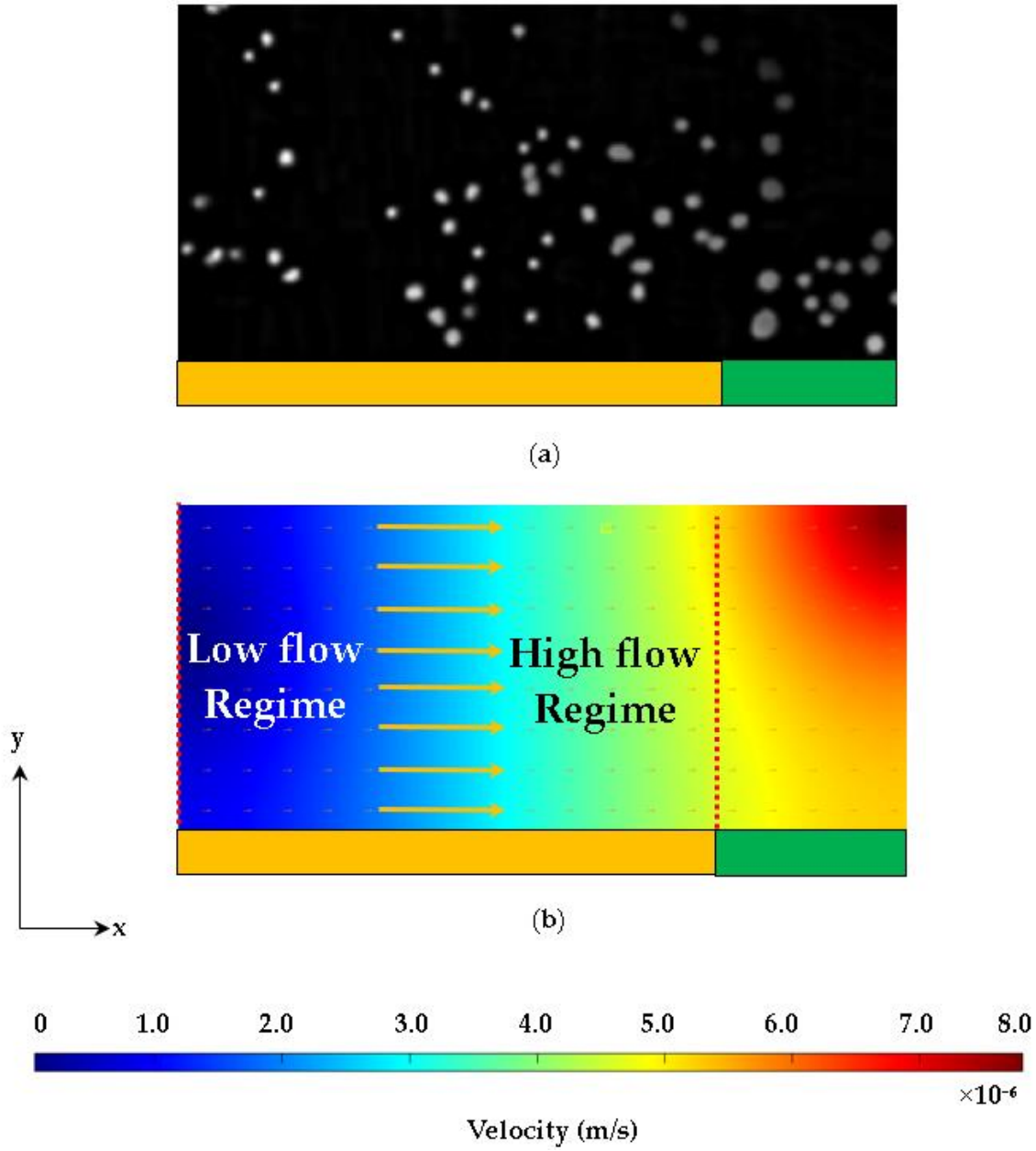

Figure 30: Overview of the particle image processing methodology in PIVlab (a) Top view of 4 µm diameter particles moving in the micro-channel under excitation and (b) The processed velocity contour image. The electrode (gold) and spacing (green) is shown below.

This phenomenon was observed in all studies, although some particles can be trapped at a given current, diameter, electrode size and spacing, and frequency. This is demonstrated later in section 3.5. To characterize the ferro-microfluidic device, we needed

to gain a baseline perspective of the influence of amperage amplitude, excitation frequency, electrode spacing, and particle size on particle dynamics. Sections 3.5 and 3.5.1 provides a detailed discussion on the particle dynamics for the electrode spacing, amperage, and frequency settings.

3.5 Large Electrode Spacing Study Results

For our initial studies, microspheres of a given individual size were initially mixed with the ferrofluid in small quantities and added to the microfluidic channel. We later introduced smaller 1 μm diameter particles with larger 10 μm diameter particles in the ferrofluid. For all studies, the particles were introduced into the microfluidic channel and the microchannel inlet and outlet was closed off at both ends to prevent fluid motion. Microspheres near the roof of the microchannel were imaged and processed in PIVLab. A current was applied to the electrodes to generate a traveling wave magnetic field within the microfluidic channel due to the phase differenced electrodes. Two electrode spacing studies are conducted in this *work (a small electrode spacing and large electrode spacing).* For both electrode spacing studies, the microspheres are randomly dispersed throughout the channel, prior to the current excitation. Depending on electrode spacing, the size-based particles can either be trapped between the electrodes or continuously pushed throughout the channel by the travelling wave magnetic field.

For the large electrode spacing studies, we observed that when current is applied, the non-magnetic particles are pushed away from the electrodes to the top of the channel *(due to the magnetic force*) where they start to rotate *(due to the magnetic torque)*. When the particles reach the top surface, their rotation leads to linear translation along the channel. It was observed that at low frequencies, the microspheres would localize between the

excitation electrodes, where the repulsive forces due to magnetic field gradients form a local minima. *Figure 31* below illustrates this phenomenon.

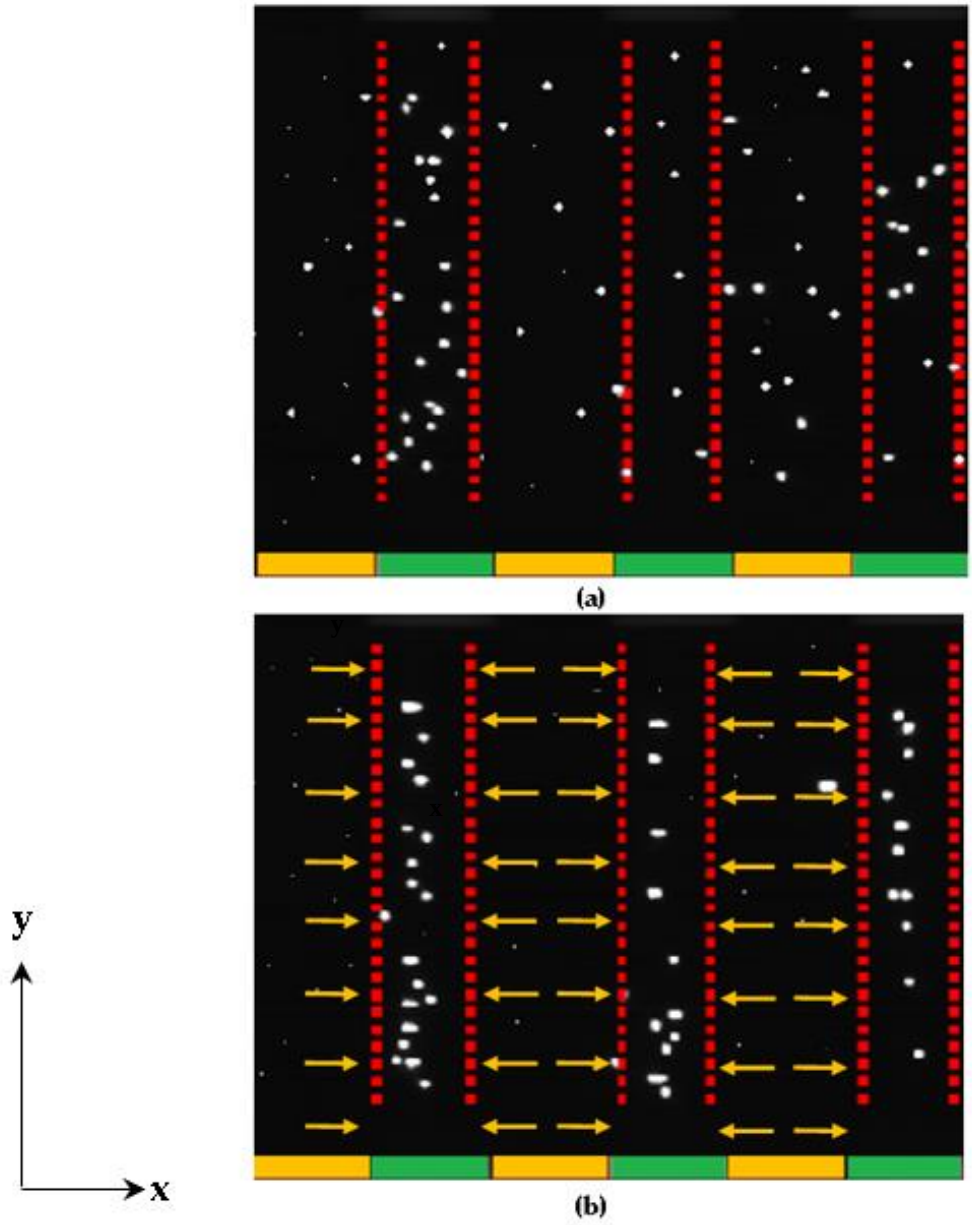

Figure 31: Top view of the microfluidic channel with the ferrofluid: (a) Image of 10 µm and 1 µm diameter microspheres randomly dispersed in the channel and (b) After the excitation, particles collect in the interelectrode spacing. The electrode (gold) and spacing (green) is shown below the figures.

As shown in *Figure 31*, the particles are randomly distributed in the channel. When the field is turn on at 6 A and with a frequency of 10 Hz, the larger particles tend to localize

in the space between the electrodes. The smaller 1 µm diameter particles appear to not be affected. *Figure 32* shows a cross-correlation processed imaged from PIVlab of the 10 diameter µm particles moving to the electrode spacing under the influence of the electrode excitation and frequency. As shown in *Figure 32*, the flow magnitudes appear to be the greatest at the electrodes. As mentioned previously, this because the electrodes create the force necessary for the particles to be pushed to the top of the channel, gain momentum, and translate across the channel at a given frequency and amperage. *Figure 32* shows a plot of the extracted velocity plotted in the middle of the channel and across the electrode region. The extraction line is shown in *Figure 32 (red arrow pointing to the line)*.

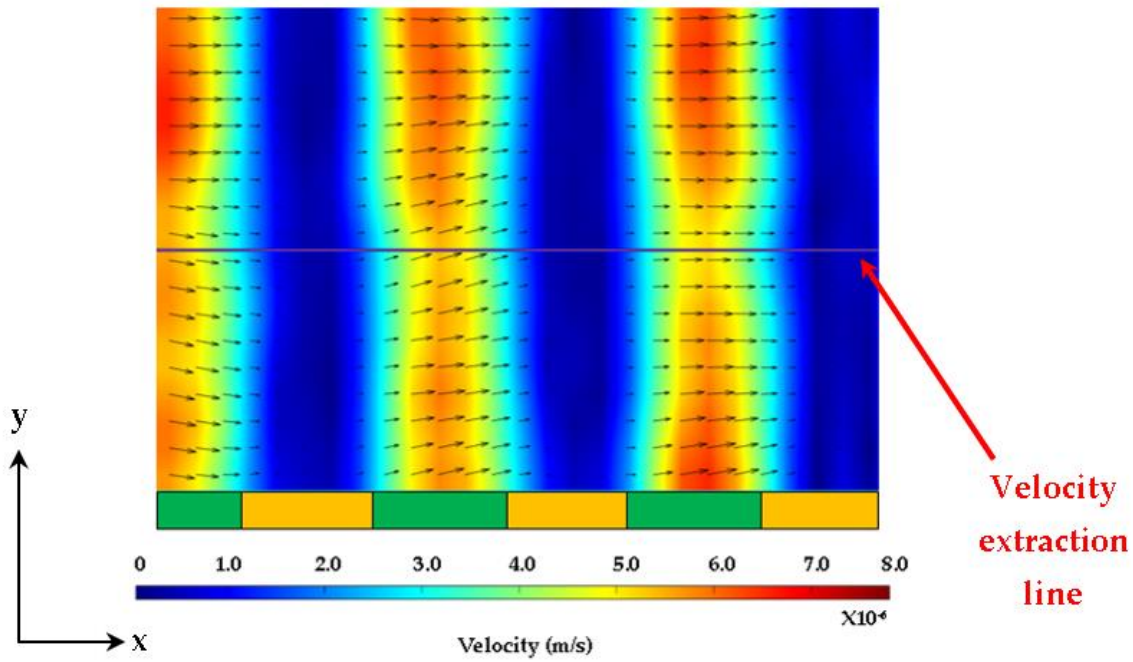

Figure 32: Velocity contour of 10 particles moving between the electrodes at 10Hz and with a large electrode spacing. The electrode (gold) and spacing (green) is shown below the figure.

As shown in *Figure 33*, the velocity profile has a sinusoidal profile similar to the trend of the phase differenced input currents. The plot indicated that the velocity increases

in the electrode spacing regions and decreases at the electrodes. *Figure 34* shows a histogram of the velocity amplitudes in the processed image.

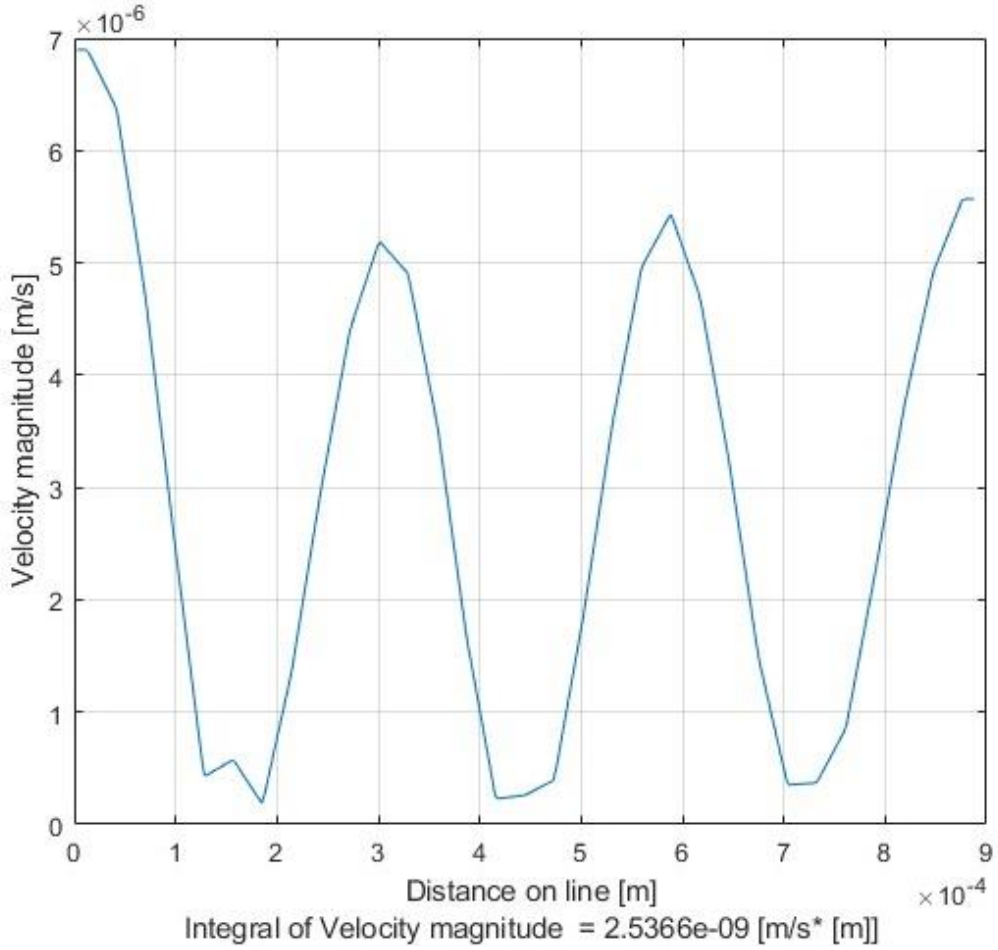

Figure 33: Plot of the velocity distribution in the middle of the channel and across the electrode region.

Unlike the velocity distribution, the histogram provides information on frequency distribution of velocity magnitudes with the entire data set of images. The negative sign indicates the direction. As shown in *Figure 34*, the highest velocity observed has the least occurrence, whereas the lowest velocity to no movement occurs the most. This indicates that the particles move from the highest force region at a high magnitude velocity and then comes to rest between the electrodes.

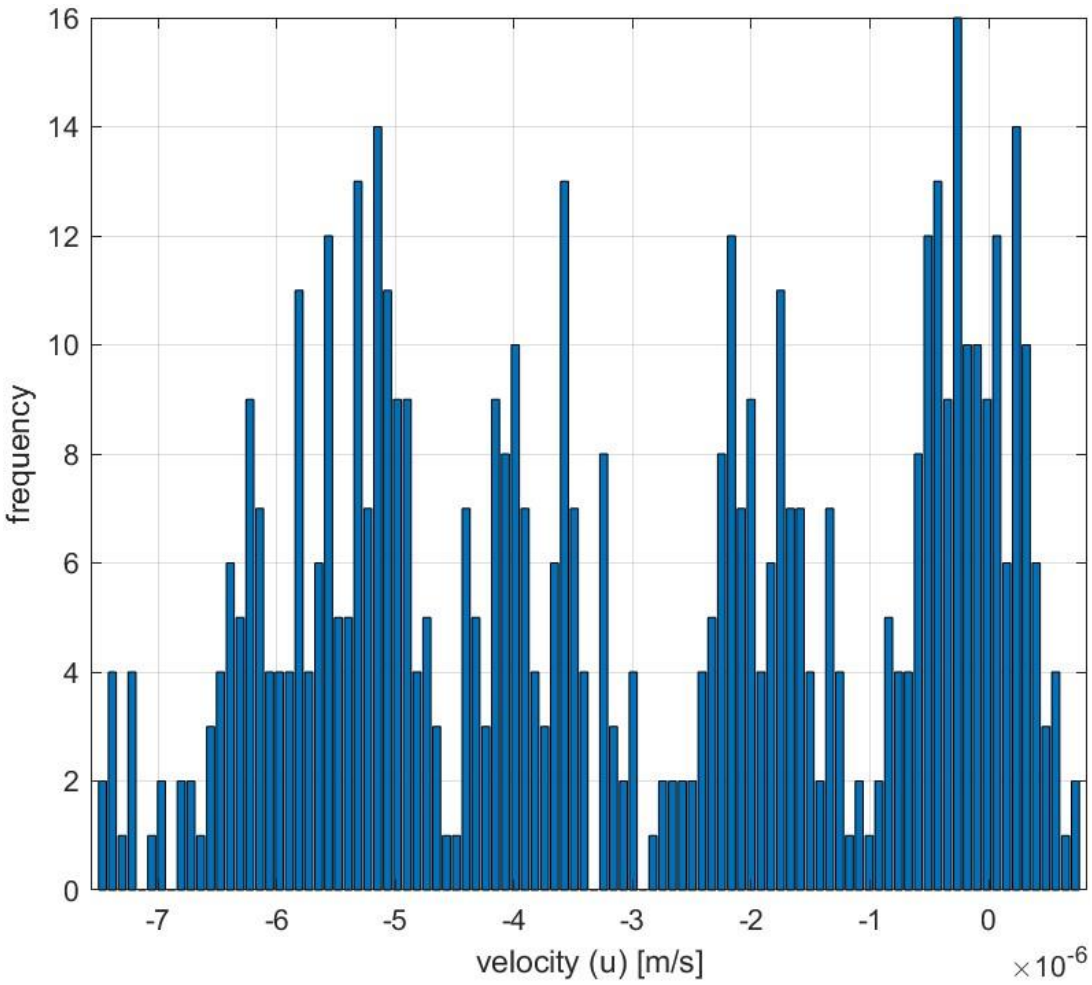

Figure 34: Histogram of the velocity distribution from the image dataset.

3.5.1 Small Electrode Spacing Study Results

For the small electrode spacing experimental studies, we observed that when current is applied to the electrodes, the particles tend to move to the top surface of the channel and translate along the roof of the channel. Unlike the large electrode spacing chip experimental studies, the smaller electrode spacing leads to more kinetic energy in the fundamental mode of the traveling wave excitation. As mentioned previously, it also reduces the lateral field gradient between the electrodes. In this manner, smaller electrode spacings will lead to faster microsphere travel and a reduction in the critical frequency for trapping. *Figure 35* below illustrates this effect.

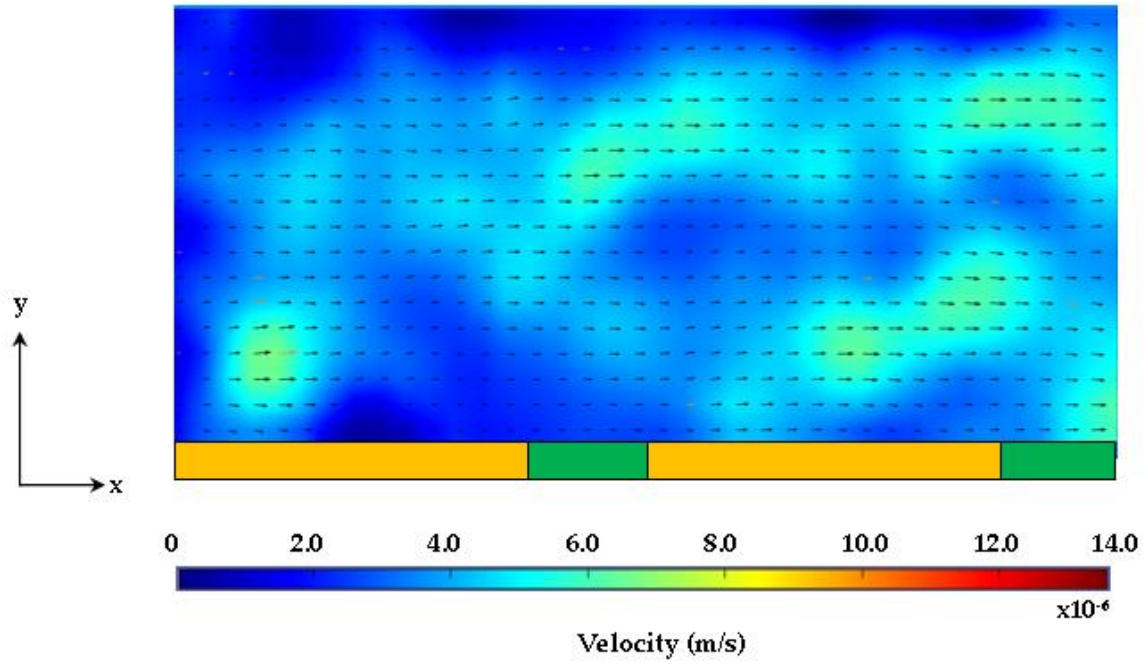

Figure 35: Velocity contour of 1 µm diameter particles under 750 mA and 10 Hz.

Figure 35 shows a processed velocity contour of 1 µm diameter fluorescent particles moving in the microchannel at a low amperage setting of 750 mA and a frequency setting of 10 Hz. Surprisingly, at a low amperage setting, the 1 µm diameter particles can be continously pushed through the channel *(from left to right)*. It appears that the small spaced electrodes creates a ratcheting effect of continuously pushing particles downstream regardless of the current setting for the 1 µm diameter particles. *Figure 36* shows a velocity contour of the 10 µm diameter fluorescent particles moving in the microchannel at a low amperage setting of 4 A and a frequency setting of 10 Hz. The velocity magnitude has increased due to the increased amperage. It also appears that the electrodes creates the ratcheting effect for larger particles as well. As shown in *Figure 36*, the velocity

magnitude is lower at the first electrode and then increases at the electrode space and increases at the second electrode.

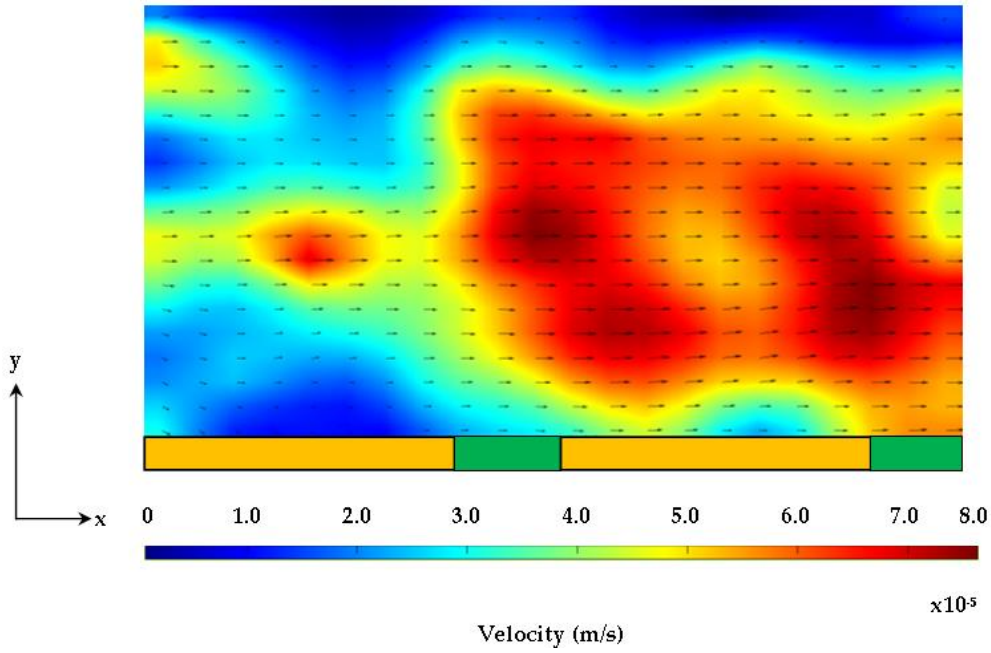

Figure 36: Velocity contour of 10 µm diameter fluorescent particles at 4 A and 10 Hz.

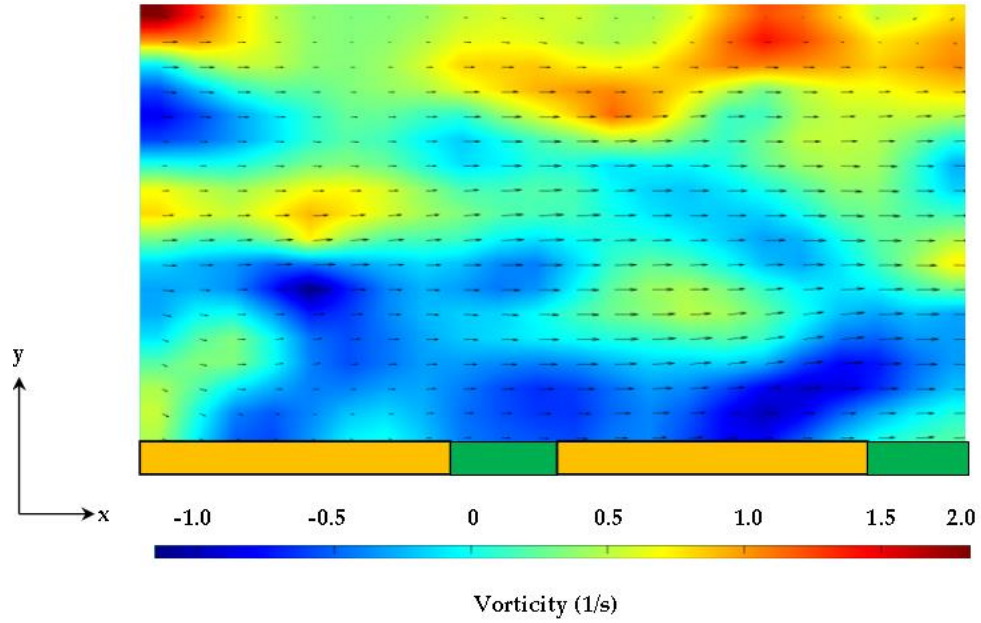

Figure 37: Vorticity contours of 10 µm diameter fluorescent particles at 4 A and 10 Hz.

Figure 37 shows the voritcity contour for the same image of 10 µm moving in the microchannel. Vorticity is a measure of the spin of the fluid. As shown in the contour, the highest spin is experienced near the edges of the electrodes which indicate the regions where the magnetic push and pull forces are the highest. This push and pull effect creates the ratcheting effect mentioned previously. This is also demonstrated in the centerline velocity distribution plotted in *Figure 38*. The velocity centerline plot shows that the highest velocity occurs near the edges of the second electrode. The velocity profile *(wall to wall)* is extracted at the middle fo the first electrode and shown in *Figure 39*. The velocity profile shows that the flow is laminar and and slightly fully developed. The no slip condition is not captured in the image due to glaring of scattered light.

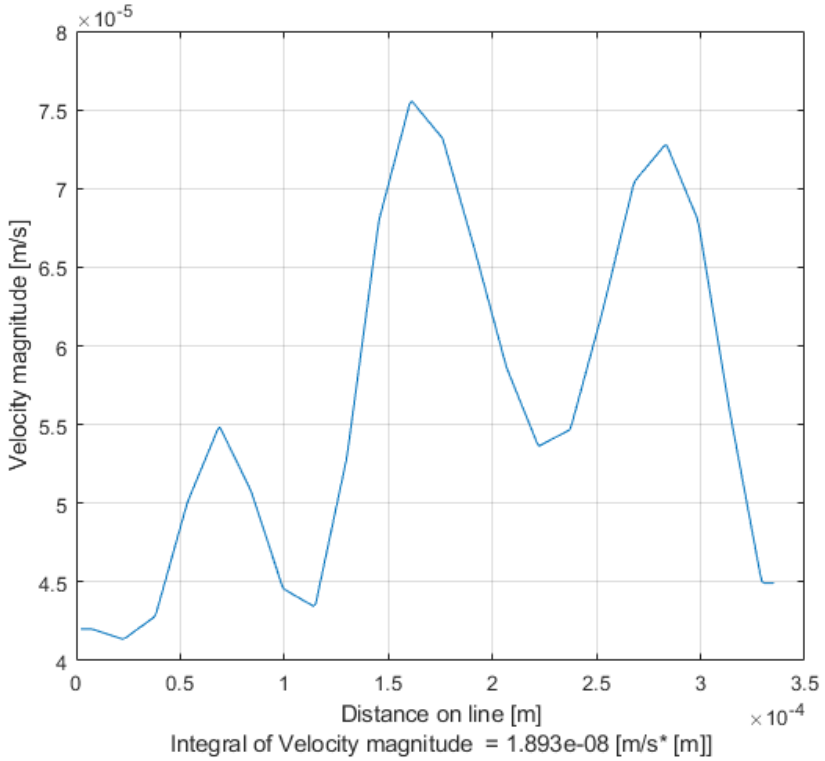

Figure 38: Velocity distribution extraction from the centerline of the 10 µm diameter particle study at 4 A and 10 Hz.

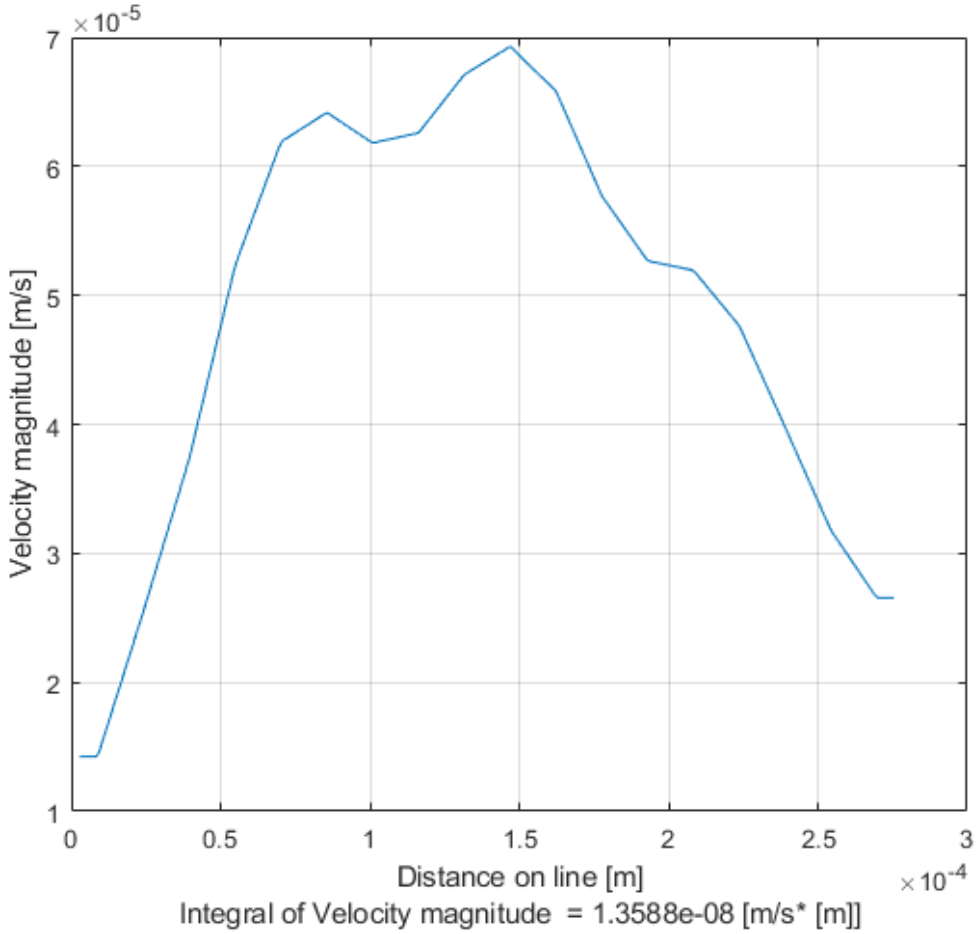

Figure 39: Velocity profile extraction from the middle of the first electrode for the 10-diameter particle study at 4 A and 10 Hz.

Figure 40 shows the images of 1 µm and 10 µm diameter particles randomly dispersed in the ferrofluid within the microchannel. The current is set to 6A with a frequency of 10Hz. Similar to the 1 µm diameter particle studies, the particles continuously translate along the roof of the channel. This behavior was consistent at various frequencies of 10, 100, 1000, and 10000 Hz.

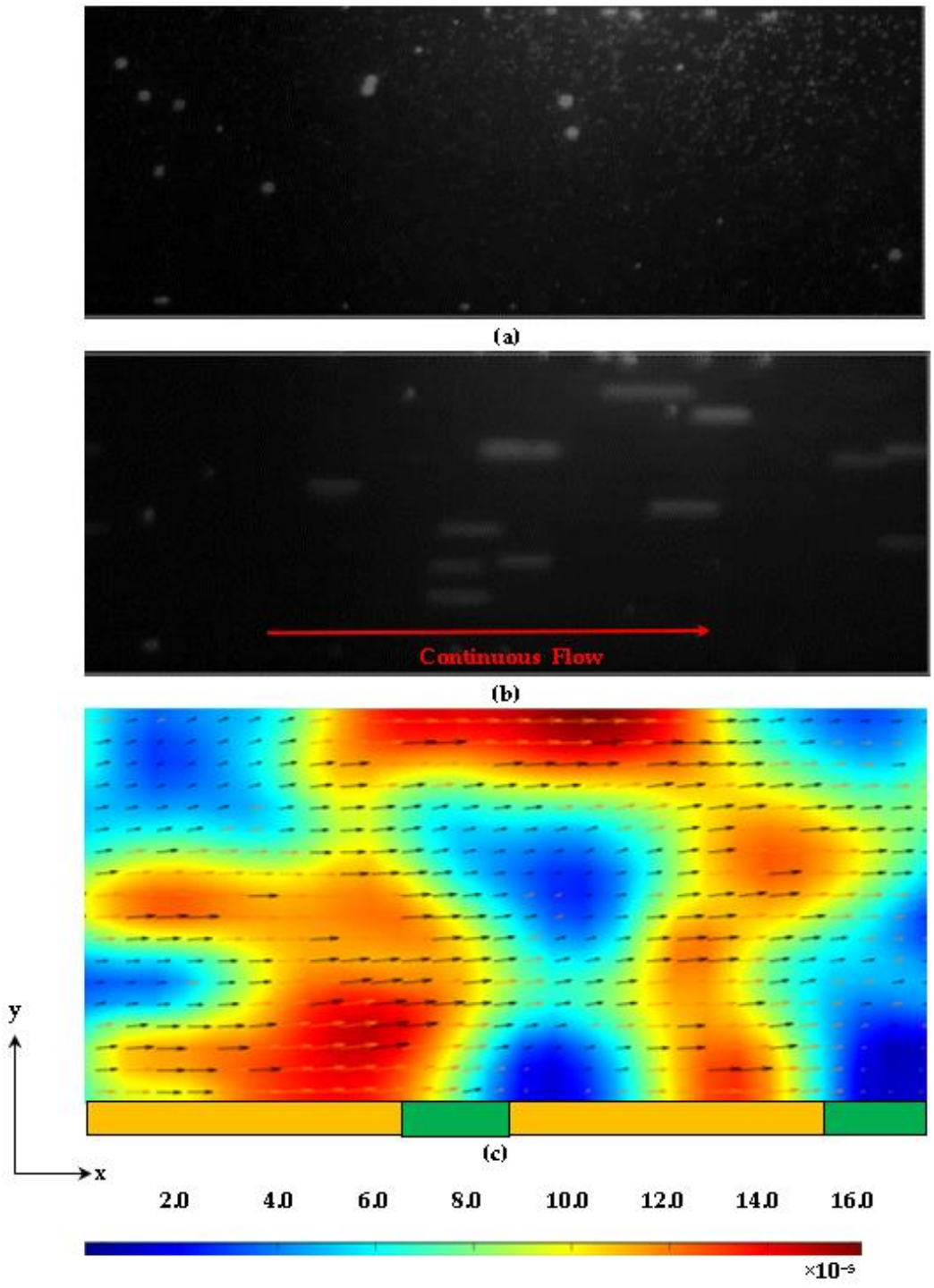

Figure 40: Velocity contour of 1um diameter fluorescent particles at 6A and 10Hz.

CHAPTER 4: CONCLUSION

The design and development of a simple traveling wave ferro-microfluidic device and system rig purposed for the potential manipulation and magnetophoretic separation of cells in a water-based ferrofluid was presented. This work consisted of designing a heat dissipation system for effectively removing heat during particle manipulation studies, fabricating cobalt ferrite nanoparticles, tailoring a water-base ferrofluid for particle manipulation studies, and conducting particle dynamic studies for characterizing the behavior of particles under an applied amperage, frequency, and underlying electrode spacing.

Experimental studies were carried out using two different diameter sizes of non-magnetic *(fluorescent microsphere)* particles. These studies have demonstrated the ability to trap large 10 μm diameter particles at small frequencies using large electrode spacing and continuously pushing particles through the channel with smaller electrode spacing regardless of the particle size. The results reported in this work demonstrate a proof of concept for magnetophoretic manipulation and separation of magnetic and non-magnetic nanoparticles in a simple ferro-microfluidic device. This work is a design and proof of concept study. From a heat transfer perspective, the design reported in this work is an improvement over existing travelling wave ferro-microfluidic designs in that heat is efficiently removed from the circuit board to allow a range of input currents and frequencies to manipulate non-magnetic particles. The results reported in this work establish that the developed ferro-microfluidic device may potentially be used as an effective platform for microparticle and cellular manipulation and sorting.

The major finding in this work is that the velocity of the microspheres depends on the excitation frequency, current amplitude, electrode spacing and their position with respect to the underlying electrodes. The key contributions of this work are:

1. A method for tailoring preferred size range *(10-20nm)* magnetic cobalt ferrite magnetic nanoparticles.
2. The development of a ferro-microfluidic device for potentially separating cells and magnetic microparticles without detrimental thermal affects.
3. The development of a water-based ferrofluid with magnetic and non-magnetic particles as surrogates for biological cells.
4. The design and development of a rig for producing the electric field within the ferro-micro fluidic device for magnetizing the magnetic nanoparticles and manipulating nanoparticles in static and dynamic flow while efficiently removing heat from the electrode base.
5. A method for measuring the surrounding fluid and particle velocity, vorticity and characterizing particle dynamics in the developed ferrofluid.
6. An approach for separating magnetic and non-magnetic nanoparticles that could potentially be an advantage in that particle manipulation will not rely on labeling or surface modification, significantly reducing operation time and cost compared to conventional approaches.

Future work should include:

1. Using a particle tracking code for particle dynamics studies as opposed to a cross-correlation methodology.

2. Refining the chip base design to incorporate thicker copper electrodes *(in the direction of the thickness of the PCB*) for smaller resistance in the electrodes. This would possibly result is less heat for any given excitation current.
3. Investigate different electrode metallic core materials to provide a more effective path for heat to flow away from the magnetic excitation pattern.
4. Develop different electrode patterns *(square and curved*) with varying sizes on one chip to characterize the behavior of particles under varying amperage and frequencies for both static and dynamic flow. Conducting further studies using this approach will allow us to establish the feasibility of this approach for potentially separating cells.
5. Conduct particle dynamic characterization studies using commercial ferrofluids such as EMG 700 with varying electrode patterns, amperage settings, frequency setting and non-magnetic particle sizes for both static and dynamic flow.
6. Tailor biocompatible ferrofluids and conduct cellular based studies such as separating bacteria from magnetic particles in dynamic flow studies.

REFERENCES

1. Rosenweig, R.E., *"Ferrohydrodynamics"*. New York: Cambride Press, 1985.
2. Gordon, R.T., Hines, J.R., and Gordon D., *"Intracellular Hyperthermia a Biophysical Approach to Cancer Treatment via Intracellular Temperature and Biophysical Alterations."*. Medical Hypotheses, 1979. **5**(1).
3. Kim, D.K., et al., *"Starch-Coated Superparamagnetic Nanoparticles as MR Contrast Agents"*. Chemistry of Materials, 2003. **15**(23): p. 4343-4351.
4. Hewlin, R.L., Jr., Edwards, M., and Schultz, C., *"Design and Development of a Travelling Wave Ferro-Microfluidic Device and System Rig for Potential Magnetophoretic Cell Separation and Sorting in a Water-Based Ferrofluid"*. Micromachines, 2023. **14**(889).
5. Nabovati, G., Ghafar-Zadeh, E., Letourneau, A., et al., *"Towards High Throughput Cell Growth Screening: A New CMOS 8 × 8 Biosensor Array for Life Science Applications"*. IEEE Transactions on Biomedical Circuits and Systems, 2016. **11**(2).
6. Azizipour, N., Avazpour, R., Rosenzwieg, D.H., et al., *"Evolution of Biochip Technology: A Review from Lab-on-a-Chip to Organ-on-a-Chip"*. Micromachines (Basel), 2020. **11**(6).
7. Gimsa, J., Marszalek, P., Loewe, U., and Tsong, T.Y., *Dielectrophoresis and electrorotation of neurospora slime and murine myeloma cells.* . Biophys J. 1991 1991. **60**(4): p. 749-760.
8. Phol, H.A., *"Dielectrophoresis: The Behavior of Neutral Matter in Non-uniform Electric Field"*. Cambridge University Press, Cambridge, 1978.
9. Pommer, M.S., Zhang, Y., Keerthi, N., Chen, D., Thomson, J.A., Meinhart, C.D., and Soh, H.T., *"Dielectrophoretic Separation of Platelets From Diluted Whole Blood in Microfluidic Channels"*. Electrophoresis, 2008. **29**(6): p. 1213.
10. Lorenz, M., Malangré, D., Du, F. et al., *"High-Throughput Dielectrophoretic Filtration of Sub-micron and Micro Particles in Macroscopic Porous Materials"*. Anal Bioanal Chem, 2020. **412**: p. 3903-3914.
11. Hewlin, J., R.L, and Edwards. M., *"Continuous Flow Separation of Red Blood Cells and Platelets in a Y-Microfluidic Channel Device with Saw-Tooth Profile Elec-trodes via Low Voltage Dielectrophoresis"*. Current Issues in Molecular Biology, 2023. **3**.
12. Kang, Y., Li, D., Kalams, S.A., and Eid, J.E, *"DC-Dielectrophoretic Separation of Biological Cells by Size"*. Biomed. Microdevices, 2008. **10**: p. 243-249.
13. Chen, D.F., Du, H., and Li, W.H., *"Bioparticle Separation and Manipulation Using Dielectrophoresis"*. Sens. Actuators A Phys., 2007. **133**: p. 329-334.
14. Zao, K., and Li, D., *"Manipulation and Separation of Oil Droplets by Using Asymmetric Nano-Orifice Induced DC Dielectrophoretic Method"*. J. Colloid Interface Sci., 2018(512): p. 389-397.
15. Zhao, K., and Li, D., *"Tunable Droplet Manipulation and Characterization by Ac-DEP"*. Interfaces, 2018. **10**: p. 36572-36581.
16. Gascoyne, P.R.C., and Vykoukal, J., *"Particle Separation by Dielectrophoresis"*. Electrophoresis, 2002. **23**: p. 1973.
17. Sajeesh, P., and Sen, A.L., *"Particle Separation and Sorting in Microfluidic Devices: A Review"*. Microfluid. Nanofluid, 2014. **17**: p. 1-52.
18. Zhao, K., Peng, R., and Li, D., *"Separation of Nanoparticles by an Nano-Orifice Based DC-Dielectrophoresis Method in a Pressure-Driven Flow"*. Nanoscale, 2016. **8**: p. 18945-18955.
19. Yamashita, M., Inoue, H., and Miyata, S., *"Platelet-Rich Plasma Purification by Dielectrophoresis and Fluid-Induced Shear Force"*. Bioelectricity, 2022. **4**(4): p. 190-197.
20. Zhao, K., Zhao, P., Dong, J., Wei, Y., Chen, B., Wang, Y., Pan, X., and Wang, J., *"Implementation of an Integrated Dielectrophoretic and Magnetophoretic Microfluidic Chit for CTC Isolation"*. Biosensors (Basel), 2022. **12**(9): p. 757.
21. Li, H., and Bashir, R., *"Dielectrophoretic Orientation, Manipulation and Separation of Live and Heat-Treated Cells of Listeria on Microfabricated Devices with Interdigitated Electrodes"* Cambridge University Press: Cambridge, UK, 2002. **729**: p. 1-6.
22. Gascoyne, P., Mahidol, C., Ruchirawat, M., Satayavivad, J., Watcharasit, P, and Becker, F.F., *"Microsample Preparation by Dielectrophoresis: Isolation of Malaria"*. Lab Chip, 2002. **2**: p. 70-75.

23. Moon, H.S., Kwon, K., Kim, S.I., Han, H., Sohn, J., Lee, S., and Jung, H.I., *"Continous Separation of Breast Cancer Cells from Blood Samples Using Multi-Orifice Flow Fractionation (MOFF) and Dielectrophoresis (DEP).* Lab Chip, 2011. **11**: p. 1118-1125.
24. Song, H., Rosano, J.M., Wang, Y., Garson, C.J., Prabhakarpandian, B., Pant, K., Klarmann, G.J., Perantoni, A., Alvarez, L.M., and Lai, E., *"Continous-Flow Sorting of Stem Cells and Differentiation Products Based on Dielectrophoresis.* . Lab Chip, 2015. **15**: p. 1320-1328.
25. Wang, Y., Wang, J., Wu, X., Jiang, Z., and Wang, W., *"Dielectrophoretic Separation of Microalgae Cells in Ballast Water in a Microfluidic Chip.* Electrophoresis, 2019. **40**: p. 969-978.
26. Vahey, M.D., and Voldman, J., *"An Equilibrium Method for Continuous-Flow Cell Sorting Using Dielectrophoresis".* Anal. Chem., 2008. **80**: p. 3135-3143.
27. Cao, Z., Zhu, Y., Liu, Y., Dong, S., Chen, X., Bai, F., Song, S., and Fu, J., *"Dielectrophoresis-Based Protein Enrichment for a Highly Sensitive Immunoassay Using Ag/SiO2 Nanorod Assays.* Small, 2018. **14**: p. 1703265.
28. Kung, Y.C., Huang, K.W., Chong, W., and Chio, P.Y., *"Tunnel Dielectrophoresis for Tunable, Single-Stream Cell Focusing in Physiological Buffers in High-Speed Microfluidic Flows".* Small, 2016. **12**: p. 4343-4348.
29. Menachery, A., and Pethig, P., *"Controlling Cell Destruction Using Dielectrophoretic Forces".* NanoBiotechnology, 2005. **152**: p. 145-149.
30. al., M.e., *"The Potential of Dielectrophoresis for Single-Cell Experiments".* IEEE Eng. Biol. Med. Mag., 2003. **22**: p. 51-61.
31. Sebastian, A., Buckle, A.M., and Markx., G.H., *"Formation of Multilayer Aggrefates of Mammalian Cells by Dielectrophoresis".* J. of Micromech. Microeng., 2006. **16**: p. 1769-1777.
32. Gijs, M., *"Magnetic Bead Handling On-Chip: New Opportunities for Analytical Applications".* Microfluidic Nanofluidics, 2004. **1**: p. 22-40.
33. Davis, J.A., et al., *"Deterministic Hydrodyanmics: Taking Blood Apart".* Proc Natl Acad Sci USA, 2006. **103**: p. 14779-14784.
34. Sutermaster, B.A., and Darling, E.M, *"Considerations for High-Yield, High-Throughput Cell Enrichment: Fluorescence versus Magnetic Sorting".* Sci Rep., 2019. **9**(1): p. 227.
35. Shamloo, A., Naghdloo, A., and Besanjideh, M., *"Cancer Cell Enrichment on a Centrifugal Microfluidic Platform Using Hydrodynamic and Magnetophoretic Techniques".* Sci. Rep., 2021. **11**(1): p. 1939.
36. Yang, L., Wujun, Z., Cheng, R., et al., *"Fundamentals of Integrated Ferrohydrodynamic Cell Separation in Circulating Tumor Cell Isolation".* Lab Chip, 2021. **21**(1706).
37. Liu, Y., Vieira, R.M.S., and Mao, L., *"Simultaneous and Multimodal Antigen-Binding Profiling and Isolation of Rare Cells via Quantitative Ferrohydrodynamic Cell Separation".* ACS Nano 2023. **17**(1): p. 94-110.
38. Pandey, S., Mehendale, N, and Paul, D., *"Single-Cell Separation". In: Santra, Tseng, F.G., (eds) Handbook of Single Cell Technologies.* Springer , Singapore, 2022.
39. Lu, N., Tay, H.M., Charyakorn, P, et al., *"Label-Free Microfluidic Cell Sorting and Detection for Rapid Blood Analysis".* Lab Chip, 2023. **23**(1226).
40. Kose, A.R., Fischer, B., Mao, L., and Koser, H., *"Label-free cellular manipulation and sorting via biocompatible ferrofluids".* Applied Biological Sciences, 2009. **106**: p. 21478-21483.
41. Kose, A.R., and Koser, H., , *"Ferrofluid Mediated Nanocytometry".* Lab Chip, 2012. **12**(1): p. 190-196.
42. Zhao, W., Zhu, T., Rui, C., et al., *"Label-Free and Continuous-Flow Ferrohydrodynamic Separation of HeLa Cells and Blood Cells in Biocompatible Ferrofluids".* Adv. Funct. Mater., 2016. **14**(26): p. 3990-3998.
43. Xuan, X., *"Recent Advances in Continuous-Flow Particle Manipulations Using Magnetic Fluids".* MIcromachines (Basel), 2019. **10**(11): p. 744.
44. Kashevsky, B.E., *"Nonmagnetic Particles in Magnetic Fluid: Reversal Dynamics Under Rotating Fields".* Phys Fluids, 1997: p. 1811-1818.
45. Rosensweig, R.E., *"Ferrohydrodynamics".* (Dover, New York, 1997), 1997.
46. Odenback, S., *"Magnetically Controllable Fluids and Their Applications".* (Springer, New York), 2002.
47. Edwards. M. and Hewlin, J., R.L., *"A Computational Model for Analysis of Field and Force and Particle Dynamics in a Ferro-Magnetic Microfluidic System".* Proceedings of the ASME 2022

International Mechanical Engineering Congress and Exposition. Volume 4: Biomedical and Biotechnology; Design, Systems, and Complexity. Columbus, Ohio, USA. October 30–November 3, 2022. V004T05A007. ASME. https://doi.org/10.1115/IMECE2022-95690, 2022.

48. Edwards, M., Hewlin, Jr., R.L., and Smith, M., *"A 2-D Transient Computational Multi-Physics Model for Analyzing Magnetic and Non-Magnetic (Red Blood Cells and E. Coli Bacteria) Particle Dynamics in a Travelling Wave Ferro-Magnetic Microfluidic Device".* ASME Journal of Engineering and Science for Medical Therapis and Diagnosis (Paper Accepted), 2023.
49. Yellen, B.B., Hovorka, O., and Friedman, G., *"Arranging Matter by Magnetic Nanoparticle Assemblers".* Proc. Natl. Acad. Sci USA, 2005. **102**: p. 8860-8864.
50. Yellen, B.B., Erb, R.M., Son, HS., Hewlin, Jr, R.L., et al., *"Travelling Wave Magnetophoresis for High Resolution Chip Based Separations".* Lab on a Chip, 2007. **7**: p. 1681-1688.
51. Hewlin, J., R.L., Ciero, A., and Kizito, J.P., *"Development of a Two-Way Coupled Eulerian–Lagrangian Computational Magnetic Nanoparticle Targeting Model for Pulsatile Flow in a Patient-Specific Diseased Left Carotid Bifurcation Artery".* Journal of Cardiovascular Engineering and Technology, 2019. **10**: p. 299-313.
52. Hewlin, J., Smith, M.S., and Kizito, J.P., *"Computational Assessment of Unsteady Flow Effects on Magnetic Nanoparticle Targeting Efficiency in a Magnetic Stented Carotid Bifurcation Artery".* Journal of Cardiovascular Engineering and Technology, (In Review), 2022.
53. Stanley, N., Ciero, A., Timms, W., and Hewlin, Jr., R.L., *"Development of 3-D Printed Optically Clear Rigid Anatomical Vessels for Particle Image Velocimetry Analysis in Cardiovascular Flow.".* Proceedings of the ASME 2019 International Mechanical Engineering Congress and Exposition. Volume 7: Fluids Engineering. Salt Lake City, Utah, USA. November 11–14, 2019. V007T08A004. ASME. https://doi.org/10.1115/IMECE2019-11649, 2019.
54. Hewlin, R.L., Jr., and Tindal, J.M., *"Computational Assessment of Magnetic Nanoparticle Targeting Efficiency in a Simplified Circle of Willis Arterial Model".* Int. J. Mol. Sci., 2023. **24**(2545).
55. Edwards, M., and Hewlin, Jr, R.L., *"A Computational Model for Analysis of Field Force and Particle Dynamics in a Ferro-Magentic Microfluidic System".* Proceedings of the ASME 20122 International Mechanical Engineering Congress and Exposition, Akron, Ohio, USA. October 30-November 3, 2022, 2022.
56. Jones, T., *"Electromechanics of Particles".* Cambridge University Press, 1995.
57. Hewlin, R.L., Jr., and Kizito, J.P., *"Comparison of Carotid Bifurcation Hemodynamics in Patient-Specific Geometries at Rest and During Exercise"* Proceedings of the ASME 2013 Fluids Engineering Division Summer Meeting. Volume 1A, Symposia: Advances in Fluids Engineering Education; Advances in Numerical Modeling for Turbomachinery Flow Optimization; Applications in CFD; Bio-Inspired Fluid Mechanics; CFD Verification and Validation; Development and Applications of Immersed Boundary Methods; DNS, LES, and Hybrid RANS/LES Methods. Incline Village, Nevada, USA. July 7–11, 2013. V01AT04A001. ASME. https://doi.org/10.1115/FEDSM2013-16248, 2013.
58. Hewlin, R.L., Jr., and Kizito, J.P., *"Evaluation of the Effect of Simplified and Patient-Specific Arterial Geometry on Hemodynamic Flow in Stenosed Carotid Bifurcation Arteries".* ASME Early Career Technical Journal, 2011. **10**: p. 39-44.
59. COMSOL, *"COMSOL MultiPhysics Reference Manual".* Obtained from: https://doc.comsol.com/5.5/doc/com.comsol.help.comsol/COMSOL_ReferenceManual.pdf, Obtained on 12/14/2022.
60. Morsi, S.A. and Alexander, A.J., *"An Investigation of Particle Trajectories in Two-Phase Flow Systems".* Journal of Fluid Mechanics, 1972. **55**(2): p. 193-208.
61. Haider, A., and Levenspiel, O., *"Drag Coefficient and Terminal Velocity of Spherical and Nonspherical Particles".* Powder Technology, 1989. **58**: p. 63-70.
62. Ounis, H., Ahmadi, G., and McLaughlin, J.B., *"Brownian Diffusion of Submicrometer Particles in Viscous Sublayer".* Journal of Colloid and Interface Science, 1991. **143**(1): p. 266-277.
63. Verwey, E.J.W.a.O., J., and Th.,G., *"Theory of Stability of Lyophobic Colloids".* Amsterdam: Elsevier, 1948.
64. Lopez-Ortega, A., Lottini, E., Fernandez, C.J., et al., *"Exploring the Magnetic Properties of Cobalt-Ferrite Nanoparticles for the Development of a Rare-Earth-Free Permanent Magnet".* Chem. Mater., 2015. **27**: p. 4048-4056.

65. Maaz, K., Mumtaz, A., Hasanain, S.K., and Ceylan, A., *"Synthesis and Magnetic Properties of Cobalt Ferrite (CoFe2O4) Nanoparticles Prepared by Wet Chemical Route".* Jour. Magn. and Magn. Mater., 2007. **308**(2): p. 289-295.
66. Cheng, C., Dai, J., Li, Z., and Feng, W., *"Preparation and Magnetic Properties of CoFe2O4 Oriented Fiber Arrays by Electrospinning".* Materials, 2020. **13**(17).
67. Tsang, E., and Morris, J., *"Magnetic Susceptibility of Escherichia Coli".* Jour. Magn. and Magn. Mater., 1985. **51**(1-3): p. 355-358.
68. Zborowski, M., Ostera, G.R, Moore, L.R., et al., *"Red Blood Cell Magnetophoresis".* Biophys. J., 2003. **84**(4).
69. Spees, W.M., Yablonskiy, D.A., Oswood, M.C., and Ackerman, J.J.H., *"Water Proton MR Properties of Human Blood at 1.5 Tesla: Magnetic Susceptibility, T1, T2, T2*, and Non-Lorentzian Signal Behavior".* Magnetic Resonance in Medicine, 2001. **45**: p. 533-542.
70. Cerdonio, M., Congio-Castellano, A., Calabrese, L., et al. , *"Room-Temperature Magnetic Properties of Oxy-and Carbonmonoxyhemoglobin".* PNAS, 1978. **75**(10).
71. Cerdonio, M., Morante, S., Torresani, D., et al., *"Reexamination of the Evidence for Paramagnetism in Oxy- and Carbonmonoxyhemoglobins".* PNAS, 1985. **82**(1): p. 102-103.
72. Kuchel, P.W.C., C.D., Daners, D., Shishmarev, D., and Galvosas, P., *"Surface Model of Human Red Blood Cell Simulating Changes in Membrane Curvature Under Strain".* Scientific Reports, 2021. **11**(13712).
73. Jahangir, S.M., Hu, HG., and Lingke, Y., *"Simulation of Red Particles in Blood Cell".* Applied Mechanics and Materials 2013. **477-478**: p. 330-334.
74. Nahavandi, M., *"Continuous-Flow Separation of Malaria-Infected Human Erthrocytes Using DC Dielectrophoresis: An Electrokinetic Modeling and Simulation".* Industrial & Engineering Chemistry Research, 2016. **55**(19): p. 5484-5499.
75. Kumar, C.L., Juliet, A.V., Ramakrishna, B., Chakraborty, S., Mohammed, M.A., and Sunny, K.A., *"Computational Microfluidic Channel for Separation of Escherichia Coli from Blood-Cells".* CMC-Computers Materials & Continua, 2021. **67**(2): p. 1369-1384.
76. Karampelas, I.H., and Gomez-Pastora, J., *"Novel Approaches Concerning the Numerical Modeling of Particle and Cell Separation in Microchannels: A Review".* Processes, 2022. **10**(6).
77. Stanley, N., Ciero, A., Timms, W., and Hewlin, Jr., R.L>, *"A 3-D Printed Optically Clear Rigid Diseased Carotid Bifurcation Arterial Mock Vessel Model for Particle Image Velocimetry Analysis in Pulsatile Flow".* ASME Open J. Engineering ASME. , 2023.
78. Hewlin, J., R.L., and Kizito, J.P., *"Development of an Experimental and Digital Cardiovascular Arterial Model for Transient Hemodynamic and Postural Change Studies: "A Preliminary Framework Analysis".* Cardiovasc Eng Tech, 2018. **9**: p. 1-31.
79. Hewlin, J., R.L., *"Transient Cardiovascular Hemodynamics in a Patient-Specific Arterial System".* Dissertation, 2015.
80. Crooks, J.M., Hewlin, Jr., R.L., and Williams, W.B., *"Computational Design Analysis of a Hydrokinetic Horizontal Parallel Stream Direct Drive Counter-Rotating Darrieus Turbine System: A Phase One Design Analysis Study".* Energies, 2022. **15**(8942).
81. Su, P., Ren, C.H., Fu, Y.S., et al., *"Magnetophoresis in Microfluidic Lab: Recent Advance".* Sensors and Actuators A-Physical, 2021. **332 Part 2**.
82. Hewlin, J., R.L. and Kizito, J.P., *"Development of a Capacitance Based Void Fraction Sensor for Two-Phase Flow Measurement".* Proceedings of the ASME 2013 Fluids Engineering Division Summer Meeting. Volume 2, Fora: Cavitation and Multiphase Flow; Fluid Measurements and Instrumentation; Microfluidics; Multiphase Flows: Work in Progress. Incline Village, Nevada, USA. July 7–11, 2013, 2013.
83. Hewlin, J., R.L., *"Development of Digital Diagnostics and Measurement Tools for a High Heat Flux Thermal Loop".* Graduate Thesis, 2010.
84. Tung, L.D., et al., *"Magnetic Properties of Ultrafine Cobalt Ferrite Particles.".* Journal of Applied Physics, 2003. **93**(10): p. 7486-7488.

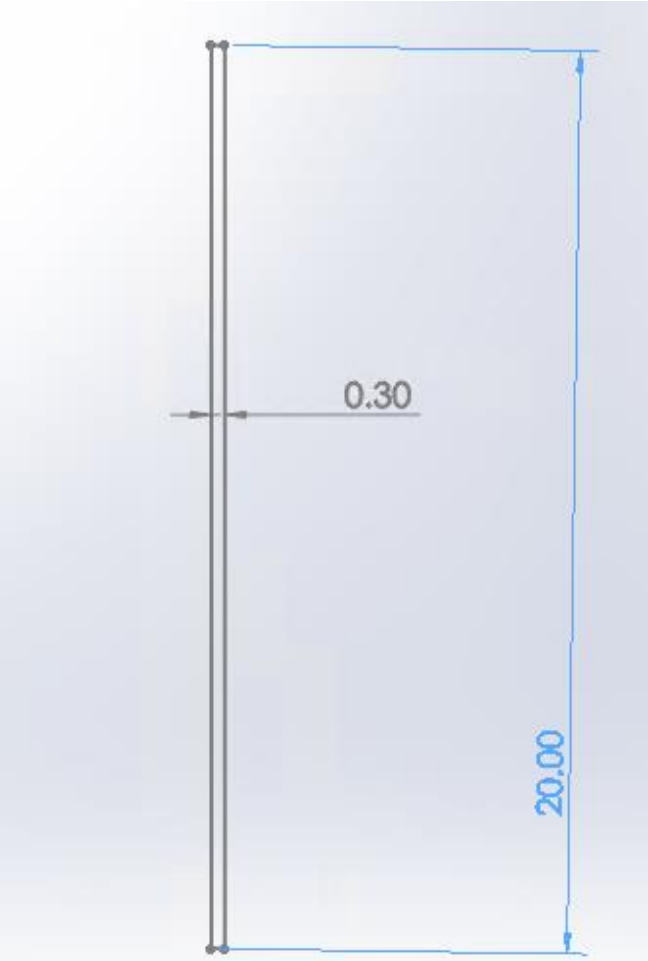

Figure 41: Single CAD drawing with dimensions

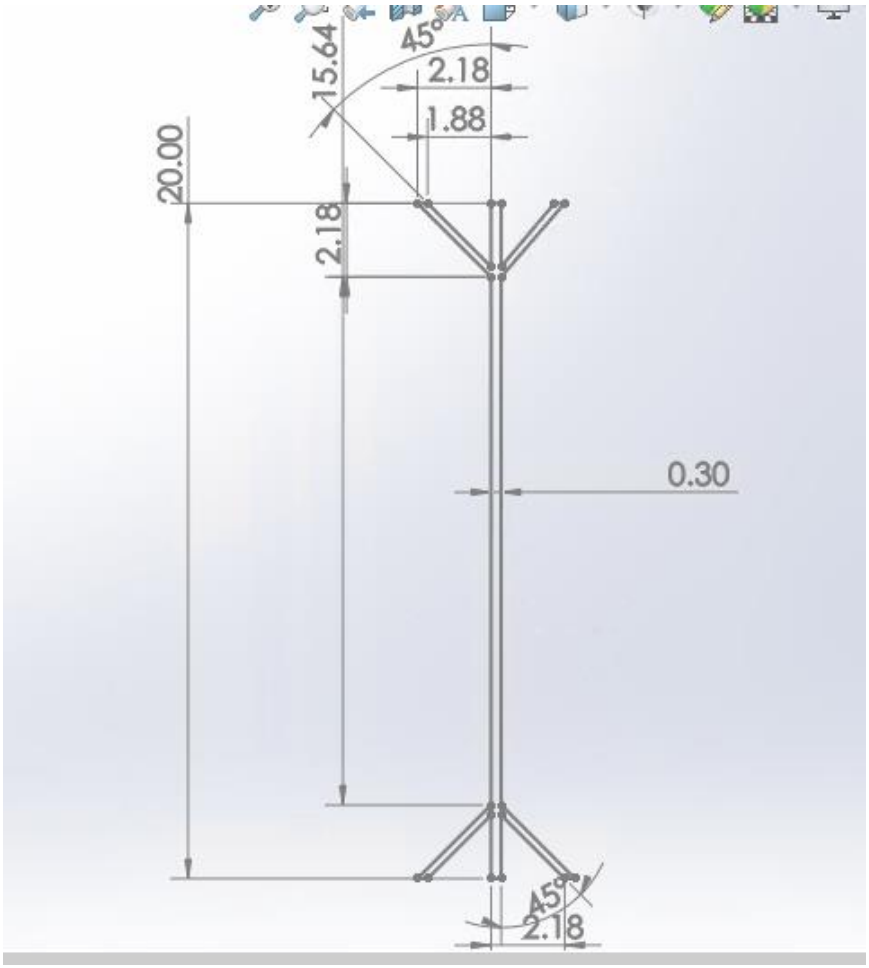

Figure 42: Y-Channel CAD drawing with dimensions

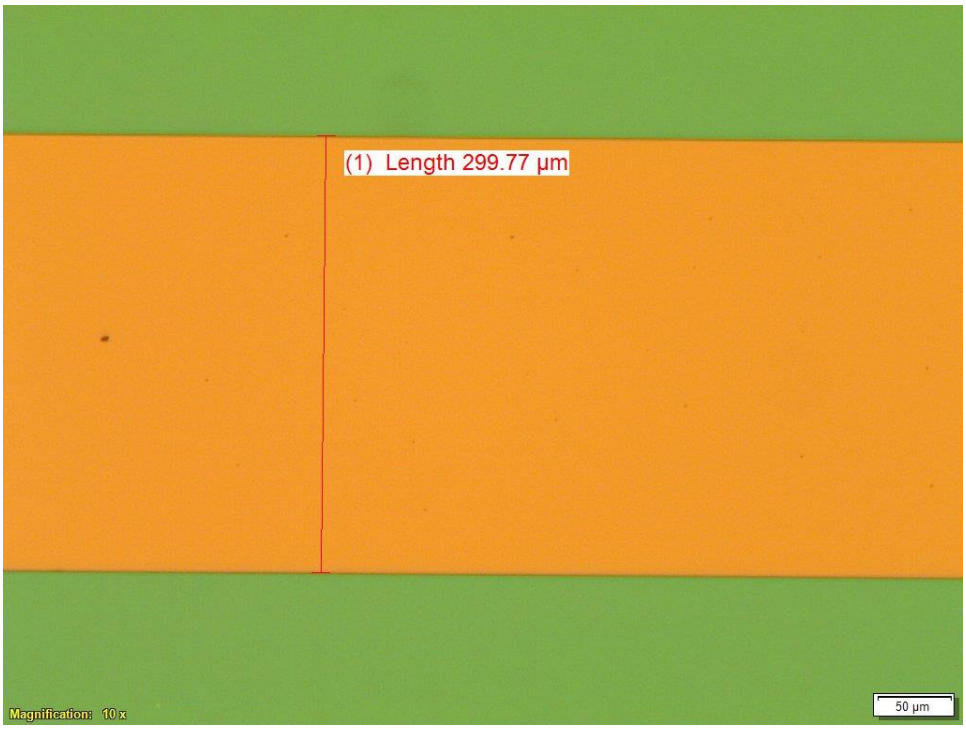

Figure 43: Cleanroom Microfluidic Device Olympus OLS 4000 LEXT Microscope

APPENDIX B: Colbalt Ferrite Nanoparticles

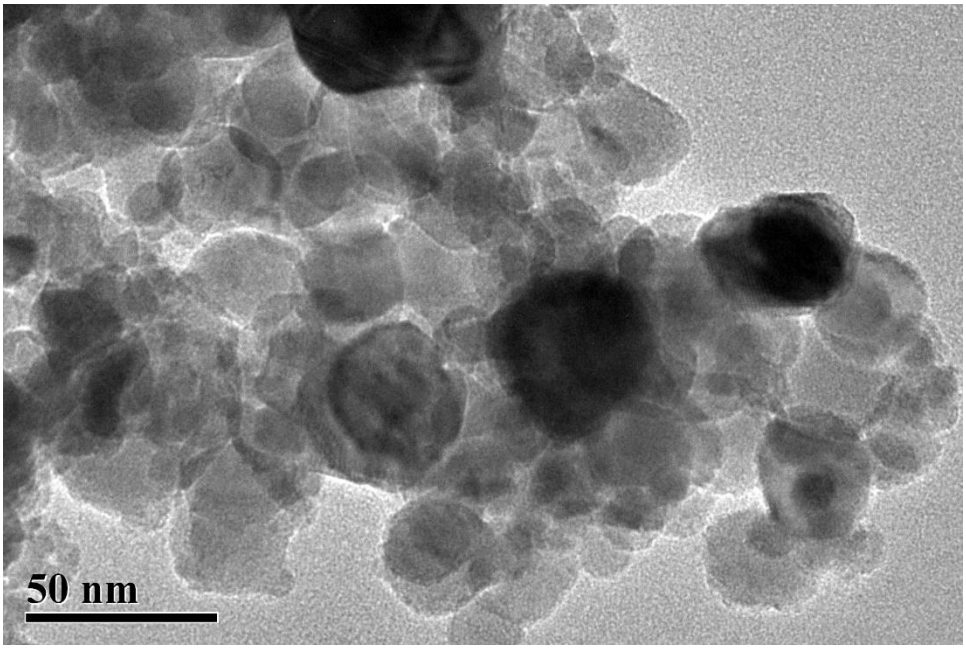

Figure 44: Cobalt Ferrite Nanoparticles Group 1 TEM

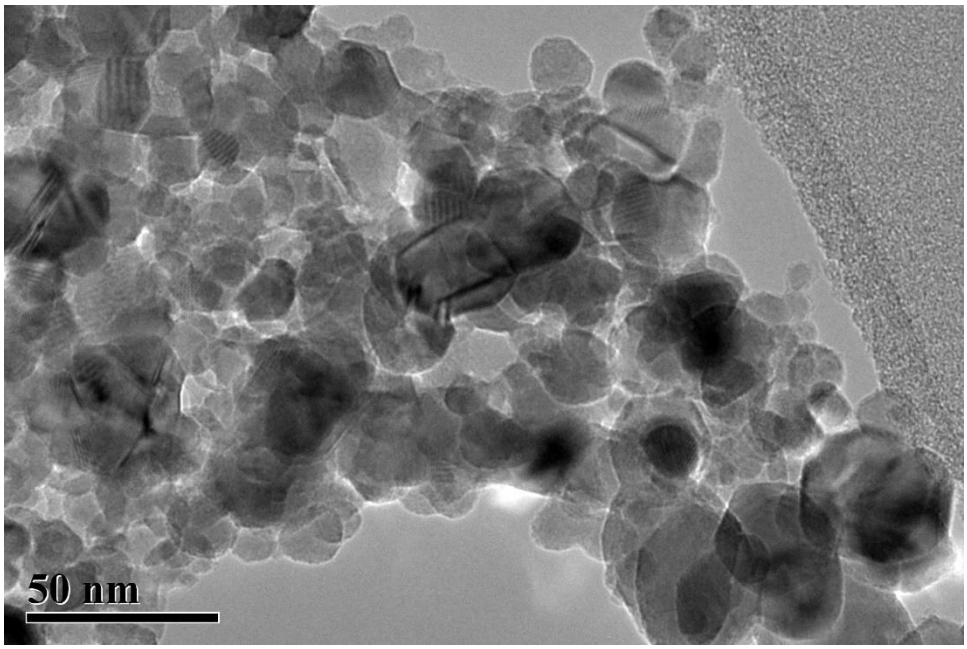

Figure 45: Cobalt Ferrite Nanoparticles Group 2 TEM 50nm

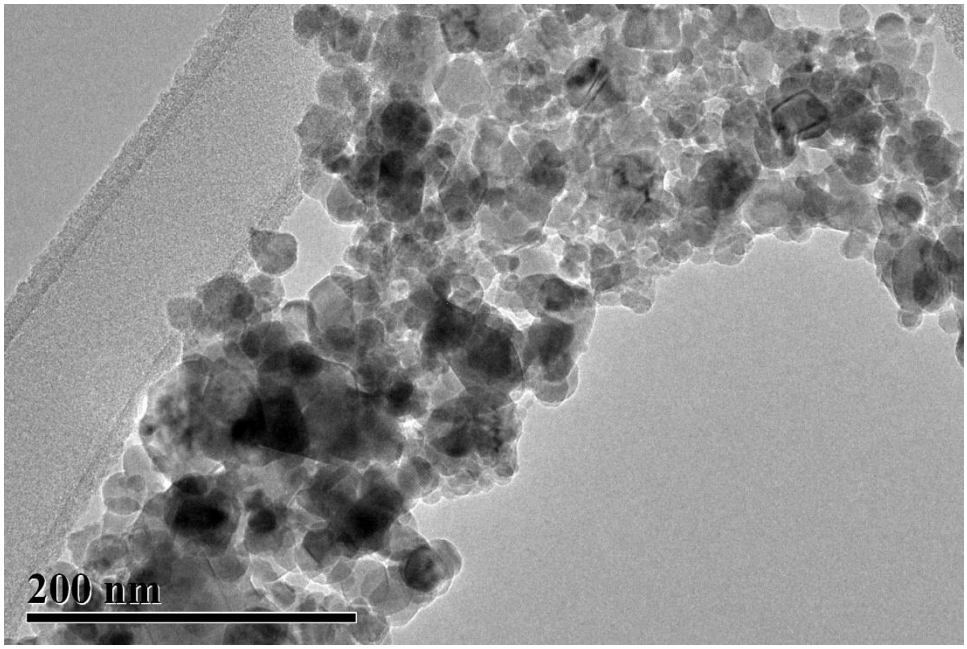

Figure 46: Cobalt Ferrite Nanoparticles Group 2 TEM 200 nm

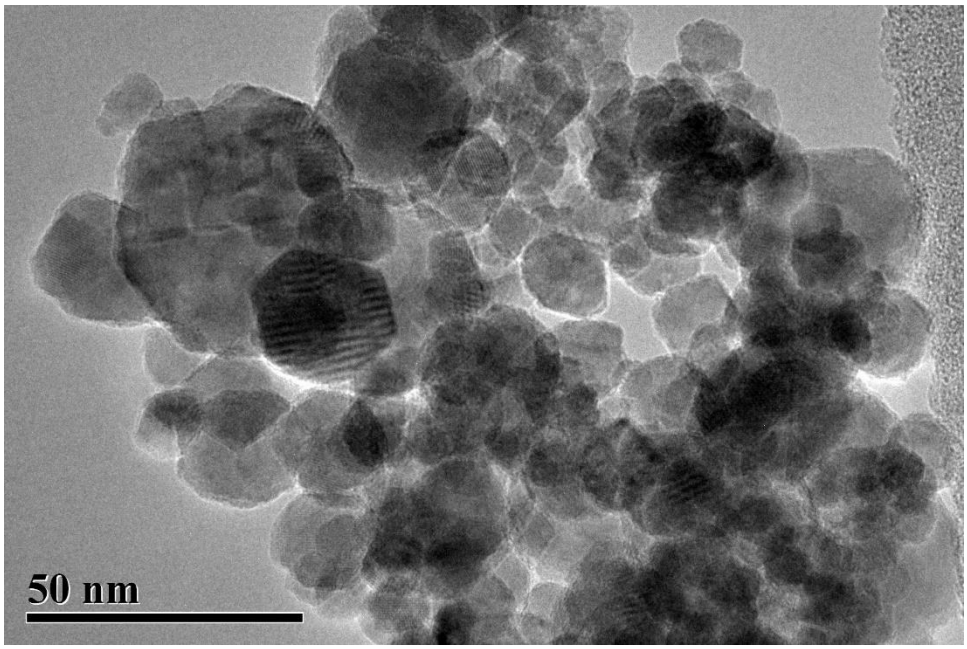

Figure 47: Cobalt Ferrite Nanoparticles Group 3 TEM 50 nm

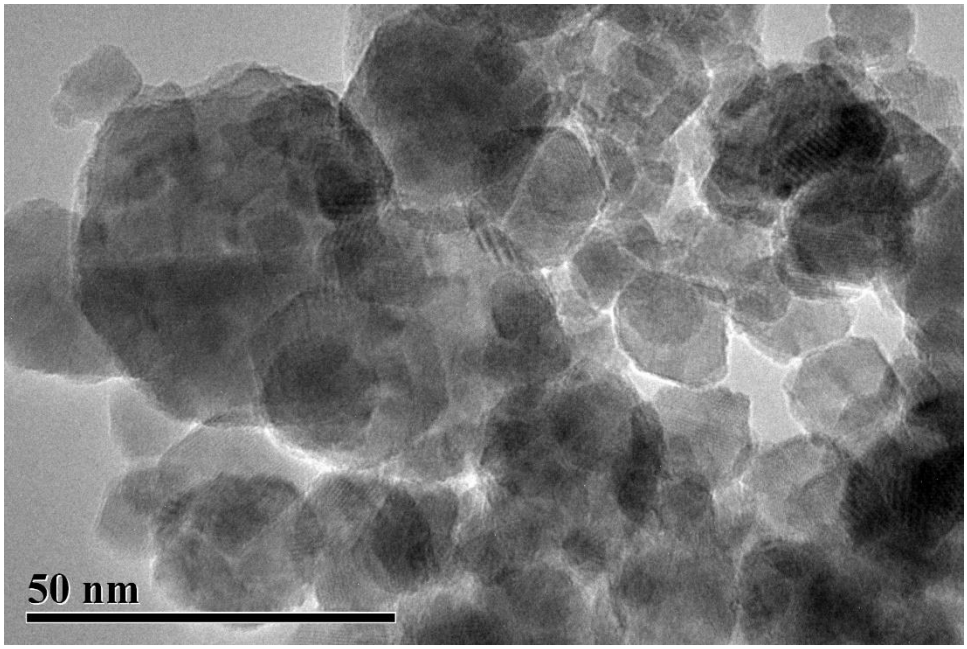

Figure 48: Cobalt Ferrite Nanoparticles Group 3 TEM 50 nm

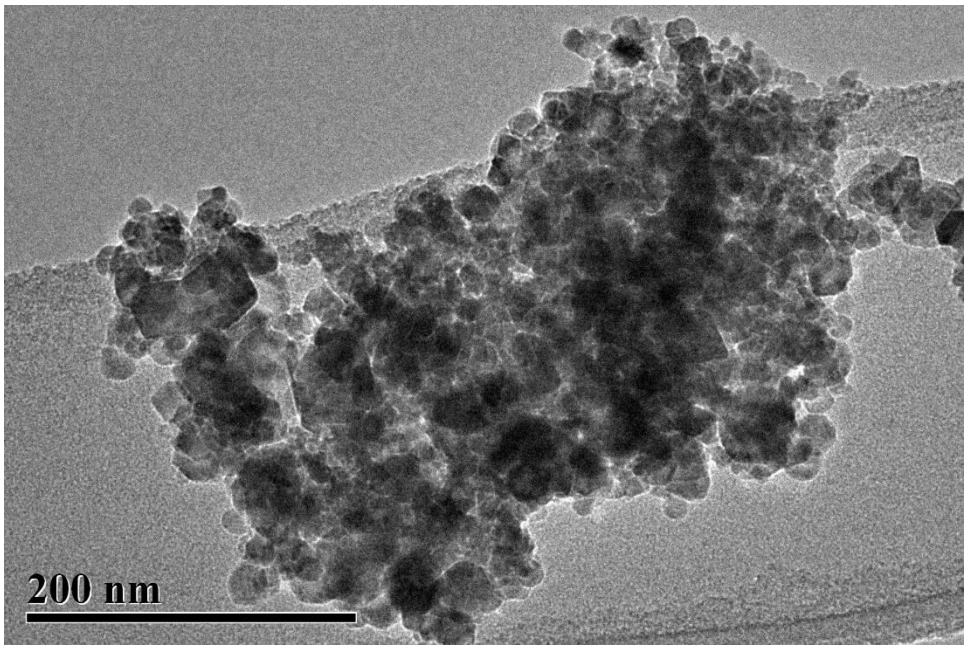

Figure 49: Cobalt Ferrite Nanoparticles Group 4 TEM 200 nm

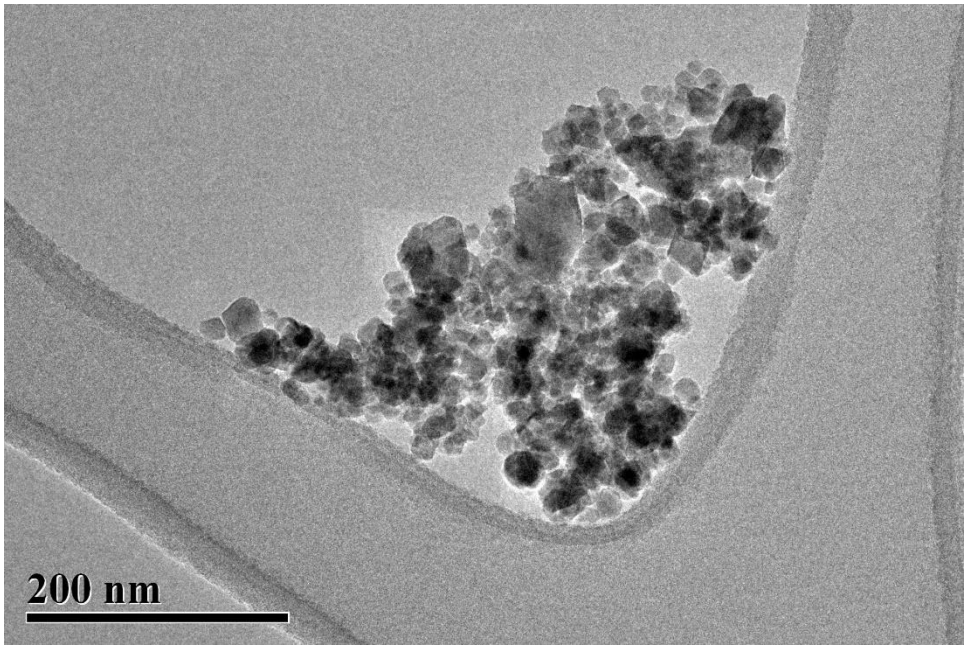

Figure 50: Cobalt Ferrite Nanoparticles Group 5 TEM 50 nm

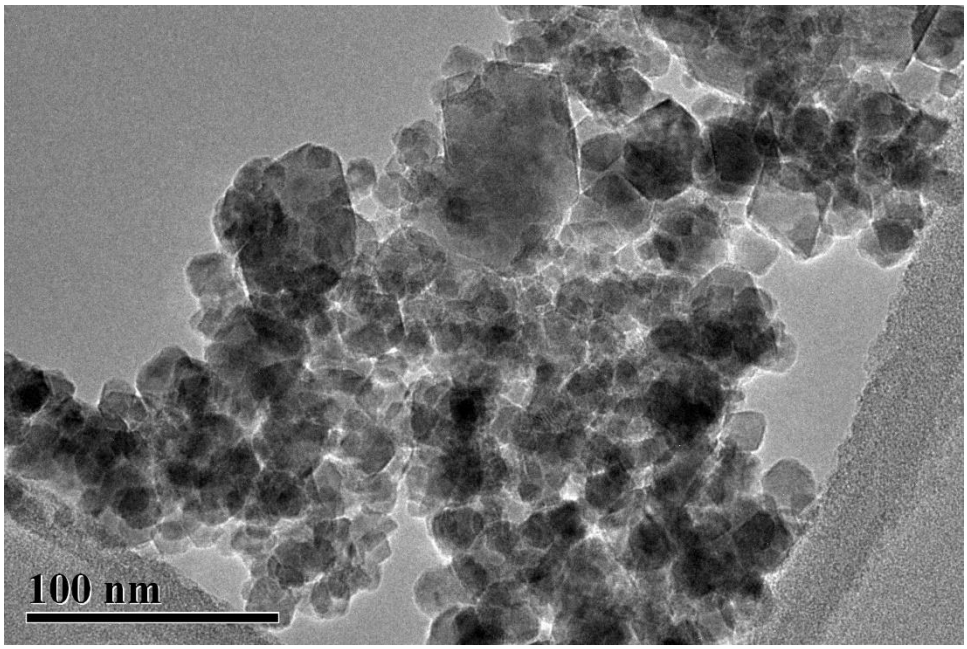

Figure 51: Cobalt Ferrite Nanoparticles Group 5 TEM 100 nm

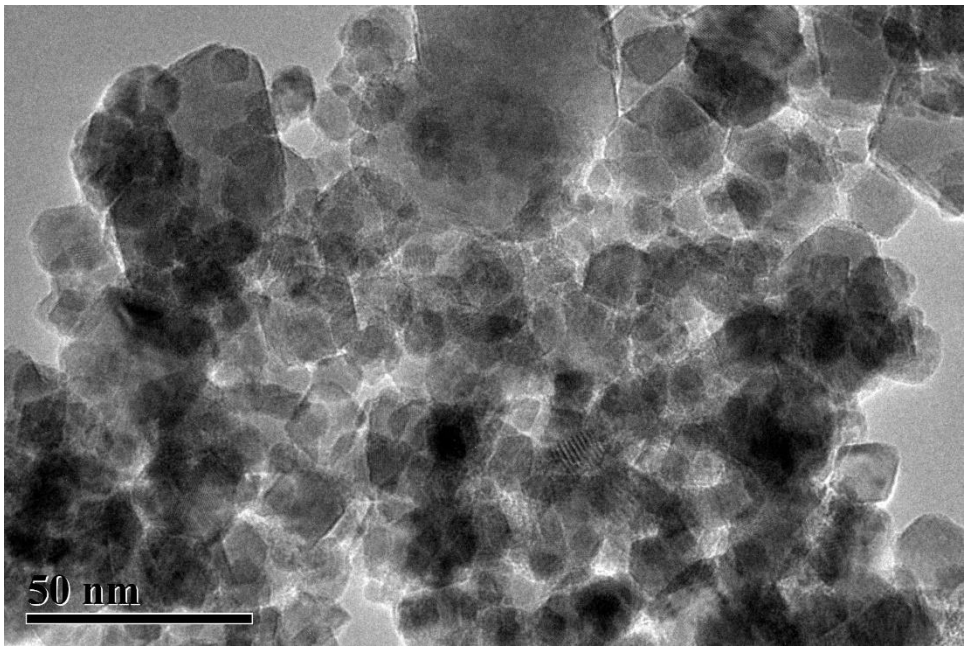

Figure 52: Cobalt Ferrite Nanoparticles Group 5 TEM 50 nm

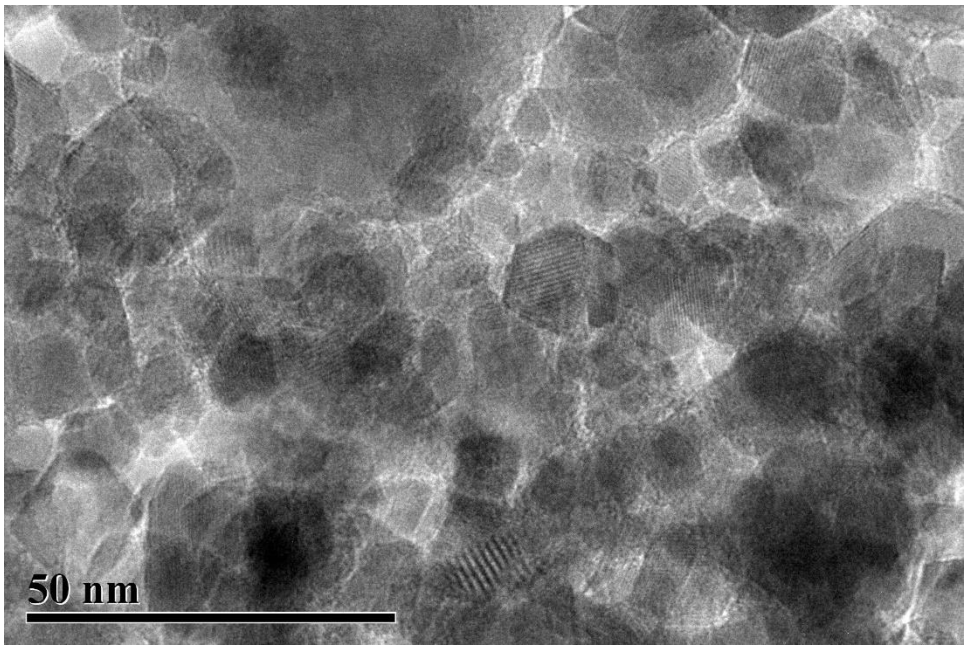

Figure 53: Cobalt Ferrite Nanoparticles Group 5 TEM 50 nm

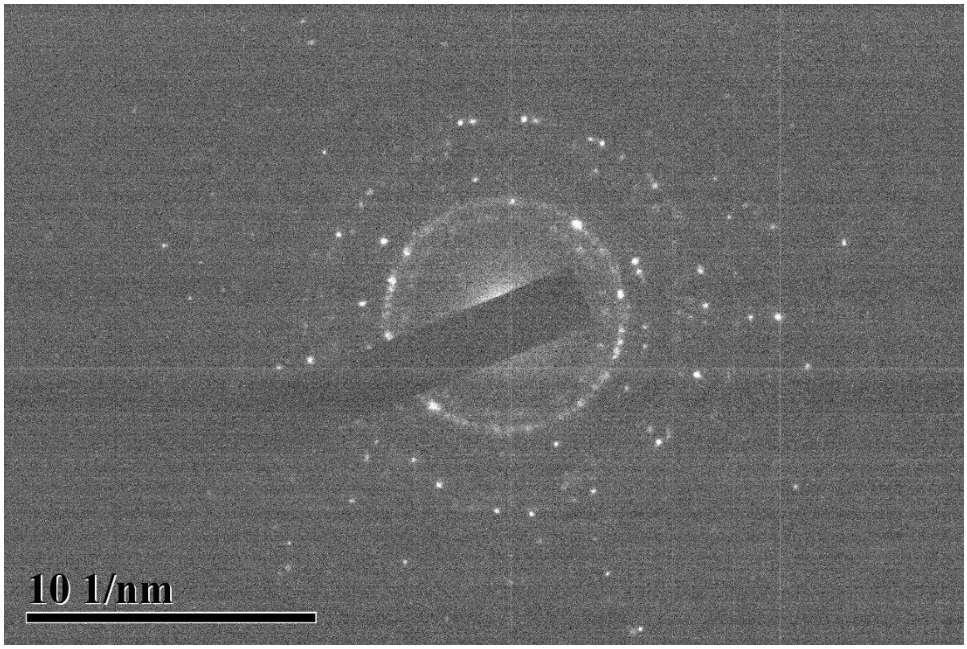

Figure 54: Cobalt Ferrite Nanoparticles Group 5 TEM Diffraction Pattern

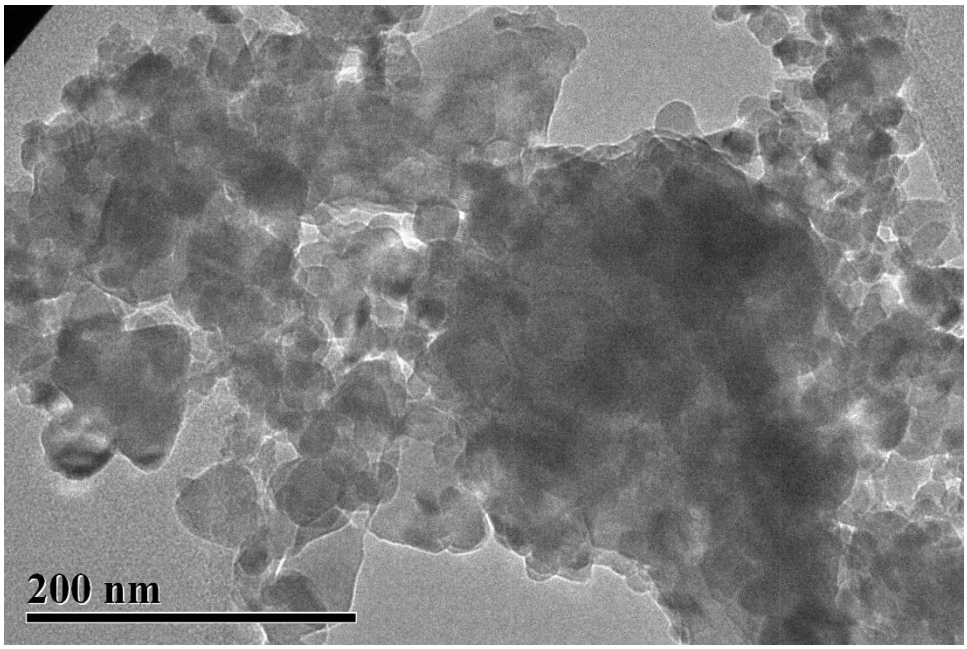

Figure 55: Cobalt Ferrite Nanoparticles Group 6 TEM 200 nm

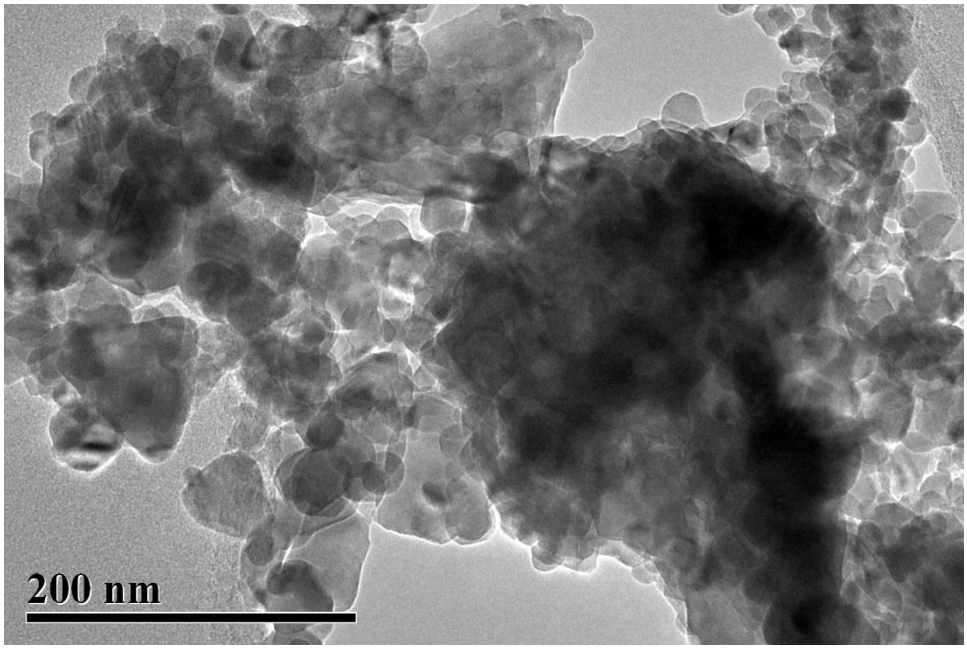

Figure 56: Cobalt Ferrite Nanoparticles Group 6 TEM 200 nm

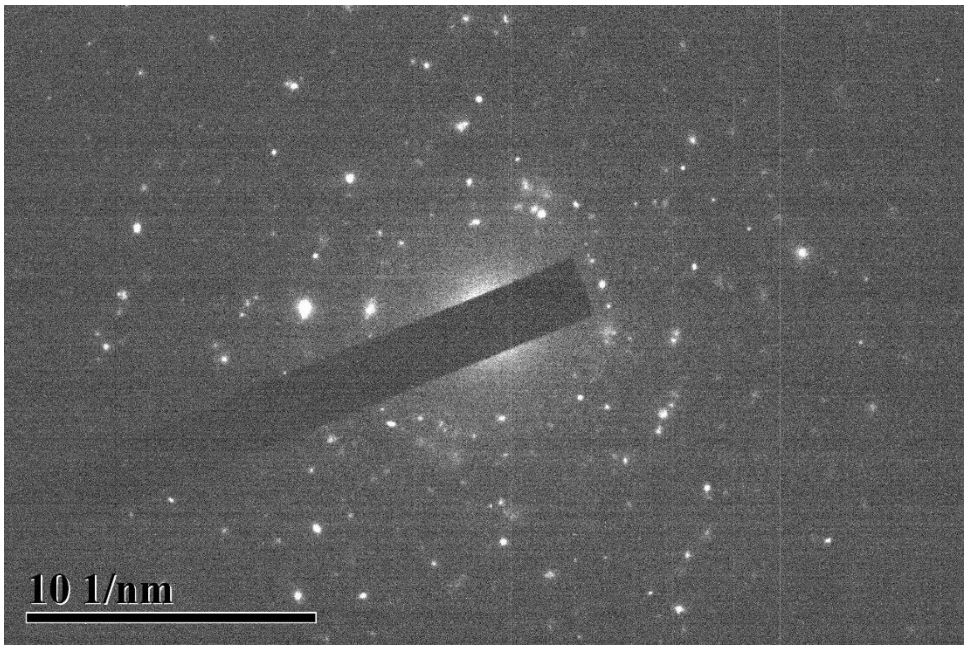

Figure 57: Cobalt Ferrite Nanoparticles Group 6 TEM Diffraction Pattern